Politecnico di Milano

Perovskite based Inks for Optoelectronic Devices

Ph.D. Dissertation, Physics Department

XXXI Cycle

Supervisor: Dr. Annamaria Petrozza

Tutor: Prof. Guglielmo Lanzani

Coordinator: Prof. Marco Finazzi

Author: Roberto Sorrentino

ID number: 858703

Academic Year 2018/2019

Contents

Chapter 1

Introduction

The increased demand of energy and the rapid evolution of optoelectronic devices is a direct consequence to the increased number of people in the world and the improved quality of life. For this reason, in this field, new materials are constantly studied.

In the Ph.D. thesis, three different projects are explained. All these projects turn around a material with hundreds of years but back to an exponential interest for scientist and researchers. The well-established Titanate-based Perovskite leave the floor to Hybrid Organic-Inorganic Perovskite materials. These materials have the very same crystalline structure but they are made of different cations and anions. The differences in the chemical composition are reflected on the different properties of the material, obtaining semiconductor materials that might be useful in everyday life. Hybrid Organic-Inorganic Perovskite materials are now mainly studied for optoelectronic applications such as solar cells, photodetectors, light emitting diodes and transistors.

Starting from 2012, the Power Conversion Efficiency (PCE) reached and recently overcame the Silicon based solar cell values, that is the technology commonly used on our roof nowadays for light harvesting applications. In the market of photovoltaic different competitive strategies can be adopted by using Hybrid Organic-Inorganic Perovskite materials, such as Perovskite solar cells,

Perovskite/Silicon Tandem solar cells and/or Perovskite/Perovskite Tandem solar cells.

To get hold of a portion of the market in photovoltaic applications, Perovskite based solar cells, present some issues that have to be solved yet. Some of them are related to the material itself; what is still needed is a deeper study on the stability of the material, how to protect the material from environment and how to passivate the defects in the crystalline structure.

Some other issues are related more on technological problems: since it is a recent technology, what is still missing is the so called "scale-up" process; in other words, going from a laboratory-scale product to an industrial-scale one. In fact, the great values reached in literature up to now, are obtained with deposition techniques that are hardly up-scalable. This route intersects different key changes in the production and optimization of wider active area devices. Another aspect to take into account for an hypothetical scale-up is the cost and the toxicity of the raw materials used to synthetize Hybrid Organic-Inorganic Perovskite materials. Avoiding toxic solvents permits to decrease the price for handling the materials during the production and to have more competitive technologies on the market.

The other investigated field, the Perovskite-based light detector devices, is one of the possible applications that can be achieved in a short to medium time-frame. Also in this field, the key point is to have a deep knowledge about the fundamental properties and the stability of the material in ambient and under working conditions and to obtain a large-area-compatible deposition technique with performances of the devices competitive with the nowadays-used technologies.

Thanks to the great properties, the cheapness and the solution processability is worth to spend time and money for studying these innovative materials. Researchers, scientists and engineers are nowadays working to fix the last key aspects and, once these issues on material and up-scalabilty will be achieved, Hybrid Organic-Inorganic Perovskite could jump into the optoelectronic market.

In this section, perovskite material is introduced. This is the material that I've been working with during my Ph.D. period. Here a deep discussion about the crystalline structure and the amazing properties but also the disadvantages and the open questions on this material.

1.1 PEROVSKITE

1.1.1 CRYSTALLINE STRUCTURE

The name *Pervoskite* comes from a particular crystalline structure that was discovered in a mineral found in 1839 in the Ural mountains, in Russia, by Gustav Rose and named few years later by Perovski, a Russian mineralogist.

Each material that presents the same crystal structure to calcium titanium oxide ($CaTiO_3$) is classified as perovskite material. It presents a general chemical formula ABX_3, where A and B are two cations and X is the anion that bonds the both cations and it is usually an oxygen atom or an halogen atom.

The structure that characterizes the perovskite material is a cubic structure. In the middle of the cage there is a cation A, on the vertices of the cube there are eight cations B, that are in the middle of eight octahedra formed by anions X^n (n can be -2 for Oxygen or -1 for Halogens). The ideal structure for Perovskite is showed in Figure 1.1.1.1

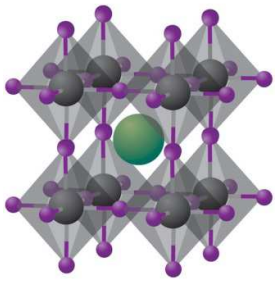

Figure 1.1.1.1 : Crystalline structure for an ideal perovskite material. The green round is the cation A, gray rounds are cations B forming the cubic cage and purple rounds are anions X forming the octhaedra. [1]

The A position is occupied by cations that can be both organic or inorganic molecules. The most famous organic cations to constitute a perovskite structure are Methylammonium ions – $CH_3NH_3^+$ (abbreviated to MA^+), Formamidinium – $[CH(NH_2)_2]^+$ (abbreviated to FA^+) and the mix between these two. Regarding the inorganic cations, is worth to mention Cesium – Cs^+, Rubidium (Rb^+), Potassium – K^+, Sodium – Na^+ and Strontium – Sr^+. [2]

The B position is occupied by metal cations. The most common are Titanium – Ti^{4+}, Lead – Pb^{2+} and Tin – Sn^{2+} but recently it's growing the interest for Lead-free perovskite; for these materials are used other elements such as Germanium – Ge^{2+}, Copper – Cu^{+1}, Silver – Ag^{+1}, Gold – Au^{+1}, Bismuth – Bi^{+3} or a permitted mix of these cations. [3,4,5,6]

Finally, the X position is occupied by anions. They can be oxygen (O^{2-}) or halides. The halides are the medium-size ones such as Chloride (Cl^-), Bromide (Br^-) and Iodide (I^-). It's worth to mention that also a mix of the halides can be possible and it will be discussed later.

Having the right size for ions, both cations and anions, is fundamental in the perovskite structure. By changing the size of cations and anions, the bonds can be stretched or compressed. This causes a distortion of the ideal crystalline structure and can bring to a change in the coordination of A and/or B cations (Figure 1.1.1.2). The extreme case is that the perovskite changes the configuration and the crystals became confined in one, two or three directions.

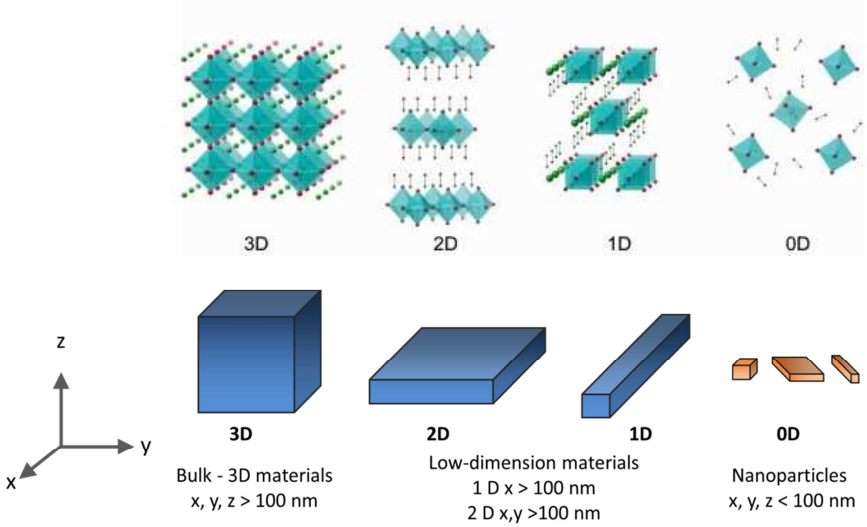

Figure 1.1.1.2: Change in the crystalline structure and reduction of the symmetry in perovskite crystals. Each structure is correlated with a geometric solid to underline the 3D, 2D, 1D or 0D confinement.

Two important parameters are needed to indicate and predict the crystalline structure for different kind of materials. The first one is called the *Tolerance Factor* (*t*) and was introduced by Victor Moritz Goldschmidt in 1926. It's an indicator for the stability and the distortion of the crystal structures. The second parameter is called the *Octahedral Factor* (μ). In an idealized solid-sphere model, *t* is defined as following:

$$t = \frac{R_A + R_B}{\sqrt{2}(R_B + R_X)} \ .$$

where R_A, R_B and R_X are the ionic radii of the A cation, B cation and X anion, respectively. The *t* range value is between 0.81 and 1.1. Lower values lead to tetragonal or orthorhombic symmetry. These symmetries can be broken with temperature for almost any type of perovskite materials.

The band gap of halide perovskite materials can be tuned by changing the combination of all the three components:

- The cation A doesn't play a major role in determining the band structure but its size can influence the optical properties by deforming the octahedra. As we increase the size of the cation A, we expect the crystal structure to expand and the band gap to decrease, obtaining a shift towards the red in the

absorption onset. [7] This explains the reason why $CsPbI_3$ absorbs up to shorter wavelength than $MAPbI_3$ and $FAPbI_3$ that absorb up to longer wavelength, following the length of the ionic radii $R_{Cs}^{+} < R_{MA}^{+} < R_{FA}^{+}$.

Generally, perovskites with a mono-A-cation suffers of thermal and structural instability. To improve these properties and to optimize the band gap for optoelectronic devices, mixture of MA^+, FA^+ and Cs^+ are used. For example, a mixture of MA^+ and FA^+ is used to improve the solar light harvesting with an active material called $MA_xFA_{1-x}PbI_3$. With particular ratio of organic cation is possible to not form the undesired δ-phase for $FAPbI_3$ and to obtain higher values for power conversion efficiency in the device.[8] After this work, other mixed cations A were found to be more effective such as the mix between FA^+ and Cs^+ in $Cs_xFA_{1-x}PbI_{3-y}Br_y$ improving the thermal stability of the material and optimizing the band gap.[9] After the two-A-cation, was developed the three-A-cation with $Cs^{+,}$ FA^+ and MA^+ in $Cs_x(MA_{0.17}FA_{0.83})_{1-x}Pb(I_{0.83}Br_{0.17})_3$; by using this perovskite material, the power conversion efficiency reached for the first time the incredible value of 21.1%. [10]

Finally, another cation is added to the previous three. By introducing the Rb^+, the efficiency and stability further increased and the performances were stable for almost 500 hours in continuous working conditions [11].

- The Metal cation B can be Pb, Sn, Ge for optoelectronic applications. The electronegativity of the metal cation decreases as we move down in the same group in the periodic table and the decreasing in the covalent character of the B-I bond, causes the following trend in the band gap $AGeI_3 < ASnI_3 < APbI_3$. Replacing Pb with Sn is a valid alternative to obtain lead-free materials but the oxidation state of tin, tends to go from Sn^{2+} to Sn^{4+}. The change in oxidation state, brings to change the charge neutrality of the material and the consequence is the separation of the phases of the components that constitute the perovskite. Materials where the Sn partially substitutes the Pb, didn't show enhanced stability neither. [12]
- The halide X, permits the shift of the band edge in the absorption spectra, towards longer wavelength when we move down in the group of the halogens (Cl, Br, I). The blue shift in the band gap, by reducing the size of the halogen, can be explained with the decrease in the covalent character of

the chemical bonding with Pb. Is also possible to mix two different halides (Cl and Br or Br and I), obtaining a continuous tuning of the band gap and the optical absorption.

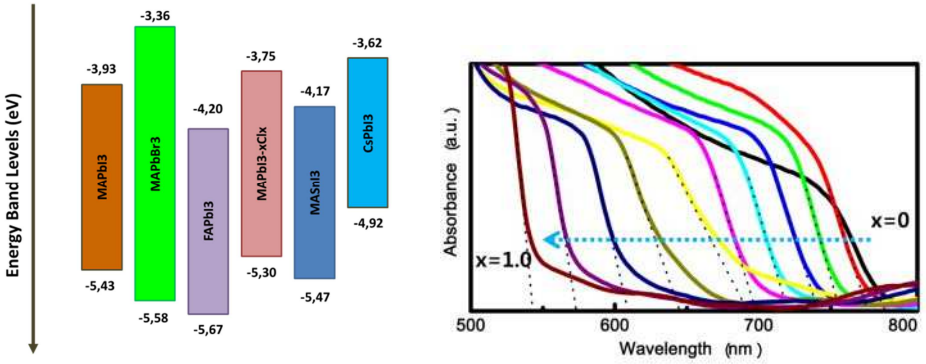

Figure 1.1.1.3: Energy band levels for different perovskite materials and values in eV (left side). Change in the absorption band edge by changing the content of halides ratio in the $MAPb(I_{1-x}Br_x)_3$ perovskite crystalline structure (right side). [13]

Theoretical calculations predict a direct band gap for perovskite materials. These are the most interesting materials for photovoltaic applications; [14] the presence of a direct band gap explains the strong optical absorption as high as the absorption of inorganic III-V semiconductor materials.

1.1.2 PHOTO-GENERATED CARRIER BEHAVIOUR

Semiconductor materials are able to generate excitons or separated charge carriers upon exposure of an external light source. An exciton is defined as a quasi-particle composed of bounded electron and hole through Coulomb's interaction, resulting in a total neutral charge. The strength of the bounding it's an important parameter that needs to be measured and is called *exciton binding energy* (E_B).

The types of excitons are *Wannier-Mott* excitons ($E_B \leq 0.1$ eV) that are usually found in semiconductor crystals with high dielectric constant and small energy gaps and *Frenkel* excitons ($E_B \geq 0.1$ eV) that are usually found in materials with relatively small dielectric constant. The numeric value E_B, discriminates if the charge carriers exist as free carriers or as bound electron-hole pairs upon photo-excitation.

For example, in $CH_3NH_3PbI_3$, E_B is estimated between a range of 19 to 50 meV. [15] This means that E_B is comparable to room-temperature thermal energy (k_BT ~

25 meV) but for $CH_3NH_3PbBr_3$ and $CH_3NH_3PbI_{3-x}Cl_x$ the measured E_B values are higher and correspond to 76 meV and 98 meV, respectively. [16] Higher values mean that the charges composing the excitons are more tightly bounded.

It is now accepted that in perovskite materials, the free charges are spontaneously generated; this is another reason why perovskite materials are excellent for light-harvesting applications. [17]

While a solar cell device needs a small E_B to easily dissociate the exciton, a Light Emitting Diode (LED) device, needs an high E_B to permit the radiative recombination decay.

Once the carriers are photo-generated they have to travel through the semiconductor. The diffusion length is characteristic for each material. $CH_3NH_3PbI_3$ supports the ambi-polar charge transport. This means that both electrons and holes can diffuse through the perovskite crystal structure. In particular, for a film obtained by spin coating starting from solution, it shows the hole diffusion length value equal to 105 nm and the electron diffusion length value equal to 129 nm. These length values are extremely high, much higher than the typical values observed in:

- other solution processed materials, where the length for the carriers is approximately of 10 nm.
- organic molecules deposited by thermal evaporation (10-50 nm).
- colloidal quantum dots (30-80 nm).

Mixed halide $CH_3NH_3PbI_{3-x}Cl_x$ perovskite material, presents even higher diffusion length values: for both electrons and holes, the length value exceed 1 μm. More precisely 1069 nm for electrons and 1213 for holes. [18]

Both E_B and transport of the charges can extremely vary depending on chemical composition, crystals size and the film morphology. [19] In fact, the photo-physical properties of perovskite materials such as the charge generation, the recombination, the transport and the collection have to be correlated to the morphology of the film formed after the deposition of the material.

In the last years plenty of depositions have been studied by scientists and researchers. What hasn't be found yet, is a protocol from synthesis to deposition, that ensure always the exactly same material's formation and performances. A small change in the ratio of reagents, deposition technique, even in the atmosphere

conditions can bring to a different crystallization in situ; this means different type and concentration of defects that is directly correlated to different performances of the devices.

1.1.3 PHYSICS OF DEFECTS

Crystalline solids present a periodic structure. This means that the position of atoms occur on fixed distances, determined by the unit cell parameters, characteristic for each material. An ideal material has all the atoms in the right position. In reality, all the materials have defects. The defects in a crystalline semiconductor can be categorized as the interruptions of the periodicity of the crystal structure (crystallographic defects) or foreign atoms in the lattice (impurities).
The defects can be divided as *point* defects, *line* defects, *planar* defects and *bulk* defects:

- point defects if the defect affects only one single lattice point. This means that the defect does not extend in any dimension (0D). Some point defects are *vacancies* (a site which would be occupied in an ideal crystal but is vacant), *interstitial* (atoms that occupy a site that should be without atoms), *antisite* (when in an ordered alloy, two different atoms exchange position).
- line defects if the defect affects a single row of the lattice points. This means that the defect is extended in one dimension (1D). The most famous line defect is called *dislocation*. If the dislocation is caused by the termination of a plane of atoms in the middle of the crystal, the dislocation is called *edge* dislocation and this causes to the other adjacent planes a bent. If the dislocation include a structure with an helical path, the dislocation is called *screw*.
- planar defects if the defect is extended in two dimensions (2D). The most important is called *grain boundaries*. This happen when the crystallographic direction of the lattice changes, for example when two crystals grow separately and then meet. Other 2D defects are *antiphase boundaries*, when the crystallographic direction is the same but each side has an opposite phase, *stacking faults*, when are present local deviations of the stacked

layers in the crystal and *twin boundaries*, when a defect introduces a plane of mirror symmetry in the order of the crystal.

- bulk defect if the defect is extended in three dimensions (3D) such as *pores*, *cracks* or *inclusions*. Moreover the impurities can *cluster* together to form small regions of a different phase with respect to the crystal.

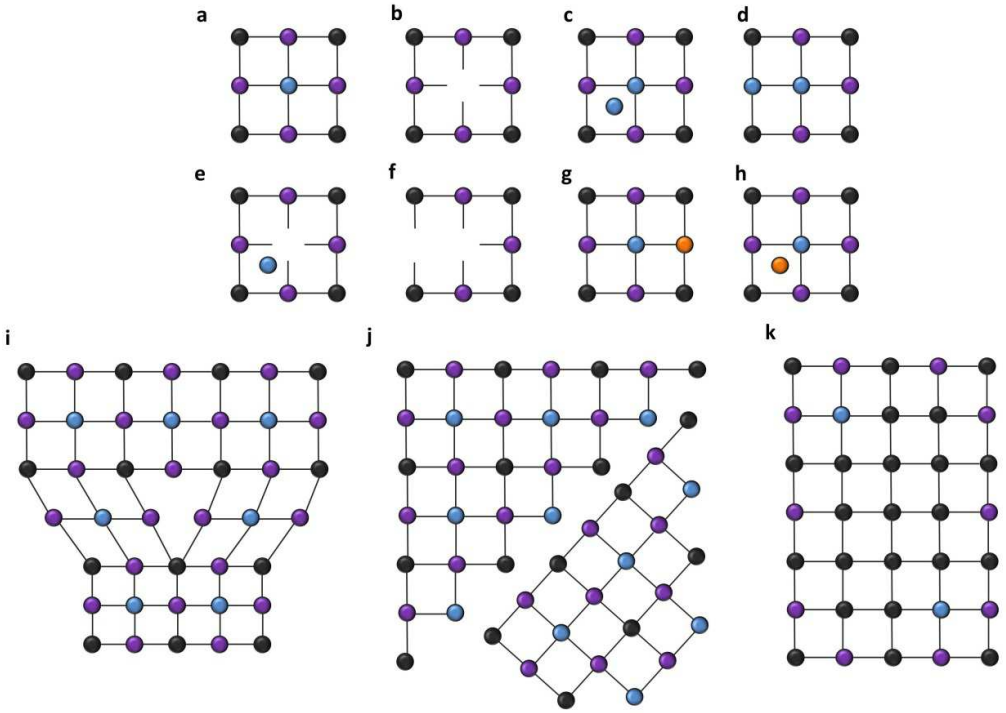

Figure 1.1.3.1: possible defects in perovskite materials: blue dots are A-cations, black are B-cations and purple are X-anions. Sketch of (a) perfect lattice, (b) vacancy, (c) interstitial, (d) antisite substitution, (e) Frenkel defect (interstitial and vacancy), (f) Schottky defect (anion and cation vacancies occurring together), (g) substitutional impurity, (h) interstitial impurity, (i) dislocation, (j) grain boundary, (k) precipitate. [20]

The defects are thermodynamically promoted in semiconductor materials because the entropy tends to be maximized ($\Delta S > 0$) and the formation energy is usually $\Delta H < 0$. The formation energy depends strictly by the atomic chemical potential and the electronic chemical potential, related to Fermi level.

In a solar cell the presence of defects in the active layer can affect the performances of the device. It might affect the charge transport or the recombination sites. For example in $MAPbI_3$ perovskite theoretical calculations (Density Functional

Materials – DFT) have showed that the point defects contribute to *deep levels* in the band gap. They usually have high formation energies and shouldn't contribute to non-radiative recombination centers. Contrarily, the *shallow* point defects could cause doping in the material because the energetic levels are close to the maximum of the valence band or the minimum of the conduction band. These defects usually have low formation energies and their formation is common during the crystallization on the substrate of the perovskite material. Minimizing the concentration of defects is fundamental and, for this reason, lot of scientists and researchers have worked on optimizing various deposition techniques that are explained in the next section.

1.1.4 LOW COST AND PROCESSABILITY

The excellent photovoltaic (PV) performances for hybrid organic-inorganic metal halide perovskite matches with the easy processability and the low-cost of these materials.

By looking at the "Golden Triangle" for photovoltaic application (efficiency, cost and stability), perovskite materials are already satisfying two on three points. The efficiency increased rapidly in few years and is going to reach the highest values possible. The basic costs for the materials are extremely low. For example one of the possible reagents, lead chloride ($PbCl_2$) powder, costs at research level around 100 €/Kg, which is enough to cover 1000 m^2 with a thickness of the film of around 200 nm. [21]

Several different film deposition techniques have been reported till now, underlining the cheapness of materials and the solution processability. Few deposition techniques are explained with the corresponding references in the state of the art for further details. All these deposition techniques are well established and permit to obtain high power conversion efficiency for solar cell devices:

- *one step precursor solution* is one of the most common thin film deposition method for organic-inorganic lead compounds thanks to the simplicity. The precursor solution contains the powder of lead-halide

(PbX_2) and the powder of A-cation-halide (AX). Usually the reagents have a non-stoichiometric ratio (3:1) and are dissolved in high boiling point, aprotic, polar, organic solvents such as dimethylformamide (DMF), dimethylsulfoxide (DMSO), N-methyl-2-pyrrolidone (NMP) or γ-Hydroxybutyric acid (GBL). The solution is kept stirring until complete dissolution of the powders in the solvent and it is spin-casted on the substrate. In-situ crystallization and formation of perovskite happens after removal of the solvent thanks to the rotation of the sample and an annealing till a complete conversion from reagents to perovskite.

The spin rate, the wettability of the substrate and the viscosity mainly due to the concentration of reagents in the solution are parameters that will affect the thickness and the quality of the thin film deposited. [22]

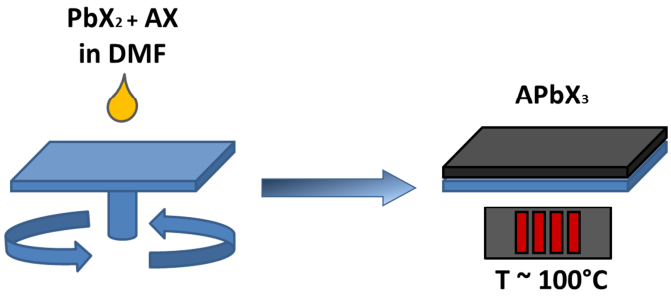

Figure 1.1.4.1: Sketch for one-step deposition technique. The solution is dropped on the sample and the rotation given by the spin-coater, permits the homogenous spread the solution on the sample. The annealing at 100 °C permits the evaporation of the solvent, the crystallization of the material and the complete reaction between the reagents PbX_2 and AX.

- *two steps sequential deposition* is another deposition technique and it includes two solutions to form the perovskite thin film. The reaction occurs between PbX_2 dissolved in DMF and AX dissolved in propan-2-ol (IPA). The first layer of PbX_2 is spin-casted and annealed in controlled atmosphere. After the first deposition, the layer can be converted in perovskite by dipping the sample in AX solution dissolved in IPA for few seconds or is possible to spin-coat the AX solution dissolved in IPA on top of the first layer. If the dripping method is used, the reaction is driven by

the initial crystal lattice that serves as template for the formation of the perovskite. The PbX_2 presents a layered structure and permits an easy inclusions of A-cations in the structure. Both the routes need an annealing step at the end to permit the full conversion of the reagents. [23]

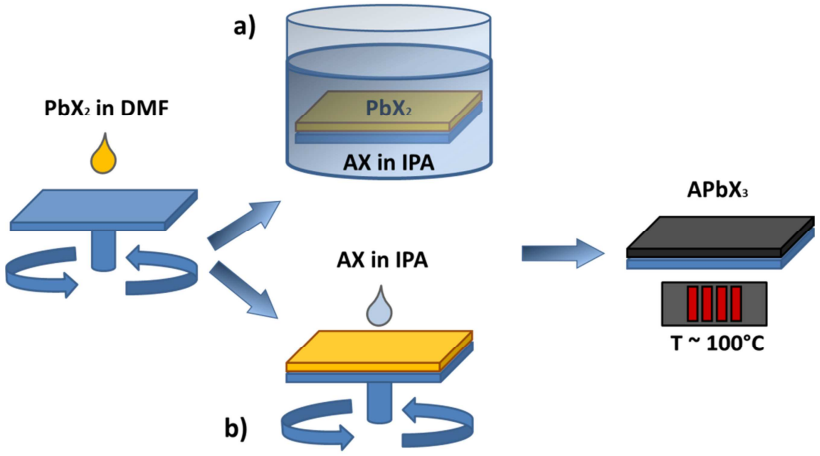

Figure 1.1.4.2: Sketch for two-steps deposition technique. The PbX_2 in DMF solution is dropped on the substrate and the rotation given by the spin-coater, permits the homogenous spread of the solution on the sample. The sample is (a) dripped in AX solution in IPA or (b) spin-coated once again with AX solution in IPA. Both the routes end with an annealing step at 100°C.

- *dual source vapor deposition* is not a technique that involves solvents but is worth to mention it because of the great efficiency values reached with this technique till date. It consists in a deposition technique which simultaneously evaporates solid precursors with a non-stoichiometric molar ratio. A final annealing step is required, in controlled atmosphere, in order to promote the formation of the hybrid organic-inorganic perovskite. The crystallization and the formation of the material is accompanied by a change in color from reddish to dark brown color. The dual source vapor deposition technique permits to have an incredibly high accuracy in thickness values for the active layer; it permits to easily optimize the thickness by maximizing the power conversion efficiency of a solar cell device. Moreover, this technique permits to have pinholes-free layers that are detrimental for the device. [24]

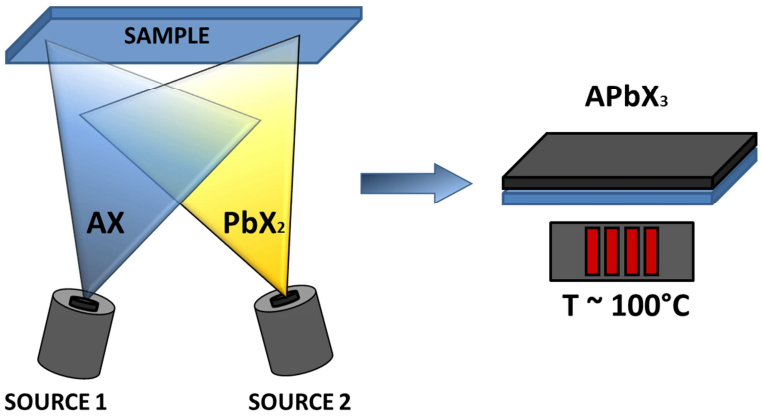

Figure 1.1.4.3: Sketch for dual source vapor deposition. The sources are heated through the passage of current in the filaments. At a certain temperature, depending on the material, starts the evaporation of the powder of AX and PbX_2. The vapors form a cone and are deposited on the sample with the right ratio. The annealing at 100°C permits to complete the reaction between the precursors.

- finally, the last technique here discussed, is called *solvent quenching* or *solvent dripping*. It consists in a spin coating of a solution in which the powders are dissolved in polar organic solvents (DMF, GBL, DMSO…). During the rotation of the substrate, after a certain amount of time, a consistent volume of a solvent in which the perovskite is poorly soluble (Toluene, Chlorobenzene, …) is dripped. The first part is needed to spread the precursors solution on the substrate, while the second part is needed to fastly remove the solvents and to permit a fast crystallization in situ of the perovskite material. An annealing step is required at the end of the process.

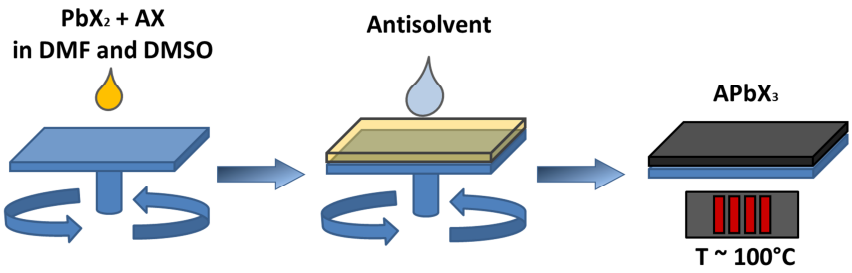

Figure 1.1.4.4: Sketch for solvent quenching deposition technique. The solution of DMF and DMSO in which are dissolved the precursors is dropped on the sample and the rotation given by the spin-coater, permits the homogenous spread of the solution on the substrate. After few seconds, a certain amount of

anti-solvent is dripped on the film, permitting the fast removal of the previous solvents and the fast crystallization of the perovskite. The annealing at 100°C permits to accelerate the crystallization of the material and the complete reaction between the reagents PbX_2 and AX. [25]

1.1.5 THIN FILMS vs. CRYSTALS

Photovoltaic and other optoelectronic applications are the main field in which the metal halide perovskite might be used. As already discussed in section 1.1.1, is possible to easily tune the band gap of the material by simply changing the ratio between two halide anions (for example $CH_3NH_3PbI_{1-x}Br_x$ with $0 \leq x \leq 1$) covering a band gap from 1.6 eV to 2.3 eV. This easy tuning is amazing for multi-junction solar cells and color-tunable LEDs applications.

However, when mixed-halide perovskite are employed in solar cell as active layer, the maximum voltage obtainable is not linear with the change in the optical band edge. [26] Was also proved that white-light illumination induces the formation of a sub-band gap photoluminescence feature always fixed at 1.68 eV, independently from the starting energy gap. This feature disappears after several minutes if the sample is kept in dark conditions.

Even if the band edge is tunable, deeper studies showed a phenomena called *photo-instability*, peculiar for mixed halides perovskite materials. The photo-instability is due to the formation of photo-induced sub-band gap emissive states. The ions in the perovskite structure, are able to move around the film diffusing through defect sites, evolving to a segregation of two different phases: the low band gap, iodide rich area close to illuminated surface of the film and the wide band gap, bromide rich area. Once the sample returns in dark condition, driven by entropy, the two halides phases mix themselves again and return to a homogenous conditions.

The phase segregation and the re-mixing of the halides is not fully understood yet.

What is clear is that these effects are correlated to a series of different parameters such as the history of the sample exposure, the species of the A-site cation, the intensity of the illumination and also the gradient of absorbed light in the material. In [27] Barker et al., considering that the ions segregation takes place via halide defects, they showed that is possible to form iodide-rich low band gap areas close

to the illuminated surface of the film and the segregation is driven by the strong gradient in carrier generation rate through the thickness of the material (Figure 1.1.5.1). They also found a way to properly engineer the active material by controlling the density of halide defects introducing a certain amount of AX compound in excess. This might stabilize the photo-instability of the perovskite, having a material with a tunable band gap even upon exposure to light sources and the solar cell device has a stable open circuit voltage.

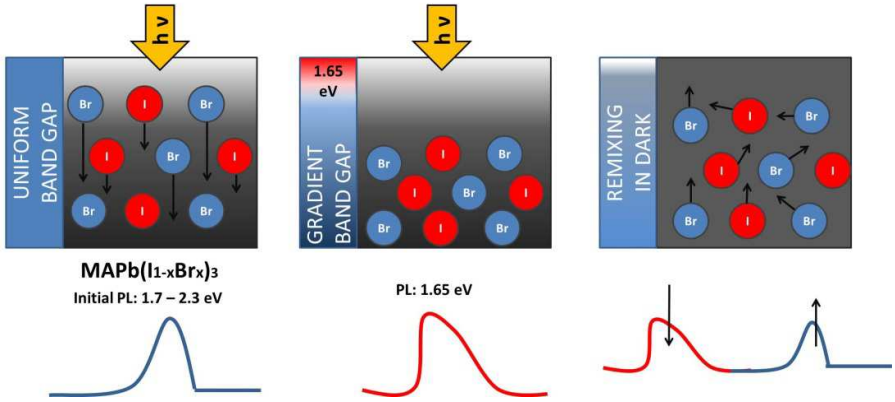

Figure 1.1.5.1: Sketch for photo-instability in $MAPb(I_{1-x}Br_x)_3$. The material has a defined ratio of halides with a proper band gap. After photo-exposition, the halides tend to diffuse through defects (left image) forming a future in the PL at 1.65 eV (image at the center). Once the light is switched off, the halides tend to inter-mixing again driven by entropy (right side image).

A more recent work [28], shows that the alternative route to obtain a photo-stable material is through the passivation of the surfaces. The passivation helps to reduce the non-radiative recombination loss and enhance the efficiency of the solar cell devices. Since perovskite presents under-coordinated lead ions at the surfaces and at the grain boundaries, these defects permit the trapping of the charge carriers and the evolution to non-radiative recombination losses. To coordinate these defects has been observed that the presence of well-engineered ligands, can effectively passivate defects or trap states. These ligands are added via post-treatment, after the deposition of the perovskite material. Few ligand examples are pyridine and thiophene used by Snaith et al in [29]. They have showed that the passivated films had orders-of-magnitude longer photoluminescence lifetime.

Others scientists [30] showed that the amino groups of the ligands bond to Pb-I lattice, reducing the recombination centers. In general, an increasing in

photoluminescence lifetime is also accompanied to an increase in power conversion efficiency of the devices.

The amino-groups based ligands and carboxylate groups are frequently used in nanocrystals, where the most significant defect is the surface. The ligands are usually added in the starting solution before the synthesis and the passivation of the surfaces is due to the bonding between amino-group and the under-coordinated lead present on the surface. In contrast to thin films, generally, the nanocrystals present higher photo-stability. In fact, the ligands on the surface, not only passivate the defects and the non-radiative traps but permit also to isolate the nanocrystals. The consequence is an increasing in photoluminescence quantum yield (PLQY) of the material.

The presence of long ligands is usually good for the emission properties and light emitting diode applications but it's detrimental for solar cell devices because the presence of long alkyl chains interrupt the charge transport between one nanocrystal and the adjacent one making difficult the extraction of the charges from the active layer to the anode and cathode.

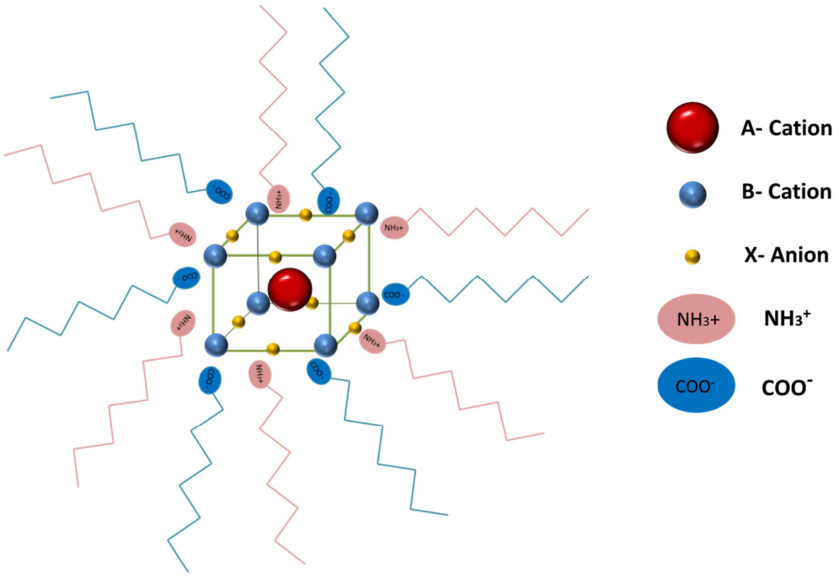

Figure 1.1.5.2: Sketch of perovskite nanocrystal passivated by alkyl chains on the surface (on the left side) and legend of the sketch (on the right side).

1.1.6 OPEN QUESTIONS

After almost 7 years working on the hybrid organic-inorganic perovskite materials, scientists and researchers achieved impressive results in different fields of application and deeply studied the material from the basic-proprieties point of view but few open questions are not solved yet. Only by solving the issues will be possible the entrance of this promising material in the optoelectronic market.

Till date, the main issues and debates around perovskite materials are:

- find a way to obtain high-quality perovskite absorber layer with control on morphology, uniformity, crystallinity, coverage and grain orientation. Only by controlling these characteristic will be possible to transfer the exceptional lab-scale-performances to large-scale-performances. This is due to the fact that till now, the main deposition technique that has been used is the spin coater technique. This is not a directly transferable technique for big area devices and company production. Simply by changing the deposition technique from spin coating to blade coating, the performance drops from 22.7% [31] to 16% [32] because of less control in crystallization of the material and lack of knowledge in properly engineer the solvents used as precursors. For this reason is worth to develop and increment the quality of the inks that are printable trying to up-scale the active area of the devices. The blade coating and bar coating look as the most promising ones because of the roll-to-roll compatibility.

- Another discussed topic is the presence of lead in the perovskite structure. Lot of researchers are trying to stabilize lead-free perovskite materials but, till now, none of these materials are promising for further studies because a big lack in stability, once exposed to oxygen. Anyhow, some recent studies show that the amount of lead needed to cover $1m^2$ with a 400 nm thick - photovoltaic module, is tiny (~ 0.4 mg). Moreover lead compounds are already well-known and are possible to recycle them. In [33], is showed the possibility to obtain high-performing perovskite-based solar cells by purifying the lead present in car batteries.

Said this, the most commonly used solvents for perovskite deposition are well known to be injurious to health. In particular the solvents commonly used (DMF, DMSO, NMP) are toxic, can penetrate the skin and are carcinogenic. While the amount of lead is low for large surfaces, if we think about a scale-up of the process for perovskite deposition, less hazardous solvents must be used. This can reduce the cost of reagents handling and future risks. Several groups tried to replace hazardous reagents but the performances are still lower than the state of the art. [34,35] Also the commonly used solvents for the deposition of other layers needed to build a solar cell device, are hazardous. For example the most used hole transporting material (Spiro-OMeTAD) is dissolved in chlorobenzene. In general, scientists and researchers should move forward a greener chemistry in order to permit the widest diffusion possible in optoelectronic market for perovskite based devices.

- The last discussed topic is about long-term stability. What is still missing is a more robust procedure to test the stability for perovskite devices. A strict control on high temperature and humidity stability is needed to permit the entrance in the market for perovskite based devices. To get into the market, perovskite has to be able to degrade as less as possible in working and environmental conditions. Recent encouraging results show the possibility to have a working device for several hours. [36]

The research approach that we decided to go through is mainly focused to fix the first and second open question point. The idea to develop inks to obtain large area devices, with an active material that is reproducible independently on the environmental conditions, stable at high humidity levels and room temperature for weeks after the deposition, stable during working conditions of light soaking and applied bias, printed from low boiling point and benign solvents. All these are small steps that might permit the entrance in the market for perovskite-based optoelectronic devices. The bigger is the impact of the research on solving these material's issues, the sooner will happen a big revolution in optoelectronic applications.

In this section, the possible applications exploited for Hybrid Organic-Inorganic Perovskite based technologies during my Ph.D. period are explained. I divided the section in two sub-sections: in the first sub-section there is a focus in the field of solar cells [37,38] and in the second one there is a focus on the field of photo-detection [39]. Both the sub-sections presents an introduction with a broad context of the application, the history and the physics in behind the working mechanism.

1.2 SOLAR CELLS

1.2.1 SOLAR CELLS: BROAD CONTEXT

Photovoltaic (PV) technology consists in producing electric energy in an environmentally clean way. This is one of the reason why PV electricity is appreciated by the public. Moreover it's unique for many applications of high social value and permits to provide electricity to people who are living both in metropolitan areas and in remote areas of the world.

The growth of the PV market has been very rapid in the last years of the XX century and it is expected to maintain the same behavior during the XXI century.

In the next years, photovoltaic is expected to become a world-wide industry, manufacturing and selling modules in almost all the countries. Crystalline Silicon technology, both mono-crystalline and multi-crystalline is, up to now, clearly dominant. It has about 90% of the market. Silicon is one of the most abundant elements in the Earth's crust but to be used must be purified. In fact, the Silicon used in today's solar cells is obtained mainly as off-grade polycrystalline-Silicon and scrap wafers from the microelectronic industry.

After this introduction, someone might ask 'why develop a totally different semiconductor technology for PV when Silicon is so well established?'. One of the answers is 'to achieve lower cost and improving the manufacturability at larger scales with respect to Silicon wafer-based modules'. In fact, Silicon crystals were expensive and slow to grow. It was also recognized that between all the semiconductors, Silicon would require the major thickness to absorb the light coming from sun. This is due to its optical properties. Silicon is the most weakly

absorbing semiconductor material used for solar cells because it has an indirect band gap while most of the other semiconductors used for PV have a direct one. Thicker active material means higher volume but is also implicit an higher quality material because the carriers generated in the semiconductor by photons, have to travel for longer paths before reach the external circuit to produce useful work and these characteristics leads to higher material cost.

Since the 1960s, was clear that other semiconductors could have been used for high performing solar cells and most of them exist in a form called thin films. When the thin film are fabricated into useful devices, they are so thin that they must be deposited on a "*substrate*" that is a layer needed only for mechanical support. Some Thin Film Solar Cell (TFSC) technologies are Cu_2S/CdS solar cells. They have been important to have led to the development of new theories to explain the device performances and new methodologies for processing the materials [40,41].
In 1980s, other thin-film technologies demonstrated the ability to cross the 10% efficiency barrier and become candidates for serious consideration: gallium arsenide – GaAs [42], amorphous Silicon – a-Si [43], cupper indium selenide/cadmium sulfide – $CuInSe_2$/CdS [44], and cadmium telluride/cadmium sulfide – CdTe/CdS [45].

Thin Film Solar Cells consist of 4 to 10 different layers and each of them has a different functions such as reducing resistance, forming the p-n junction, reducing reflection losses and providing a robust layer for contacting and interconnection between cells. Some of the layers could be as thin as only 10 nm and this requires excellent process control.
The main advantage of TFSC is that they may have lower costs than crystalline-Silicon-wafer photovoltaic technology once produced in large volumes. The lower cost for Thin Film Solar Cells come from the following characteristics:

- the active material is typically an hundred times thinner than Silicon wafers (~100 – 400 nm vs ~1 – 3 μm) usually deposited onto low-cost substrates such as glass or plastic.
- the active material is deposited continuously over large areas at much lower temperature (200 to 500 °C vs ~1400°C for crystalline-Si);

- the active material can tolerate higher impurity concentration, that is reflected to lower cost to purify the raw materials

In the 1990s, significant improvements in the Dye-Sensitized Solar Cells' (DSSC) performances were achieved, mainly thanks to the development of nano-porous TiO_2 electrodes in École Polytechnique Fédérale de Lausanne (EPFL) by Micheal Grätzel's group. The TiO_2 electrode has a large surface area and on top of TiO_2, a dye is absorbed. The dye that was used is a Ruthenium-complex, able to absorb wavelengths from 400 to 900 nm. Thanks to these devices was possible to achieve a power conversion efficiency, η, up to 10% under AM1.5 irradiation.
The DSSC technology has been intensively investigated worldwide, and its PV mechanism is now well understood [46,47,48,49,50]. The cost of commercially fabricating DSSCs is expected to be low because the cells are made of low-cost materials and the assembly is an easy process.

In the 2000s, Organics Photovoltaics took the floor. An organic solar cell is a particular type of PV that uses organic molecules or polymers as active material in the devices. This technology uses solution processable and cheap materials, permitting to obtain low cost devices, with a large-area compatible fabrication. Nevertheless, the devices might be also flexible and the molecular engineering permits to have an extremely high number of active materials, changing the band gap and the band alignment, allowing the tunability of the optical properties.
By engineering them, is possible to absorb a large amount of incident light, with only few hundreds nanometers of active material. Nowadays, the record efficiency for organic PV is around 17% for Tandem devices [51] and around 14% for ternary blend [52]. Some disadvantages associated to organic PV are lower efficiency, lower stability and a lower strength than Silicon PV. On the other hand, organic PV have usually a light weight and are much cheaper and printable. They might be fabricated in a custom way by changing the active material and they can find an important role in flexible electronics market and solar cells integrated in windows thanks to their high transparency.

In the 2010s, quantum dots (QDs) have been incorporated in PV to increase the efficiencies of converted light to electrical current [53]. The semiconductor QDs have an electronic structure and optical properties that are strongly size-dependent.
The QD technology presents the low-temperature solution processing, environmentally abundant active materials and is compatible with cheapness and flexible substrates. The QDs solar cells, have advanced fast from 1.8% in 2008 [54] to over 13% in 2017 [55] and a recent theoretical analysis of nanostructured thin film, QDs-based, suggest that efficiency can reach up to 15%.
The semiconductors usually used for this technology, are lead chalcogenides (PbSe, PbTe) nanocrystals, lead sulfide (PbS) or, more recently, perovskite-based QDs.

In 2013, a new TFSC has been discovered. The Hybrid Organic-Inorganic perovskite has been used for the first time in this year [56,57]. In the few following years overcome the efficiency of Silicon PV, reaching 23% [58] in single junction configuration and can reach 30% in Tandem configuration. The perovskite solar cells use as active material a perovskite-structured compound with lead or tin halide-based material. Perovskite materials such as methylammonium lead halides and all-inorganic cesium lead halide, are cheap to produce and, in principle, simple to manufacture.

With all the advantages of TFSC, why does crystalline-Silicon or multi-crystalline Silicon still dominate 90% of the world market? This brings us to the disadvantages of TFSC: they have a much less-developed knowledge and technology base compared to crystalline-Silicon. The companies have had to develop not only an understanding of the materials and devices but also the equipment and processing to manufacture them. The thin-film photovoltaic industry has had to develop the technologies all by itself with considerably less financial resources than the Silicon industry had. They were not able to adopt a mature technology like the Silicon photovoltaic community did from the Silicon electronics industry.

Consequently, low-cost alternatives and high-efficiency novel concepts, many already in development, are needed. Thin-film technology is still one of the candidates to take over from Silicon technology in the short to medium-term. So

that, the research on this application must be considered as public investment with strong public support and long-term human benefits.

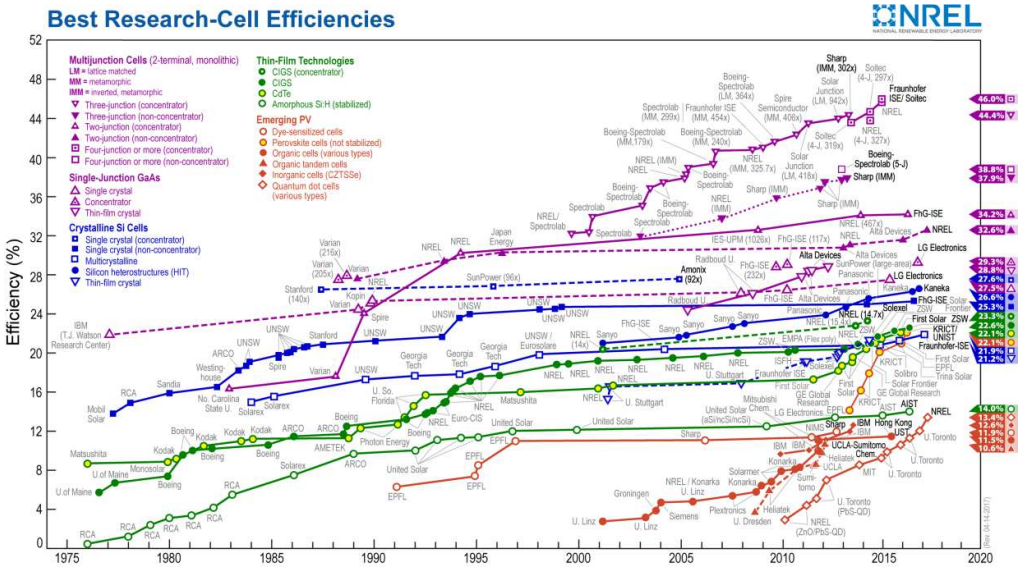

Figure 1.2.1.1 : Power Conversion Efficiency chart versus years for different photovoltaic technologies.[59]

1.2.2 SOLAR CELLS: THE PHYSICS IN BEHIND

A solar cell is an electrical device that converts the energy of light into electricity. In the solar cell devices is present an active layer, usually it is a semiconductor material. This kind of material have the capacity to absorb light and to transform it in a couple of carriers positively and negatively charged, called holes (h^+) and electrons (e^-), respectively.

A semiconductor solar cell, is a properly designed and engineered diode, able to efficiently absorb and convert light energy to electrical carriers that are collected and electrical current is produced.

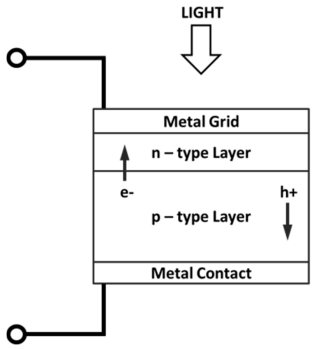

Figure 1.2.2.1 : Sketch for a solar cell. Electrons and holes are photogenerated in the active material and collected from an external circuit.

The diode needs an n-type semiconductor connected to a p-type semiconductor and they form a metallurgical junction. This is usually done by diffusion or implantation of specific impurities, called dopants. The metal contact and the metal grid are needed to collect the different charges and produce electricity.

The electromagnetic radiation is composed of elementary particles, called photons, which each has a specific amount of energy determined by spectral properties of the source. These particles exhibits also a wavelike character with a wavelength (λ) related to the photon energy (E_λ) by:

$$E_\lambda = \frac{h\,c}{\lambda}.$$

where h is the Plank's constant and c is the speed of light. Only quantum elements with an energy greater than semiconductor's energy gap (E_g) are able to generate

electron-hole pairs and will contribute to the energy conversion process. Said that, it is important to consider the solar spectra to efficiently design the solar cells.

The Sun has a surface temperature of 5762 K and the radiation spectrum can be approximated to the black-body radiator. As a black-body radiator, the Sun has an isotropic radiation and, being very far from Earth, the light can be thought as parallel streams of photons.

The Air Mass (AM) number is given by:

$$\text{Air Mass} = \frac{1}{\cos\vartheta}\,.$$

where ϑ is the incident angle ($\vartheta = 0°$ when the sun is overhead); follows that AM is always greater than or equal to one at the Earth's surface. The commonest AM used is AM1.5 spectrum normalized to a total power density of 1 kW/m^2 and the main losses with respect to the pristine black-body emission are due to absorption by chemical elements and molecules that are present in the Earth's atmosphere (oxygen, water, nitrogen, carbon dioxide…). The AM1.5 spectrum, presents the maximum amount of energy for a solar cell that can be converted in electrical current output.

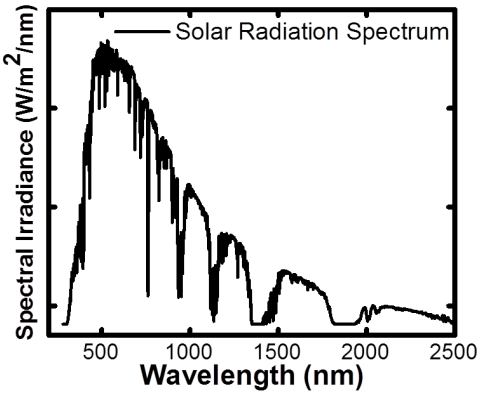

Figure 1.2.2.2 : Solar Radiation Spectrum vs wavelength.

As written before, semiconductor materials are crystalline materials. Having a crystalline nature means that the atoms are aligned in a periodic array. The periodicity and the atomic properties of the different elements are the cause of the electronic properties of the material. In fact, an electron moving in a semiconductor material is comparable to a particle confined in a three dimensional box, that feels the potential fields surrounding due to the presence of the atom's nuclei and the

core electrons. The dynamic behavior of the electron can be established from the electron wave function (ψ), which is obtained by solving the time-independent Schrödinger equation:

$$\nabla^2\psi + \frac{2\,m}{\hbar}[E - U(\vec{r})]\,\psi = 0 \ .$$

where m is the electron mass, $\hbar$ is the reduced Plank's constant, E is the energy of the electrons and $U(\vec{r})$ is the periodic potential energy inside the semiconductor's lattice. Solving this equation permits to obtain the band structure of the semiconductor materials and the relationship between the electron's energy and the momentum. Nevertheless, this equation tells us that the motion of the electrons in the crystal is approximated to an electron in free space with an effective mass (m^*) in the Newton's law:

$$F = m^* a \ .$$

where F is the applied force and a is the acceleration of the electron and m^* is defined as:

$$m^* = \left[\frac{d^2E}{dp^2}\right]^{-1} = \left[\frac{1}{\hbar^2}\frac{d^2E}{dk^2}\right]^{-1} .$$

From these equations is possible to derive the band energy diagram versus the crystal momentum (p):

$$p = \hbar\,\mathrm{k} \ .$$

where k is the wave vector, corresponding to the wave function solutions of the Schrödinger equation.

Energy bands below the valence band (VB) are presumed to be fully occupied by electrons and the energy bands above the conduction band (CB) are presumed to be empty. When the minimum of CB occurs at the same value of the crystal momentum as the maximum of the VB, the semiconductor is defined as a *direct band gap* material, while, when the maximum of the VB and the minimum of the CB are not align, the semiconductor is defined as *indirect band gap* material.

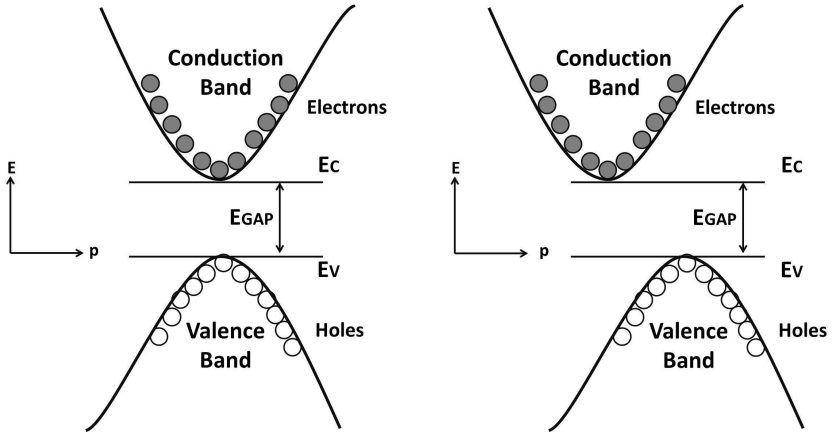

Figure 1.2.2.3 : Sketch of energy band: on the left a direct band gap material and on the right an indirect band gap material. The difference is whereas the maximum of the VB is aligned with the minimum of the CB or not.

The creation of electron-hole charges through absorption of light is fundamental for the operation of a solar cell device. The excitation of an electron directly from the VB, which leaves a hole behind, to the CB is called *fundamental absorption*. Both energy and momentum of all the particles involved must be conserved. The absorption coefficient for a given photon's energy (hv) is proportional to the probability (P_{12}) of the transition of an electron from the initial state (E_1) to the final state (E_2), and summed with the density of available final states:

$$\alpha\ (hv) \propto \sum P_{12} g\ v\ (E_1)\ g\ c\ (E_2)\ .$$

This is true if we consider that all the VB states are full and all the CB states are empty. Absorption is the result of the creation of an electron-hole pair after the photo-excitation of a free electron from VB to CB, leaving a free hole in the VB.

When a semiconductor is brought out of thermal equilibrium, for example upon illumination from a source of light, the concentration of holes (p) and electrons (n) tend to relax back to their equilibrium values through a process called *recombination*. During this process, an electron energetically falls from the CB to the VB. There are different recombination mechanism such as:

- Recombination through defects that form traps in the forbidden gap.
- Radiative recombination (also called band-to-band recombination).
- Auger recombination.

These recombinations are schematized in Figure 1.2.2.4.

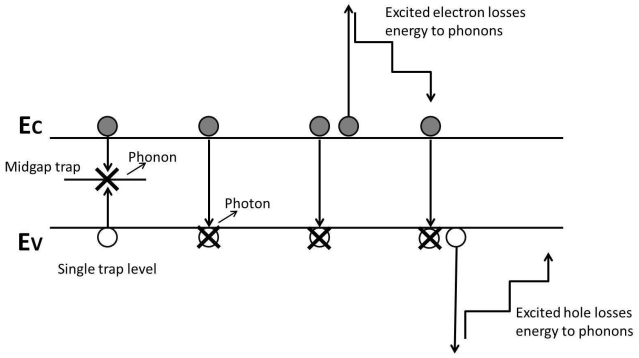

Figure 1.2.2.4 : Sketch of possible recombinations in a semiconductor material.

The rate of each recombination process can be determined by the Shockley-Read-Hall statistics: at low excitation densities, the photo-excited population decays with a mono molecular rate. If the photo-excitation density is increased, this decay channel reach the saturation and bi-molecular band-to-band recombination increases. At much higher photo-excitation densities, the three body interaction became more probable and Auger recombination takes place. All these recombination channels can take place in a system:

$$\frac{dn}{dt} = -k_{Auger}\, n^3 - k_{radiative}\, n^2 - k_{traps}\, n \ .$$

Where n is the excited carrier density and k_{traps}, $k_{radiative}$ and k_{Auger} are the rate constant for mono-molecular, bi-molecular and three-body recombination.

Once the carriers are photo-generated in a solar cell device, before they recombine through the different channels explained before, electrons and holes have to be collected.

This is done by applying an external electric field. If the semiconductor is uniformly doped, the bands bend upward in the direction of the applied field and the electron in CB, being negatively charged, move in the opposite direction of the field, while the holes, in the VB, being positively charged, move in the same direction of the applied field.

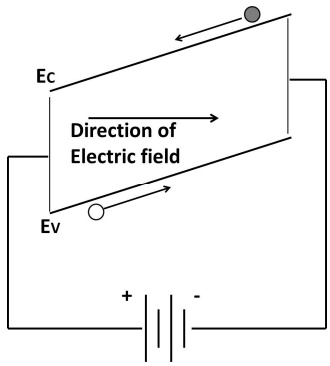

Figure 1.2.2.5 : Sketch of the drift in semiconductor material after photo-generation. The electric field can be created by the internal built-in potential of the junction or by an externally applied bias.

The simplest description for a solar cell in the ideal case is when the device corresponds to a perfect current generator and an asymmetric resistive element, called *diode*. A potential is applied at the terminals of the circuit.

The current voltage response of the device can be approximated to the amount of the current produced by the generator, called photo-generated current and the current generated by the diode with an opposite sign with respect to the first one.

The general formula for the current density is:

$$J\,(V) = J_{SC} - J_0\left(e^{\frac{e\,V}{K_B T}} - 1\right).$$

Where K_B and T are the Boltzmann's constant and the temperature, respectively. The short circuit current density (J_{SC}) and dark saturation currents (J_o) of the diode are given by the solar cell structure, the operating condition, the material properties. To understand a solar cell, is possible to associate it to an ideal current source in parallel with a diode and, the direction of the current source is opposed to the current flow of the diode.

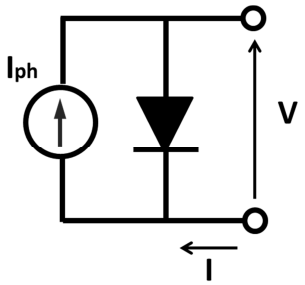

Figure 1.2.2.6 : An ideal solar cell can be modeled by an ideal current source in parallel with a diode.

To determine the efficiency of a solar cell device, the J-V characteristic is analyzed, where J is the current normalized on the active area of the device:

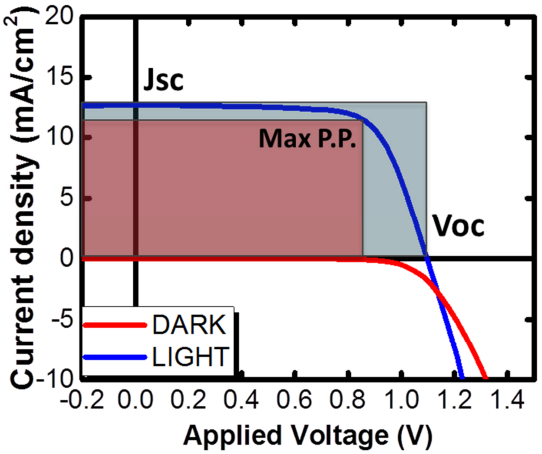

Figure 1.2.2.7 : J-V characteristic for a solar cell device. Red line for the dark current and the blue line, after exposure to light and photo-generation process.

An ideal solar cell, behaves in dark as a diode (red line in Figure 1.2.2.7). Upon exposure to light the charges are photo-generated and extracted from the device by an external applied bias. The figures of merit for a solar cell are:

- the short circuit current density (J_{SC}), that is the current density through the device when the voltage across the solar cell is 0 V.
- the open circuit voltage (V_{OC}) that is the maximum voltage available from a solar cell and it occurs when the current through the device is 0 mA.
- the maximum power point (*Max P.P.*) is the maximum power that can be generated from the solar cell device. It is defined as:

$$Max\ P.P. = V_{Max}\, J_{Max}\ .$$

- the *squareness* of the J-V characteristic defines the Fill Factor (*FF*):

$$FF = \frac{Max\ P.P.}{V_{OC}\, J_{SC}} = \frac{V_{Max}\, J_{Max}}{V_{OC}\, J_{SC}} = \frac{A}{B}\ .$$

- the Power Conversion Efficiency (*PCE*) or simply efficiency (η) that takes into account all the previous parameters and is defined as the ratio

between the power output and the incident power (P_{IN}) that depends on the properties of the spectrum used to excite the device:

$$\eta = \frac{P_{OUT}}{P_{IN}} = FF\frac{J_{SC}\,V_{OC}}{P_{IN}} .$$

When a real solar cell device is studied, two parasitic resistances have to be taken into account. The first one is called Shunt Resistance (R_{Sh}) and has no effects on the short circuit current but reduces the open-circuit voltage. The second one is called Series Resistance (R_S) and has not effects on the open-circuit voltage but reduces the short circuit current and it could come from the mismatch of energies band alignment.

Taking into account these two parasitic resistances, the circuit that describes a real solar cell, can be modified as a diode, one resistance in series and one resistance in parallel (Figure 1.2.2.8).

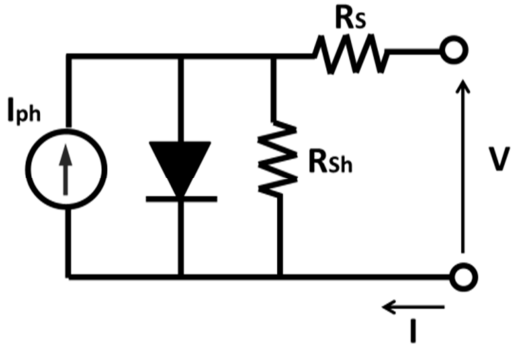

Figure 1.2.2.8 : A *real* solar cell can be modeled by an ideal current source in parallel with a diode and one resistance (shunt) and in series with another resistance.

The resistances now discussed are added to the previous formula and it is modified as follows:

$$J = J'_{SC} - J_0\left(e^{\frac{e(V+J\,A\,R_S)}{K_B T}} - 1\right) - \frac{(V + J\,A\,R_S)}{A\,R_{Sh}} .$$

where J'_{SC} is the sort-circuit current when there are no parasitic resistances that are considered in the other terms of the equation, A is the active area of the device and, to obtain the highest values for a solar cell device, the R_S have to tend to zero and the R_{Sh} have to be maximized, as explained in Figure 1.2.2.9.

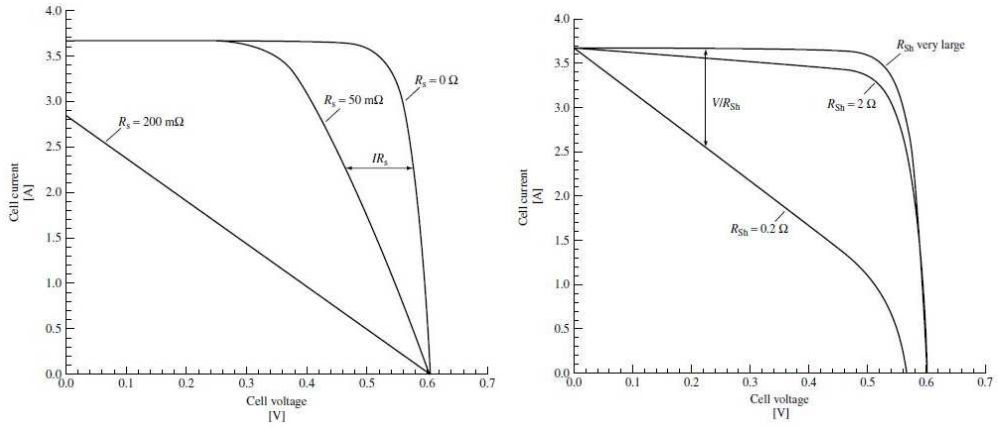

Figure 1.2.2.9: Effect of the parasitic resistances on I-V characteristic for a solar cell device: series resistance (on the left side graph) and shunt resistance (on the right side graph).

Finally the concept of multi-junction or tandem solar cell is explained. This concept appeared in the 1990s and is based on stacking more absorbing material with different band gap, opportunely engineered. Each material, will produce electric current in response to absorption of different wavelength and it allows to absorb a broader range of energies. This brings to a final improvement of solar cell efficiency. Since the components of the multi-junction are connected in series, the cell with minimum current density during the operation will limit the total current of the junction, while the open circuit voltage will be, theoretically, the sum of the open circuit voltage of the cells that are forming the multi-junction.

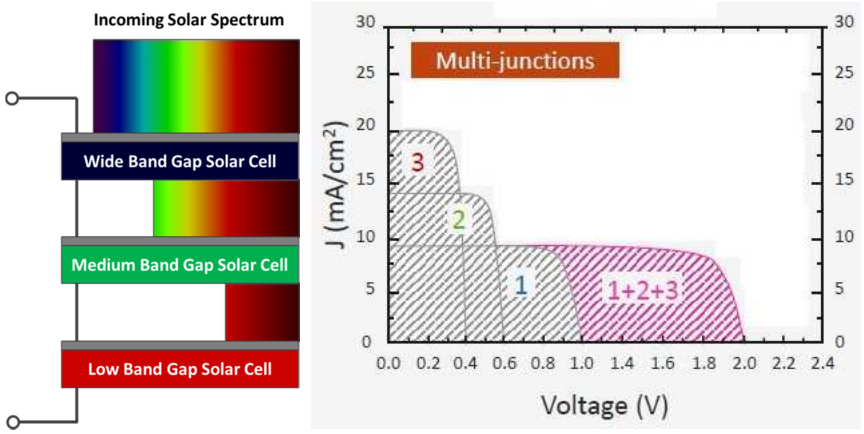

Figure 1.2.2.10: Sketch of a triple-junction on the left and J-V characteristic for a multi-junction solar cell. The current density is limited by the lowest and the open circuit voltage is the sum of all the open circuit voltages.

1.3 PHOTODETECTORS

1.3.1 PHOTODETECTORS: BROAD CONTEXT

A photodetector (PD) is a device sensitive to light or other electromagnetic radiation. It is able to convert the absorbed photons into electrical current, after creating electron-hole pairs.
The photodetectors are used in different fields in our daily life such as in automatic doors in the supermarkets and buildings, are used to receive the signal from remote controllers for televisions or stereos, in the CCD of a video camera, in different scientific instrumentation, in medicine or in fiber-optic connections.

1.3.2 PHOTODETECTORS: THE PHYSICS IN BEHIND

In principle, the basis are similar to what has been discussed in the previous section for solar cell devices.
Briefly, the photodetectors present an active material, usually a semiconductor. These materials are able to detect and absorb the incident light; the absorbed wavelength depends on the physical and chemical properties of the material and the bonds between the elements that constitutes the active material.
Upon absorption the semiconductor generates charges that are photo-generated and, before these charges recombine through different recombination channels already explained before, these carriers must be separated and travel through the semiconductor material. Thanks to an external applied bias they have to be extracted from the device, producing current.

In general, a photodetector device should be sensitive and fast; it means that should be able to detect low intensities in a certain range of wavelengths and the output current should be created in a reasonably fast time.
To resume, the figures of merit for a photodetector device are:

- the *dark current* is the current flowing in the photodetector device even in absence of incident light, upon applying a bias.

- the *responsivity* is defined as the ratio between the output current (I_{OUTPUT}) and the power of the incident light (P_{IN}) :

$$R = \frac{I_{OUTPUT}}{P_{IN}} \left[\frac{A}{W}\right].$$

as the optical power associated to a certain photon flux depends on the photon's wavelength, *R* can't be used to fairly compare photodetectors operating at different wavelengths. For this reason is often used the external quantum efficiency.

- the *external quantum efficiency* (*EQE)* is the quantum conversion parameter expressed by the number of incoming photons divided by the number of collected charges and is related to Responsivity by the following formula:

$$EQE = \frac{R\,\lambda\,q}{h\,c}\ .$$

- the *noise-equivalent power* (*NEP*) is the amount of power of light needed to generate a signal that is comparable in size with the noise of the same device.

$$NEP = \frac{(\overline{i_n^2})^{0.5}}{R(\Delta f^{0.5})} \left[\frac{W}{Hz^{0.5}}\right].$$

- the *specific detectivity* (D^*) is measured in *Jones* and it is defined as the ratio between the square root of the active area of the detector and the noise equivalent power:

$$D^* = \frac{(A)^{0.5}}{NEP} \left[\frac{cm\ \ Hz^{0.5}}{W}\right].$$

- the *gain* is the output current of a photodetector divided by the current produced by the incident photons on the detector.
- the *response time* is the time needed for a photodetector to go from 10% to 90% (or from 90% to 10%) of the final output when the light is switched on (or when the light is switched off).

To obtain performing photodetector devices, one of the goal of light-detection is the discrimination of the information carried by light signals over a random pattern called *noise*. The noise represents a random fluctuation of the electrical signal expected. This fluctuation, in electronic devices, could come from different mechanisms. The most relevant in this discussion, is the *shot noise* that is the noise intrinsically associated to the discrete nature of electric charge on carriers.

Let's consider a medium; this medium is characterized by a current flow (I) which identifies a surface perpendicular to its direction: the instant when a certain carrier cross this surface is not correlated with respect to the other carriers that are present, accordingly to statistic with Poisson's distribution. This random distribution on the electron passage is the origin of the fluctuations in the current value, which determines the shot noise in a device.

Usually the shot noise is much less significant to another noise present in electronic circuits: the *flicker noise*. This, called also *pink noise*, is a type of electronic noise with a dependence of 1 over the frequency (f). It comes from different effects such as the impurities in the conductive channel or generation and recombination of charges.

Finally, the last noise that is introduced, is the *white noise*. This is the lowest noise reachable in an electronic device and comes from a random signal having equal intensity at different frequencies.

Chapter 2

Experimental Methods

In the 2nd chapter of the Ph.D. thesis, are described the technical details of the research projects. Here are shown the instruments, the chemicals and the solvents that have been used during the Ph.D. period. In the final section are described the deposition techniques used for the active layers in the different devices realized. Moreover, is possible to find a section with all the details to reproduce the structures and the parameters used for the fabrication of the devices.

2.1 INSTRUMENTATION

Absorption:

The absorption measurements are performed with a Perkin Elmer Lambda 1050 spectrophotometer in a range between 300 – 900 nm.

Some of the absoprtion showed in chapter 3 are obtained by measuring reflectance spectra by using a PerkinElmer Lambda 1050 UV/Vis/NIR spectrometer equipped with a 150 mm integrating sphere.

X – Ray Diffractometer:

The X-ray diffraction spectra are obtained using a BRUKER D8 ADVANCE diffractometer with a Bragg-Brentano geometry equipped with an anode of Cu $K\alpha_1$

(λ = 1.544060 Å); the usual operating voltage is 40 kV and the current is set at 40 mA. All the diffraction patterns are collected at room temperature over an angular range (2θ) between 4° and 60° with step size 0.02° and an acquisition time of 1 second.

High Resolution – Scanning Electron Microscopy:

The HR – SEM images are collected by using an Ultra High vacuum Zeiss Supra 40 with GEMINI column FE-SEM. The electron energy is set between 3-5 kV, distance from the sample is set at 4 mm and magnification between 10k and 200k. High Efficiency In – Lens secondary electron detector was used during the images acquisition.

Profilometer:

The thicknesses of the different layers are measured by using KLA-Tencor Alpha-Step IQ Surface Profiler. The lengths scanned are 500 µm with a speed of 50 µm/s and a rate of sampling of 50 Hz. The value is the average of more measurement in different points of the same sample to check the uniformity of the deposited layer.

Solar Simulator:

The current density – voltage (J–V) characteristics are measured with a computer – controlled Keithley 2400 Source Meter. The simulator Air Mass 1.5 Global (AM 1.5G) irradiance is provided by a Class AAA Newport solar simulator. The light intensity is calibrated with a silicon based photodetector.

Steady-state Photoluminescence fluence dependent:

Excitation was provided by an unfocused CW diode laser with wavelength at 405 or 450 nm (Oxxius). The emission spectra was collected in reflection geometry and focused into a fiber coupled to a spectrometer (Ocean Optics MAYA Pro 2000). The emission was measured exposing the sample for 5 seconds and with intervals of 1 min between different fluencies. The measurements were taken on the same spot starting from low to high power and then back to low. The resulting spectra was integrated in the range of 400 to 700nm, divided by the laser power and then normalized to obtain the relative PL emission points shown in the graphs. All

measurements were taken at room temperature and in a vacuum chamber at ~10^{-6} mbar.

Photoconductor Measurements:

Responsivity and gain were measured using a spectrophotometer (Tungsten-Halogen Lamp with a monochromator) coupled with a Keithley 2300 source-meter. The light intensity across the spectrum from the spectrophotometer is in the range of tens of microwatts. A silicon photodetector (UV-818) is used for calibrating the light source. Photocurrents are always dark current subtracted and

$$I_{ph} = (I_{LIGHT}-I_{DARK}).$$

Gain reported is the external gain G_{ext} , defined as the ratio between the number of incident photons and the number of collected charges, taking also the expression:

$$G_{ext} = \frac{\text{Responsivity}(R) \times h \times \text{Frequency of Incident Light}(\nu)}{\text{electronic charge}(e)}.$$

Intensity dependent G_{ext} is determined using a diode laser at 560 nm, chopped at 1 kHz, with a 3 V applied bias.

The photocurrent is amplified with a DHPCA-100 Femto-transimpedance amplifier and the signal is recuperated with a Stanford Research 830 lock-in amplifier. The intensity is varied using neutral density filters.

The transient time response is measured using fast switching LEDs (λ = 532 nm, rise/fall time ~25 ns) and a DHPCA-100 Femto-transimpedance amplifier, connected to an oscilloscope. The measurements are done in a Faraday cage to minimize the noise.

Rise time (t_{rise}) and fall time (t_{fall}) is calculated by the time taken from the device to produce the photocurrent signal from 10 % to 90 % (rise) and from 90 % to 10 % (fall).

Bandwidth of the device is:

$$\frac{1}{(t_{rise}+ t_{fall})}.$$

The pulse width for the transient measurements are 500 µs, much larger than the device response speed to permit to the device photocurrents to saturate.

Noise measurements are performed over a range of frequency with a custom spectrum analyzer based on the cross-correlation technique.[60]

Two low-noise wide-bandwidth transimpedance amplifiers set the bias voltage of the device under test and measure the current flowing in the device. The output of the two amplifiers are band-pass filtered (10 Hz – 200 kHz), amplified and simultaneously converted in the digital domain. The cross-spectrum between the two signals is calculated, obtaining the current noise of the device with a reduced effect of the uncorrelated noise given by the transimpedance amplifiers. The device and the transimpedance amplifiers are shielded with a grounded metal box to reduce electromagnetic interferences. Bandwidth for the NEP is 1Hz.

The gain, for photo-transistors and photoconductors is function of incident light intensity and the comparison of performances are carried out at similar light intensities whenever possible. Bandwidth is calculated using the time taken for the change in photo-response signal (10%-90%).

2.2 MATERIALS

Chemicals:

- Lead (II) Iodide powder sold by Alfa Aesar (PbI_2 , 99.999% purity).
- Lead (II) Bromide powder sold by Merck ($PbBr_2$, $\geq$ 98% purity).
- Methylammonium Iodide sold by DyeSol (MAI).
- Methylammonium Bromide sold by DyeSol (MABr).
- Methylammonium Chloride sold by DyeSol (MACl)
- Cesium Carbonate sold by Merck (Cs_2CO_3, 99% purity).
- n-Octylamine sold by Merck.
- Phenyl-C61-butyric acid methyl ester (PCBM) sold by Solenne.
- Titanium (IV) Iso-propoxide sold by Merck.
- Lithium bis (trifluoromethylsulfonyl) imide (Li-TFSI) sold by Merck.
- 2,2',7,7'-Tetrakis[N,N-di(4-methoxyphenyl)amino]-9,9'-spirobifluorene (Spiro OMeTAD) sold by Lumtec Technology Corp.
- Zinc powder sold by Merck.

Solvents:

- Isopropyl Alcohol or propan-2-ol (IPA)
- Acetone
- n-n-dimethylformamide (DMF)
- Dimethyl sulfoxide (DMSO)
- Chlorobenzene (CB)
- Toluene (Tol)
- Propionic Acid (PrAc)
- Butylamine (BuAm)
- n-Hexane (Hex)
- 4-tert-butylpiridine (tBP)
- Acetonitrile (ACN)
- n-methyl pyrrolidone (NMP).

All the solvents are anhydrous and are bought from Merck.

2.3 DEPOSITION TECHNIQUES

Spin coating:

Spin coating is a technique used to depose thin film on flat substrates by using a spin coater machine. A reasonable amount of solution is put in the center of the substrate. The substrate starts rotating with a speed set by the user. The substrate is anchored to the spin coater by a rubber o-ring and a low vacuum.

Once the substrate start rotating, thanks to the centrifugal force, the solution is spread all over the substrate obtaining a thin and uniform film.

The thickness and the homogeneity of the produced film, depends on different parameters that can be set through the spin coater controller, such as the rotation speed of the substrate, the acceleration and the time set. Thickness is also determined by the concentration and viscosity of the solution or the conformation of the substrate. While the substrate rotates, the solution spread off the edges of the sample. Generally, the faster is the spin speed, the thinner is the film.

Bar coating:

Bar coating is a technique used to depose thin film on flat substrates by using a bar coater machine. A reasonable amount of solution is put on the edge of the substrate. A metallic bar passes with a certain speed and a certain groove, spread the ink and it forms a thin and uniform film.

The thickness and the homogeneity of the produced film, depends on different parameters, such as the viscosity of the ink, the speed of the metallic bar, the groove patterned on the bar. This technique is a large-area compatible deposition technique.

Spray coating:

Spray coating is a technique used to depose thin film on substrates by using a spray coater machine or air-pressurized spray gun. The gun can have different types of nozzles, shapes and sizes. This permit to obtain a uniform film, by optimizing the concentration of the ink used. The technique used in our laboratory is the manual mode, in which the air-gun is moved manually on the substrate, with a distance of about 10-20 cm. The deposition of the material permits to have, at the end, a continuous thin film.

2.4 ACTIVE MATERIALS

$MAPbI_3$ thin films:

The methylammonium lead tri-iodide ($MAPbI_3$) perovskite thin film strictly depends on the deposition technique. The one used in the experiments as a reference is the one described here. The precursors solution is prepared as follow: 140 mg of methylammonium iodide (MAI) and 430 mg of lead iodide (PbI_2) are dissolved in a mixture of 66.75 µL of anhydrous dimethyl sulfoxide (DMSO) and 933.25 µL anhydrous n,n-dimethylformamide (DMF) obtaining a concentration of 1 M.

The solution is kept stirring at 70 °C until the solution became yellowish but clear.

To depose the active layer, the solution is filtered with a PTFE filter with pore size of 0.22 µm and spin coated at 4000 r.p.m., 4000 r.p.m./s for 25 seconds. After 10 seconds of rotation, 300 µL of anhydrous toluene (Tol), is dripped on the sample.

The dripping of an orthogonal solvent permits to fastly remove the solvents where the precursors are dissolved in and the crystallization of the perovskite, immediately starts. To improve the crystallinity and to further remove the solvents that are present on the substrates, an annealing step is done at 100 °C for 10 minutes.

$MAPbI_3$ particles:

The synthesis of methylammonium lead tri-iodide (MAPbI3) perovskite particles is based on a cyclic approach with a successive reduction of the precursor PbI_2 particles size. In the first cycle, the starting PbI_2 precursor is obtained by grinding the as-bought powder in a ceramic mortar, under nitrogen atmosphere. This procedure permits to increase the PbI_2 surface area. Then, the PbI_2 is slowly added into a 100 g/L concentrated methyl ammonium iodide (MAI) solution in propan-2-ol (IPA) under stirring at 80 °C. As soon as the PbI_2 is added into the MAI solution, a fast insertion of MA^+ and I^- ions occurs into the PbI_2 lattice, inducing the growth of black $MAPbI_3$ cubic-like crystals. Such formed particles are subsequently isolated through sedimentation and decantation of the residual MAI solution and washed with isopropanol for two times. After this first cycle, we obtain $MAPbI_3$ particles with size of a few (1 to 5) micrometers.

By repeating the cycles is possible to reduce the average size of $MAPbI_3$ particles. Is possible to re-dissolve the particles in water under ambient conditions, without specific environmental control. The water addition promotes rapid extraction of MA^+ and I^- ions from the perovskite lattice that collapses immediately into water poorly soluble, PbI_2 particles, which are afterwards additionally rinsed with IPA to remove residual MA^+ and I^- ions. The recrystallized PbI_2 particles appear in the form of thin sheets, indicating layered structure of PbI_2 and are smaller in size than the starting precursor.

The obtained PbI_2 sheets are then adopted as precursors for a new cycle, following the same procedure described before and obtaining sheets with decreasing lateral dimensions and thickness at each step. Starting from smaller PbI_2 sheets, correspondingly smaller cubic perovskites particles can be isolated.

By applying the synthetic cycle three times, $MAPbI_3$ particles are obtained with characteristic size well below 1 μm.

$CsPbBr_3$ Nanocrystals:

Cs_2CO_3 is dissolved in Propionic Acid (PrAc) with a concentration of 2 M. $PbBr_2$ is dissolved in a mixture of IPA:PrAc:Butylamine (ratio 1:1:1) with a concentration of 0.5 M.

5 µL of the first solution are injected in 3 mL of a poor solvent. The antisolvent is a mixture of n-Hexane (Hex) and Isopropanol (IPA) with a ratio 2:1.

Immediately after the first injection, 100 µL of the second solution are injected under vigorous stirring in the solution in which the perovskite has poor solubility. When the precursors react, the solution turns green because of the nucleation of the nanocrystals that grow in size and are formed within few seconds. After stirring for 10 seconds, the formation of the nanocrystals is complete and the solution is centrifuged at 1000 r.p.m. for 2 minutes. This permits to remove the unreacted products and to collect the NCs that are then washed twice with Toluene (Tol) still through centrifugation steps. The final dispersing solvent can be changed by changing the deposition technique. This permits to have better morphologies of the active layers.

$MAPbBr_3$ Nanocrystals:

In a typical synthesis of methylammonium lead tri-bromide ($MAPbBr_3$) nanocrystals, a mixture of 0.16 mmol of methylammonium bromide (MABr) and 0.20 mmol of lead bromide $PbBr_2$ is dissolved in 5 mL of n,n-dimethylformamide (DMF) with 20 µL of

n-octylamine to form a precursor solution with 0.4% v/v of ligands. 100 µL of precursor solution is dropped into 10 mL of anhydrous chlorobenzene (CB) kept under vigorous stirring. The perovskite nanocrystals are immediately formed and they are purified by centrifugation steps at 7000 r.p.m. for 10 minutes. The biggest-size nanocrystals precipitate and are discarded. The obtained bright green colloidal solution is further investigated.

2.5 DEVICE FABRICATION

Solar Cell:

The standard structure solar cells are produced starting with a commercial Fluorine doped Tin Oxide (FTO) coated on glass with a substrate size of 2.5 x 2.5 cm^2. They are etched to obtain the desired pattern with Zinc powder and Chloridric Acid (HCl) 2M. The substrates are cleaned with a swab and IPA to remove glue residual and then immersed in a ultrasonic bath with a sequence of a mixture of Hellmanex detergent with a concentration of 2% v/v and distilled water, two steps in distilled water, IPA, Acetone, IPA. Each step last about 10 minutes. After the washing procedure, the substrates are dried with a N_2 gun, to help the evaporation of the solvent and not leave halos on the surfaces. To remove the last organic residual that can be present on the samples, 10 minutes of surface treatment are then done with a O_2 plasma etcher.

The Electron Transporting Layer (ETL) used is a compact Titanium di-Oxide (TiO_2). The solution is prepared as follow: 140 µL of Titanium (IV) Iso-propoxide is added to 1mL of IPA and, in another vial, 5 µL of HCl (2M in distilled water) are added in 1mL of IPA. The two solutions are mixed and the obtained mixture is firstly filtered with a PVDF filter with a pore size of 0.22 µm and then spin-coated at 2000 r.p.m., 2000 r.p.m./s for 45 seconds.

The spin coated substrates are placed on a hot plate able to reach 500 °C to permit the sinterization of the compact TiO_2. The annealing procedure last 45 minutes.

Once the substrates are cooled down, the active layer can be deposited, accordingly with the different deposition technique needed.

The Hole Transporting Layer (HTL) used in our standard structure is a Spiro-OMeTAD layer. It is deposited inside a N_2 filled glovebox at 1500 r.p.m., 1500 r.p.m./s for 45 seconds. The HTL solution is prepared as follow: 75 mg of Spiro OMeTAD is dissolved in 1 mL of chlorobenzene. Once the powder is dissolved, 29.88 µL of tert-ButylPiridine (tBP) and 18.11 µL of a stock solution with a concentration of 520 mg/mL of Lithium bis (trifluoromethylsulfonyl) imide (Li-TFSI) in Acetonitrile, are added and the solution is kept under stirring.

After the deposition, this HTL has to be oxidized to increase the conducibility. To do this, the sample is kept in dry air, for 12 hours. Finally, the metal contacts are deposed by thermal evaporation with a thickness of 75 nm. Thanks to an increase in

voltage is possible to sublimate a metal in a low pressure ambient (10^{-6} mbar). This permits to depose onto the samples, the desired pattern, after an opportune masking. The active are that are used on the different projects are 0.0935 cm^2 and 1.00 cm^2.

Planar Perovskite Photodetector:

Low-alkali 1737F Corning glass was used as substrate. The bottom electrodes are patterned by a lift-off photolithographic process, defining 2.5 µm channel length. The electrodes are obtained by thermal evaporation using a shadow mask. The composition is 1.5 nm thick Chrome used as adhesion layer on glass and 25 nm thick gold. The lift-off process to remove the unexposed light part is done by dipping the samples in a N-Methyl-2-pyrrolidone (NMP) bath overnight.

The substrates are then cleaned in an ultrasonic bath of distilled water, IPA, Acetone and IPA, 10 min for each step and finally exposed to O_2 plasma etcher for 10 min to remove the last organic residuals.

The developed inks are deposed in air by using a bar coater with a TQC Automatic Film Applicator. The stainless cylindrical steel bar used has 10 µm wire diameter and the speed is set at 30 mm/s. Different layers of active inks can be deposed in sequence, permitting to increase the thickness of the layer.

For PCBM passivation a 10 mg/mL solution of [6,6]-phenyl-C61-butyric acid methyl ester (PCBM) in chlorobenzene is prepared and then spin coated on top of the active layer at 2000 r.p.m., 2000 r.p.m./s for 30 seconds.

Chapter 3

High Detectivity Perovskites Light Detectors Printed in Air from Benign Solvents

In the 3rd chapter of the Ph.D. thesis, the project on photodetectors is described. Here is possible to find the details of the novel synthesis conceived in our group without the use of hazardous solvents, commonly used for perovskite-based applications. After the synthesis details and the characterization of the material obtained, is discussed the possibility to print the formulated inks on specific substrates permit to obtain light detectors with high specific detectivity, low noise and fast time response.

Light detectors is one of the real possible applications for halide perovskites that can be achieved in a short to medium time-frame. In fact light detectors require some of the key properties that mark the halide perovskite as a unique material for solar cells. Notably, this material has large absorption coefficients of 10^5 cm^{-1} in the visible and UV range, and long carrier lifetimes.[61,62,63,64]. On top, solution processability would result in a drastic simplification and affordability of the

manufacturing processes, leaving ample room for advanced pixel and array design for imaging applications, for example.

Nowadays, there are still a few aspects that limit the potential of perovskites for light detection and, in general, the use for consumer electronics. The first one is about toxicity of lead-based compounds and it is probably the most discussed topic. On this side, researchers are already trying to develop lead-free materials. Moreover recent studies demonstrate also the possibility of fully recycle the lead present in exhaust car batteries [65] or in the active layer of the opto-electronic devices [66] thus getting away from the practical and expensive issue of disposal of hazardous materials.

Another important aspect is related to the presence of the organic solvents that are often used to process perovskite thin films. These solvents present health and environmental hazards and high boiling points.[67] These aspects complicate the deployment of energy efficient fabrication processes and increases the environmental impact and the cost of waste handling. On top of that, the precursors-based approach restricts the available process window.[68,69,70,71]. In fact the final microstructure, which dominates the optoelectronics properties of the light absorbing layers, depends on how the constituent ions self-assemble during the crystallization process on the selected substrate, a complex function of the ratio of precursors, the solvents that are involved, processing additives, the substrate roughness and surface energy, atmospheric/environmental conditions, annealing temperature and treatment time.

Both the use of hazardous solvents and the difficult control of the polycrystalline structure might limit the advantages presented by perovskite as emerging technology but particle-based ink formulations in safer and more environmentally friendly solvents can represent a successful strategy to permit to the new technology to arrive on the market soon.

3.1 $MAPbI_3$ PARTICLES SYNTHESIS AND INKS FORMULATION

To synthetize methylammonium lead tri-iodide ($MAPbI_3$) perovskite particles, a cyclic approach is designed. It is based on the successive reduction of the size of precursor PbI_2 particles.

A schematic illustration of the process is shown in Figure 3.1.1. The starting PbI_2 precursor is obtained by grinding as-bought PbI_2 powder in a ceramic mortar, under nitrogen atmosphere, to increase its surface area. PbI_2 is slowly added into a highly concentrated (100 g/l) methyl ammonium iodide (MAI) solution in propan-2-ol (IPA) under stirring at 80 °C. Upon PbI_2 addition into the highly concentrated solution of MAI, immediate insertion of MA^+ and I^- ions into the PbI_2 lattice follows, inducing the growth of $MAPbI_3$ cubic-like crystals and turning the MAI solution into a dispersion of black perovskite particles. The formed particles are subsequently isolated through sedimentation and decantation of the residual MAI solution and washed with IPA twice.

After this first cycle, we obtain $MAPbI_3$ cubic-like particles with characteristic size of a few (1 to 5) micrometers (Figure 3.1.2a).

The successive cycles permit to reduce the average size of $MAPbI_3$ particles. To start the iteration, the latter are re-dissolved in water, in ambient atmosphere without specific environmental control. The presence of water promotes rapid extraction of MA^+ and I^- ions from the perovskite lattice that immediately collapses back into water poorly soluble, PbI_2 particles, which were afterwards additionally rinsed with IPA to remove residual MA^+ and I^- ions. The recrystallized PbI_2 particles appear in the form of sheets, indicating layered structure of PbI_2, [72] and are smaller in size than the starting PbI_2 precursor.

For example, after the first rinse of perovskite particles with water we obtained PbI_2 sheets with lateral sizes of a few micrometers (Figure 3.1.2b) and thickness of several hundreds of nanometers.

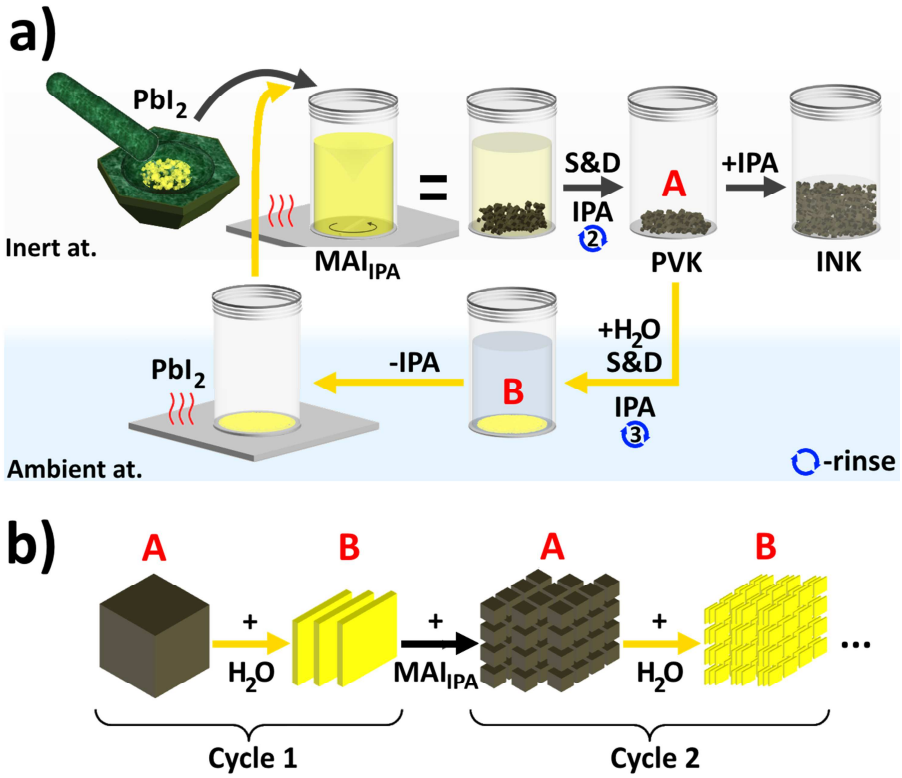

Figure 3.1.1: Synthesis of $MAPbI_3$ particles. a) Schematic representation of cyclic $MAPbI_3$ synthesis. b) Scheme of the effect of synthesis cycles on the characteristic size of perovskite particles (A) and lead iodide sheets (B).

The obtained PbI_2 sheets are then adopted as precursors for a new cycle, following the exact same procedure described before. It permits to obtain sheets with decreasing lateral dimensions and thickness at each step. Starting from smaller PbI_2 sheets, correspondingly smaller cubic perovskite particles are formed. Few years ago, Ha et al. determined a linear relation between the thickness of PbI_2 sheets grown in the (001) direction and the resulting perovskite platelet thickness grown out of it when gas-induced transformation is applied.[73] Following that, we think that the size of cubic perovskite particles depends on the PbI_2 sheet thickness.

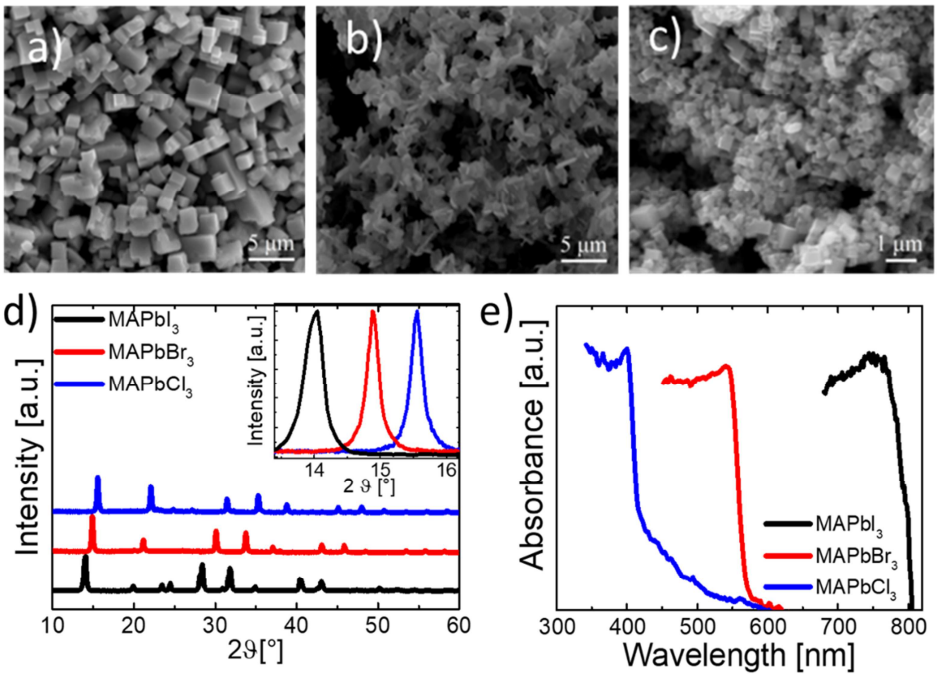

Figure 3.1.2: Characterization of Synthesized Particles. Top view SEM images of (a) first cycle synthesis $MAPbI_3$ particles, (b) recrystallized PbI_2 sheets and (c) final $MAPbI_3$ particles. (d) X-Ray diffraction spectra and (e) absorption band edges of synthesized $MAPbI_3$, $MAPbBr_3$ and $MAPbCl_3$ particles.

By repeating the synthetic cycle three times, we were able to obtain $MAPbI_3$ particles with size well below 1 µm (Figure 3.1.2c). Further synthetic cycles do not lead to further reduced particles size. X-ray diffraction measurements confirmed that the incorporation of MA^+ and I^- ions into PbI_2 to form $MAPbI_3$ is complete: the corresponding spectrum (Figure 3.1.2d) shows the characteristic peaks for $MAPbI_3$ at 14.1°, 28.4° and 31.8°, corresponding to the reflection of the (110), (220) and (310) crystal planes, respectively. No unreacted MAI or PbI_2 (main peaks at 10° and 12.7°, respectively) were detected.

Starting from the synthesized $MAPbI_3$ particles, tuning of the energy bandgap can be achieved through halide exchange. Halide exchange in the $MAPbX_3$ lattice has been previously reported and it is a facile strategy to tune the semiconductor bandgap. Starting from $MAPbI_3$, $MAPbBr_3$ or $MAPbCl_3$, full conversion or mixed halide perovskite ($MAPbI_{3-x}Br_x$, $MAPbI_{3-x}Cl_x$, $MAPbBr_{3-x}Cl_x$), can be obtained if the starting solution is stirred at 65 °C in presence of MAI, MABr or MACl.

The XRD spectra of the materials between the different steps of synthesis is showed in Figure 3.1.3. Is it possible to confirm that at the end of each step, no structural differences are found.

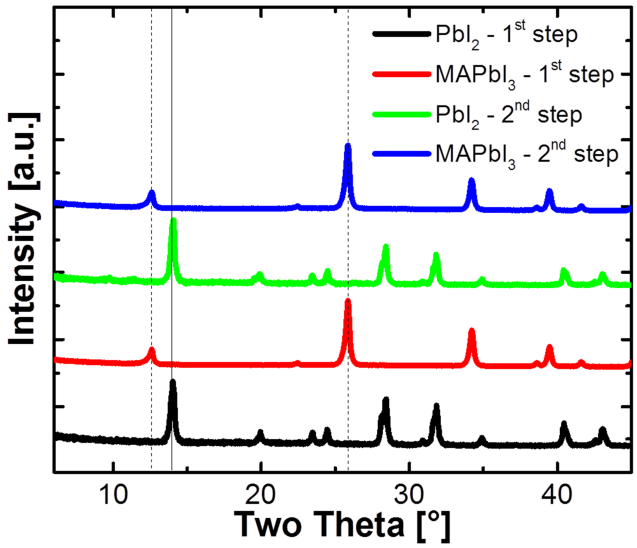

Figure 3.1.3: X-Ray diffraction spectra for different steps during the synthesis of the material used for the devices. Each material presents his own characteristic peaks with no differences after water addition and removal.

The material sinthetized by the synthesis technique developed by our group, has been tested for stability over weeks after deposition on glass substrate. For comparison a thin film $MAPbI_3$ perovskite is deposited by spin coating. The analysis that easily permits to observe the degradation of perovskite material is the X-Ray diffraction technique. In Figure 3.1.4 the main peak of XRD spectra over weeks for the material obtained with our synthesis and a thin film perovskite deposited by standard spin coating is showed. On the left side picture, is possible to see a small hydratation of the perovskite (peak at 10.3°) starting from the 4th week, while for spin coated $MAPbI_3$, the hydrateted peak compares after only one week exposure time and the main perovskite peak is almost disappeared.

The two samples are very different in thickness. To fearly compare the two samples we should have comparable thicknesses. Unfortunately, by spin coating technique, is difficult to reach 5 µm in thickness. Said that, it's anyway possible to see the different behaviour of the two samples once exposed to 70% moisture and 23 °C, confirming that our bulky material has a better resistance to moisture.

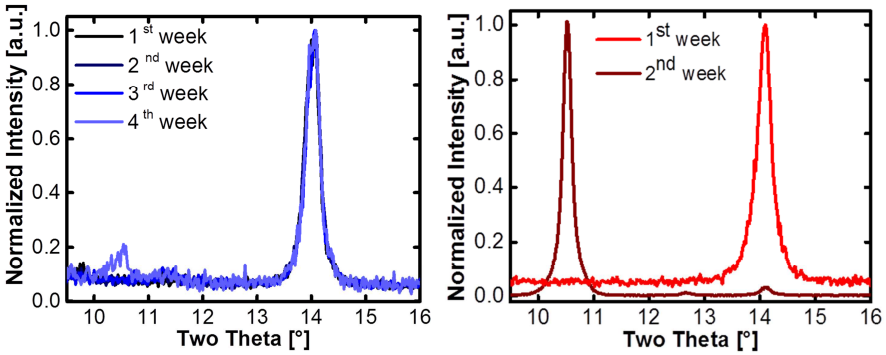

Figure 3.1.4: Normalized X-Ray diffraction main peak of the material deposited on glass after weeks. Our crystals (on the left) and standard spin coating (on the right side). The sample are both stored in air at 70% moisture and 23 °C.

The synthesis and characterization of the material has been done in collaboration with Dr. Peter Topolovsek.

3.2 PRINTED LIGHT DETECTORS

The formulated inks can be printed on different kind of substrates in ambient atmosphere, by bar coating, a large area and roll-to-roll compatible coating technique [74,75] (Figure 3.2.1).

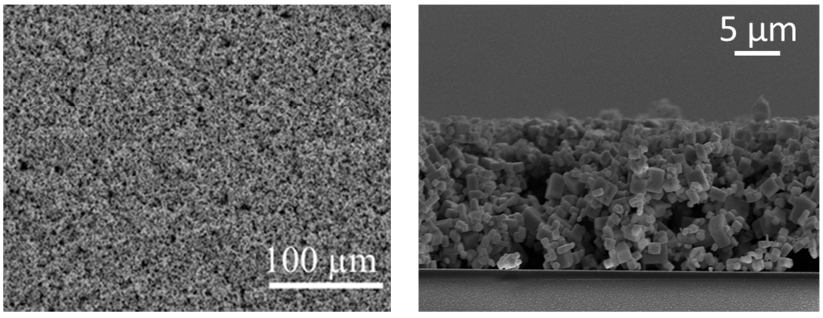

Figure 3.2.1: Top view image of printed perovskite particles showing complete coverage (on left side) and cross-sectional SEM image of printed perovskite particles (on right side).

After a first optimization on how to print the material on bare glass, a simple planar structure for gold electrodes is used. The interdigitated electrodes are made by

photolithography technique and, on top of them, the $MAPbI_3$ crystals solution is printed to obtain the photodetectors (Figure 3.2.2a).

These devices show a symmetric current-voltage (*I-V*) characteristics and a tangible light sensitivity with respect to the dark when exposed to a monochromatic radiation at 532 nm of 1 mW/cm^2 (Figure 3.2.2c).

The spectral responsivity as function of wavelength ($R(\lambda)$) is comprised between 0.1 A/W and 1 A/W (Figure 3.2.2d) in the visible range from 400 nm to 800 nm with an applied bias of 5 V on the device.

These performances are drastically improved when a layer of fullerene-derivative called [6,6]-phenyl-C61-butyric acid methyl ester (PCBM), is added on the printed perovskite layer particles acting as electron accepting layer. Due to the presence of voids among particles, the solution can permeate through the film of photoactive layer that has a thickness of few microns; the permeation brings to a full coverage with PCBM on the surfaces of the printed perovskite cubic-like particles (Figure 3.2.2b).

After the deposition of PCBM layer, the response to light is drastically raised: the perovskite/PCBM structure shows a dark current of 9 nA, an order of magnitude higher than for the bare perovskite and when the device is exposed to the same radiation as before, the photocurrent reaches 4.1 μA, three orders of magnitude more than in dark. Such strong photo-activity of the printed $MAPbI_3$ crystals with the PCBM coating device corresponds to a ($R(\lambda)$) that varies between 10 A/W and 78.7 A/W within the same spectral range (from 400 nm to 820 nm) and the shape corresponds to the absorption onset of the semiconductor (Figure 3.2.2d).

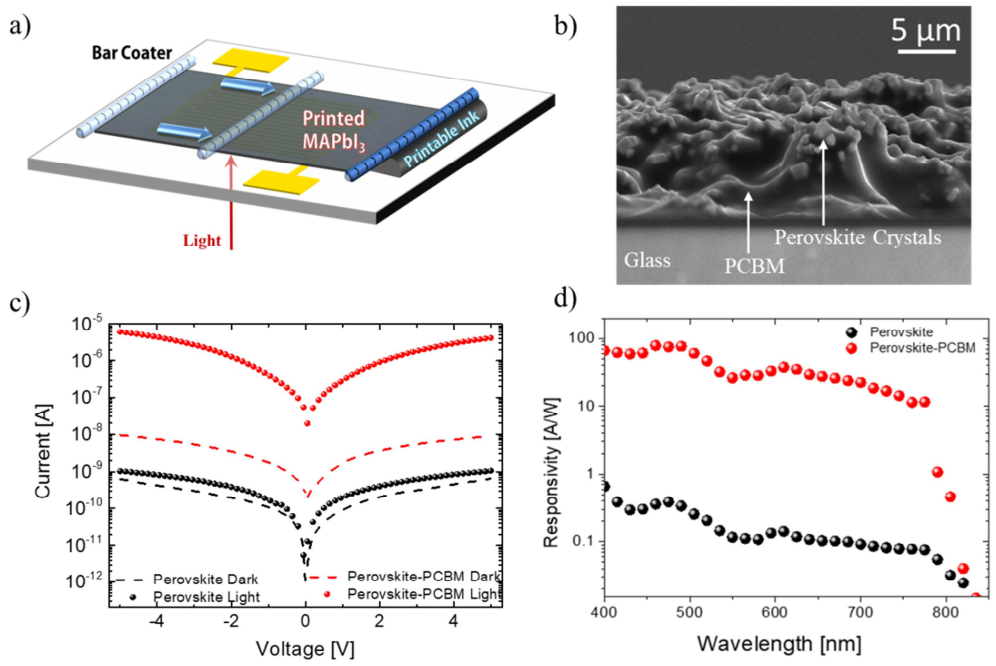

Figure 3.2.2: (a) Schematic image of the perovskite photoconductor printed on a simple planar geometry with gold electrodes (channel width, W = 20 mm and channel length, L = 5 µm). (b) Cross-sectional SEM image of the printed perovskite active layer with PCBM penetrating the film. (c) Dark and light (532 nm LED light, 1mW/cm^2) *I-V* characteristic curves of the device with and without PCBM. (d) Responsivity of the printed perovskite photodetectors with and without PCBM at 5 V applied bias.

An important selling point for our printed photodetectors is the stability; not only from the material point of view, thanks to the innovative synthesis but also the stability of the device itself under working conditions.

It's well-known in literature that $MAPbI_3$ material lacks in terms of photo-stability and when a bias is applied because of the ion motion through defects in the crystal lattice. [76]

In Figure 3.2.3 is showed the stability under continuous light soaking from a white LED with an intensity of 1 mW/cm^2 for different time (from 0 to 60 minutes).

The overall performances look stable both in dark and light conditions but, with a proper scale, in the current versus voltage graph under light can be noticed a small reduction in the performances of the device, highlighting a slow but continuous degradation over time of the material.

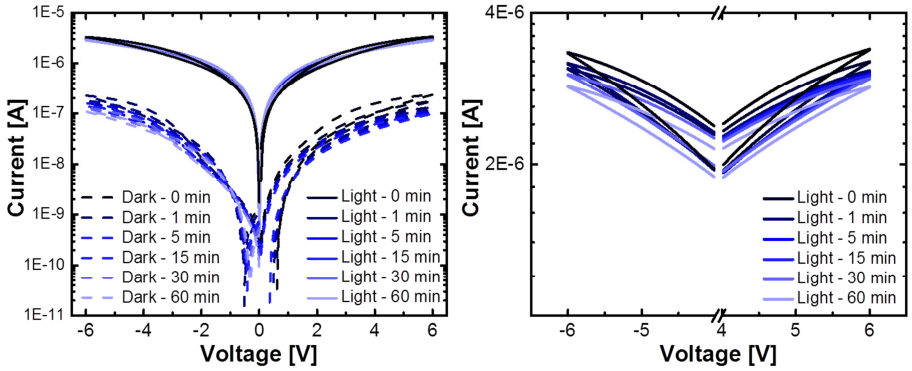

Figure 3.2.3: Current versus Voltage characteristics under dark and light conditions after different time of light soaking (on the left side) and zoom on light only (on the right side) to observe the degradation of the material over time.

Another important parameter to check for the devices is the shelf life-time stability. Keeping the device in dark condition and in nitrogen atmosphere, the lifetime is monitored over days and the performances are showed in Figure 3.2.4.

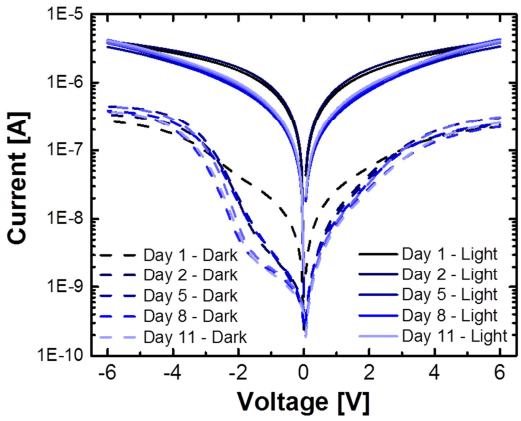

Figure 3.2.4: Current versus Voltage characteristics in dark and light condition over 10 days of storage in dark and nitrogen.

From the combination of high responsivity values ($R(\lambda)$) achieved with a low applied bias of 5 V over a channel length of 5 µm, a gain mechanism is suggested. [77,78]

In fact, the external quantum efficiency (*EQE*) calculated in the blue region of the spectrum overcome the value of 100%. Such *EQE* value, together with the symmetric $I - V$ characteristic curves, indicates a photo-conductive nature of the photodetector. The external gain (G_{ext}) that is defined as the ratio between the

number of collected photo-generated carriers and the number of incident photons is estimated to be 213 at a wavelength (λ) equal to 460 nm (Figure 3.2.5).

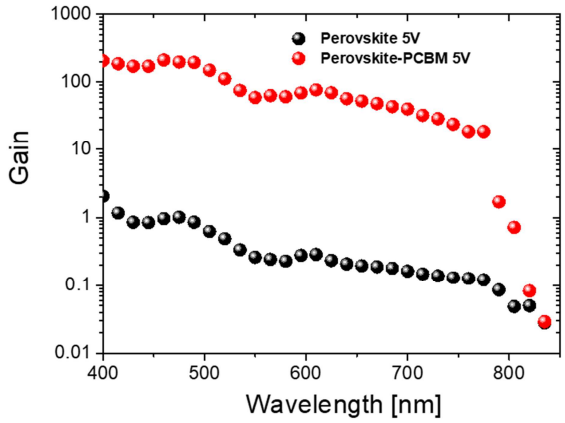

Figure 3.2.5: Gain as a function of incident wavelength are plotted for photodetectors with and without PCBM passivation layer.

The obtained gain is one order of magnitude higher than in any printed perovskite photodetector reported so far (Table 3.1). The photocurrent and G_{ext} as a function of the incident light intensity are reported in Figure 3.2.6a. At the low excitation density of 2 $\mu W/cm^2$ (λ = 560 nm), the gain increases from about 6, in the case of the pristine perovskite device, to 180, when the perovskite is coated with PCBM. By increasing the light intensity of almost 6 orders of magnitude, the gain quickly vanishes below 1 for the pristine material, while such decrease is strongly limited in presence of PCBM, with a gain which is still higher than 1 above 1 W/cm^2 (G_{ext} = 1.44 at 1.31 W/cm^2). Moreover, with addition of PCBM, the photocurrent is a power law of light intensity, i.e. $\propto I^{\alpha}$ with α = 0.68, on the base of which it is possible to easily retrieve the input light signal from the recorded photocurrent [79,80,81]

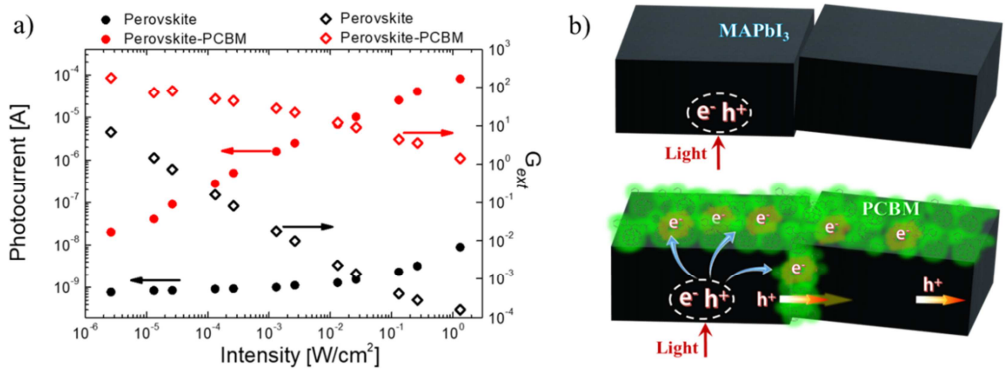

Figure 3.2.6: (a) Photocurrent and G_{ext} versus the incident laser light intensity with λ = 560 nm for photodetectors with and without PCBM. (b) Schematic representation of the photoconduction mechanism; the PCBM molecules serve as acceptor and trap for photo-generated electrons and as passivation of particles surface traps. These effects facilitate holes transport and boost both G_{ext} and Bandwidth of the detectors.

In a photoconductor device the gain originates from a strong unbalance in the transport properties of the photo-generated charge carriers following the absorption of a photon, where one of the two carriers is deeply trapped, and the other can drift under the external field. Once the mobile carrier is collected at the electrodes, another carrier is injected on the opposite electrode for charge neutrality. Recirculation of the carrier proceeds until the trapped carrier is finally released, determining the gain (G) that is proportional to the ratio between the de-trapping time and the transit time:

$$G = \frac{\tau_{\text{de-trapping}}}{\tau_{\text{transit}}} .$$

where $\tau_{\text{de-trapping}}$ is the time needed for a charge carrier to be de-trapped and τ_{transit} is the time needed for a charge carrier to circulate in the device.

The presence of unbalanced charge transport in pristine $MAPbI_3$ material upon photo-excitation has been recently reported, [82,83] moreover, the high work function of gold used for the electrodes in these devices introduces a high energy barrier for the injection of electrons for photoconduction, while promote the recirculation of holes.

This effect explains the behavior observed for the detector based on pristine perovskite. At low light intensity the gain is high since trapping of one of the two carriers by defect states and selective barrier for electrons at the contact unbalance the transport. As traps are filled with increasing intensity, the transport becomes more balanced and/or the trapping time of the less mobile carrier reduces and the gain is correspondingly smaller.

As reported in literature, [84,85] PCBM has a passivation effect when deposited on the perovskite thin film (Figure 3.2.6b). PCBM, as a Lewis acid, it is able to oxidize negatively charged PbI_3^- anti-sites or under-coordinated halide ions which work as deep traps for holes. Moreover, by penetrating through the printed porous film of perovskite particles, PCBM significantly improves the hole conductivity allowing the carriers to more easily drift through the particles under the externally applied bias and it also acts as a sink by extracting photo-generated electrons from the perovskite phase. In such a way, the lifetime of the free holes in the perovskite is further increased, while electrons are confined in the PCBM phase with short diffusion length. All this results in a 30 times enhancement in gain at low excitation density (~ $\mu W/cm^2$), and in a G_{ext} still higher than 1 at high excitation density (~ W/cm^2). Since electrons are extracted from the perovskite phase in the PCBM treated device, the device is less sensitive to light intensity, explaining the markedly different intensity dependence of photocurrent and gain between pristine and PCBM coated perovskite.

3.3 PHOTORESPONSE TIME

The photoresponse time is an important figure of merit for a photodetector device. Usually in these devices is present a trade-off between gain and response speed, or bandwidth.

In our devices the time response is evaluated by irradiating the samples with a 500 µs light pulse train and recording the transient photoresponse. The printed detectors follow very well the train of pulses (showed in Figure 3.3.1a and Figure 3.3.2a). The rise and fall times defined as the time taken by the photocurrent to rise from 10 % to 90 % of the regime value, and vice-versa, are 14 µs in both cases for the photoconductor coated with PCBM (Figure 3.3.1b).

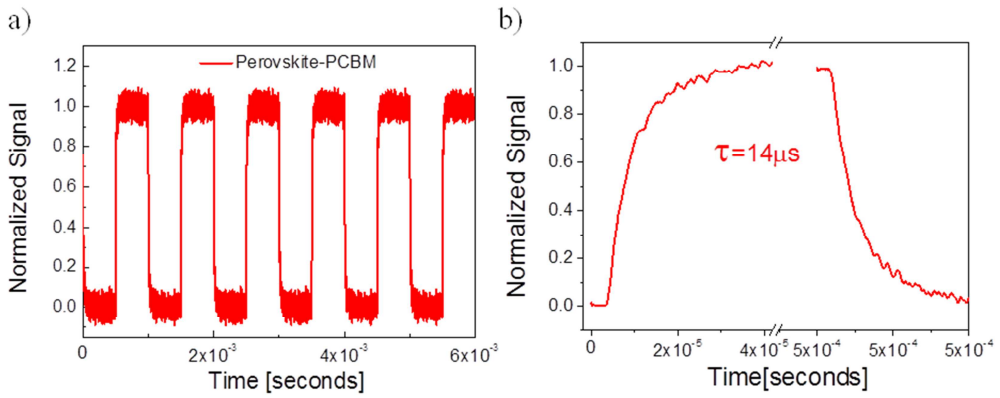

Figure 3.3.1: (a) Response of the perovskite-PCBM detector to a light pulse train (532 nm LED, 500 µs pulse width, 1 µW/cm^2 intensity) with 5V bias. (b) Transient response of the photodetector with equal rise and fall times of 14µs.

The obtained photoresponse time is more than one order of magnitude faster than in previously reported printed perovskite photodetectors (Table 3.1). This time response allows the detector to follow light signals with frequencies up to $f_{max} \approx$ 35 kHz.

Despite the higher gain, it is about 4 time faster with respect to a device which uses perovskite only (rise and fall time 55 µs, $f_{max} \approx$ 9 kHz, Figure 3.3.2b).

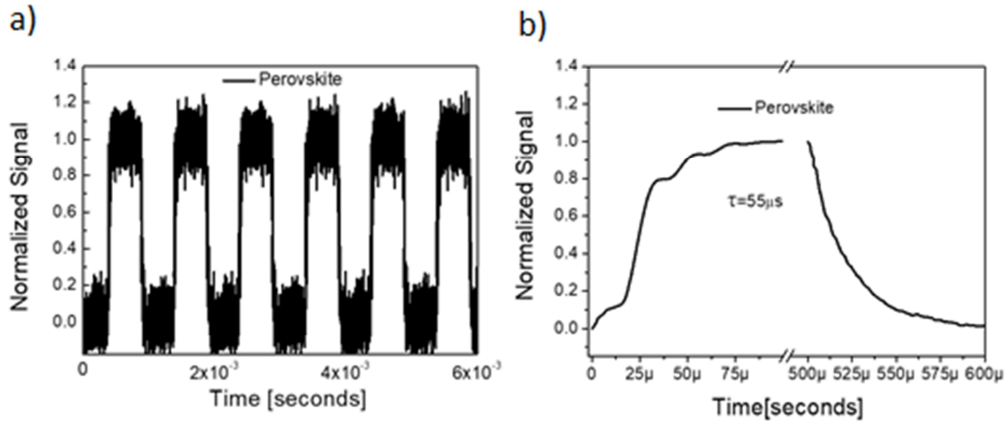

Figure 3.3.2: (a) Perovskite detector response to a light pulse train (532 nm LED, 500 µs pulse width, 1 µW/cm^2 intensity) with 5V bias and (b) Transient response of the photodetector with equal rise and fall times.

A decrease in transient response time with PCBM and a concomitant increase of the gain, support the picture of an improvement of the transport mechanism for holes

within the perovskite layer and an effective trapping of electrons in the acceptor PCBM layer.

The Gain–Bandwidth product of photodetector is calculated. This is a useful figure of merit to compare performances of detectors related with gain. We obtain values as high as 1.5×10^7 Hz at 10 μW/cm^2 for λ = 460 nm, which is a few orders of magnitude higher than previously reported printed perovskite photodetectors.

With respect to all perovskite photodetectors reported till date, our devices have one of the most optimized Gain-Bandwidth tradeoff (Figure 3.3.3).

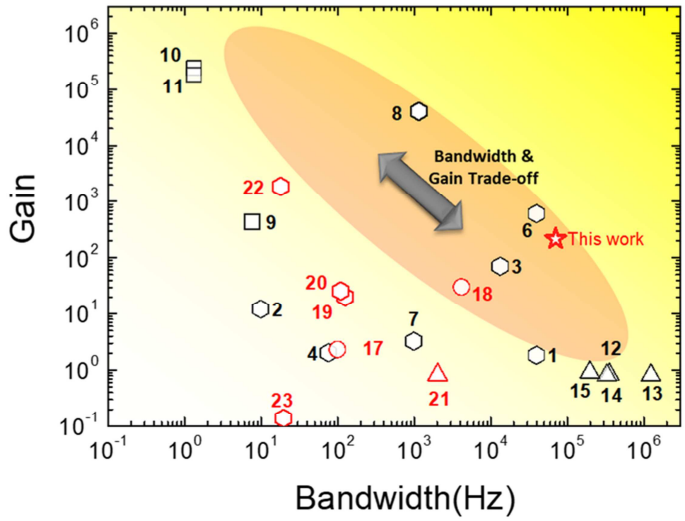

Figure 3.3.3: Gain Vs Bandwidth values plotted for photodetectors from the Table 3.1. A trade-off between the Gain Vs Bandwidth is clearly observed in the highlighted area. Our result is one of the best up to now.

3.4 NOISE CHARACTERIZATION AND SPECIFIC DETECTIVITY

Another figure of merit for a light detector is related to its sensitivity, namely the possibility of detecting small signals. The minimum signal for which an electrical response is discernable is ultimately limited by the intrinsic device noise. To quantify this aspect is used the Specific Detectivity (D^*) that takes into account also the active area (A) of the device, permitting a fair comparison between different light detector devices.

$$D^* = \frac{(A)^{0.5}}{NEP}\ [\mathrm{cmHz}^{0.5}/\mathrm{W}]\ .$$

D^* is defined as the ratio between the root square of the active area and the Noise Equivalent Power (NEP), namely the power of a sinusoidal monochromatic radiation producing the same root mean square output signal of the device current noise (i_n) in an ideal noise-less device and bandwidth (Δf):

$$NEP = \frac{(\overline{i_n^2})^{0.5}}{R(\Delta f^{0.5})}\,[\mathrm{W}]/[Hz^{0.5}]\ .$$

A first estimations of D^* can be obtained by assuming that the noise of the device is limited by the fluctuations of the dark current circulating in the device, called white shot noise. This approximation may lead to large overestimation of D^*, especially at low frequencies where $1/f$ noise, so called "flicker" noise can be significant and it dominates.

This scenario is even more critical for photoconductors, since traps can contribute to the flicker noise; pushing the corner frequency (f_c) between $1/f$ and the white shot noise, *i.e.* the frequency above which shot noise dominates D^*, to high frequency.

If the device can't operate at such high frequencies, the assumption that white noise dominates completely fails. Therefore, D^* has to be evaluated by performing accurate noise measurements. We have measured the equivalent current noise of printed perovskite detectors both with and without PCBM coating, over a large bandwidth (from 10 Hz to 150 kHz). In the investigated range, the noise of the printed detector without PCBM is completely dominated by flicker noise, reaching high level of noise over the whole bandwidth at which the detector can operate (Figure 3.4.1, black line).

At the maximum operative frequency of 9 kHz for the pristine perovskite device, $(\overline{i_n^2})^{0.5}$ is ~ 2.3 x 10^{-13} A/Hz$^{0.5}$ that is almost two orders of magnitude higher than the shot noise, corresponding to a NEP of 0.33 pW/Hz$^{0.5}$. Interestingly, when the PCBM coating is introduced, the flicker noise is reduced by two orders of magnitude, so the corner frequency (f_c) is retroceded within the investigated range, falling at 4 kHz (Figure 3.4.1, red line).

Since the perovskite-PCBM device can operated up to 35 kHz, there is a frequency window from f_c up to such maximum frequency where the noise in the device is limited purely by the shot noise. This results into a considerably lower $(\overline{i_n^2})^{0.5}$ of ~ 7.69 x 10^{-14} A/Hz$^{0.5}$, with a NEP of 0.97 fW/Hz$^{0.5}$, despite of the higher dark current observed in devices with PCBM.

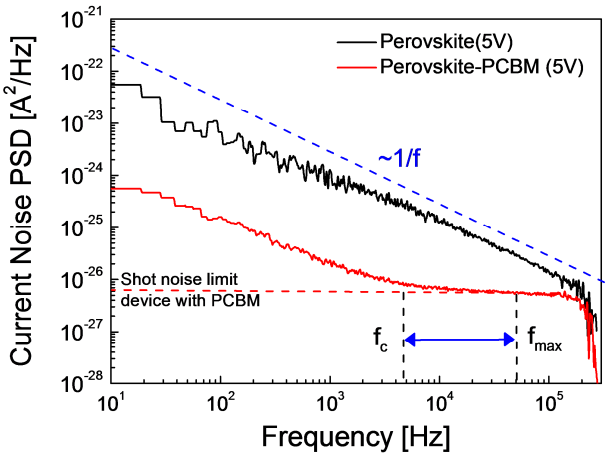

Figure 3.4.1: Current Noise Power Spectral Density (PSD) of the photoconductors with (red line) and without (black line) PCBM coating. Shot noise limit, corner frequency f_c, maximum operating frequency f_{max}, and frequency range where detectors are operated at shot noise limit is shown for devices with PCBM.

Considerable reduction of 1/f noise upon deposition of PCBM on perovskite crystals is an interesting evidence and confirms that the small fullerene-derivate molecules act as a trap passivator.

Moreover, we can suggest that PCBM acts on surface trap states of the crystals, which determines the higher flicker noise in the device without PCBM.[86] The device noise is compared where the flicker noise dominates (500 Hz), with the noise expected from the Hooge's empirical formula, used to rationalize the 1/f noise in terms of fluctuations in the electrical conductance of homogeneous samples (Figure 3.4.2).

$$\left(\overline{i_n^2}\right) = \alpha_H I^\gamma / (fN) \, .$$

where α_H is called Hooge's parameter, I is the dark current, N is the total number of carriers. In the case of bare perovskite device, the Hooge's formula hardly fits the data and $\gamma > 2$ is extracted on a limited range of currents and frequencies. If the value of γ exceeds 2 may suggest a complex source of noise.[87,88]

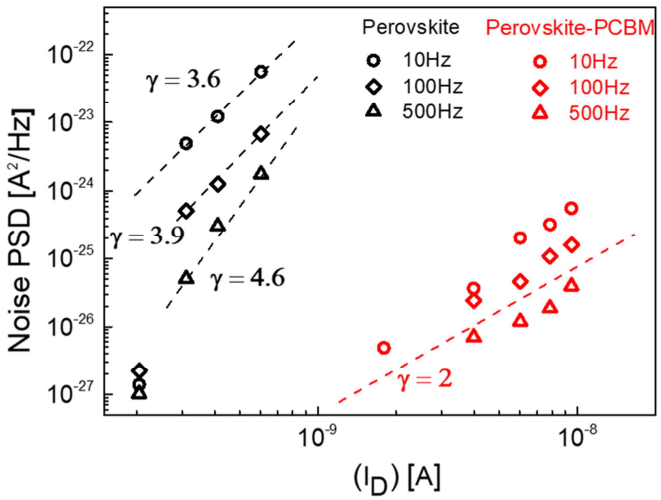

Figure 3.4.2: Values of γ for different frequencies for photodetectors with and without PCBM as a function of frequency.

When the PCBM coating is introduced the low frequency flicker noise correlates well with the Hooge's formula for homogeneous samples (γ = 2). Ions accumulation at grain boundaries in presence of an electric field have been frequently observed in $MAPbI_3$ thin films. This effect would be exacerbated in the case of the pristine perovskite film, where the connectivity between individual perovskite crystals is lower than in spin coated films. Large presence of accumulated I^- ions at the grain boundaries is expected to give rise to inhomogeneity in energy landscapes, contributing to an increased noise. The passivation of ions by the presence of PCBM molecules strongly reduces this source of noise, and renders $\gamma \sim 2$, as often verified in inorganic semiconductors.

After the noise measurement, the specific detectivity (D^*) can be extracted, which for the perovskite-PCBM detectors is very high in all the visible spectra, reaching a maximum of 7.23 x 10^{13} cmHz$^{0.5}$/W at λ = 460 nm (Figure 3.4.5).

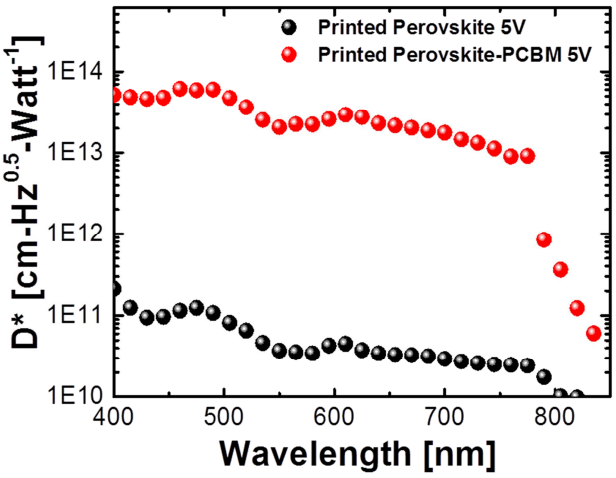

Figure 3.4.5: Specific Detectivity D* for perovskite-PCBM devices (red dots) and pristine Perovskite (black dots).

The printed perovskite particles device shows one of the highest measured specific detectivity for the reported perovskite detectors till date and is at least one order of magnitude higher than any printed perovskite photodetector (Table 3.1).
The very good overall performance of the printed detectors is a straight consequence of a combination of perovskite trap passivation by PCBM molecules. This reduces the transit time of the mobile carriers (holes) and the 1/*f* noise but in the meanwhile works as an electron acceptor ensuring a selective hole circulation that permits to achieve high gain in the device.

Thanks to the results achieved with this work, we think that the perovskite particles inks can open up attractive possibilities to use printable perovskite materials for large area photo-detection application. The fastest response and the highest gain-bandwidth product so far, validate our idea. Moreover, the specific detectivity values observed are higher than commercially available silicon photodiodes, which is remarkable considering our photoconductor is printed with a very simple geometry.

The characterization of the photodetector devices has been done in collaboration with Dr. Vijay Venugopalan.

3.5 STATE OF THE ART

In this section, the actual state of the art of photodetectors is resumed in a table (Table 1). Only light detectors measured using standard notation and with (almost) complete information are included for comparative purpose.

It is worth noting that the gain is a function of incident light intensity and the comparison of performances are carried out at similar light intensities whenever possible.

Bandwidth is calculated using the time taken for the change in signal (10% - 90%). G_{ext} is calculated from the responsivity given in the papers, using the standard form.

Material	Responsivity [A/W]	Gain [a.u.]	Length normalized Response time [µs/µm] **	Detectivity $\times 10^{10}$ [Jones] *	Light Intensity [µW/mm^2]	Ref N°
$CsPbI_3$ 2D Sheets	0.64	1.8	1.25	Not Measured	1	89
$MAPbI_3$ Spin Coated	2	12	7×10^3	Not Measured	0.1	90
$MAPbI_3$ Single Cyrstal	30	70	3.8	Not Measured	0.1	91
CNT-$MAPbI_3$	0.7	2	7	Not Measured	0.1	92
Crystalline Nanowire $MAPbI_3$	0.5	1.17	Not Measured	2×10^3	0.1	93
$MAPbI_3$ Crystals	220	600	5	3×10^3 *	0.4	94
$MAPbCl_3$ Crystal-UV	1	3.2	500	100	0.1	95
$MAPbI_3$ Single Thin Crystal	10^4	4×10^4	2345	1.3×10^3 *	0.1	96
$MAPbI_3$-Graphene Transistor	180	431	2×10^3	0.1	1	97
$MAPbI_3$-MoS_2 Transistor	~10^5	2.4×10^5	2×10^4	~50	0.1	98
Hybrid $MAPbI_3$-Graphene Transistor	6×10^4	1.8×10^5	7.5×10^4	Not Measured	0.01	99
$MAPbI_3$ High Gain Buffer Layer	0.4	0.82	11.2	100	1	100
Spin Coated $MAPbI_3$ with PFN	0.32	0.8	2.6	4×10^4	0.1	101
Spin Coated PCBM Buffer	0.41	0.8	15	300	0.1	102
Spin Coated $MAPbI_3$ C_{60}	0.22	0.9	< 5	740	0.1	103
R2R/Gravure $MAPbI_3$	*5.2×10^{-3}*	*Not Measured*	*Not Measured*	*Not Measured*	*360*	*104*
Inkjet Printed $MAPbI_3$	*1.2*	*2.3*	*333*	*240**	*1*	*105*
Blade Coated $MAPbI_3$	*13.5*	*30*	*9.6*	*524*	*5*	*106*
Blade Coated-Hot Cast	*8.95*	*20.9*	*17000*	*290**	*37*	*107*
Blade Coating-Mixed Cation	*10.75*	*25*	*9×10^3*	*Not Measured*	*Not Measured*	*108*
Bar Coated Particles	*78.7*	*213*	*2.8*	*7.23×10^3*	*0.1*	*This*

						Work
Nanocrystals/Quantum Dots	*1500*	*1860*	*Not Measured*	2.5×10^{3}	*0.05*	[109]
2D Materials /Oxides	2.1×10^{-3}	*0.1*	6.4×10^{4}	*95.9*	*42*	[110]

Table 3.1: *corsive*: Printed photodetectors Others: Non-Printed detectors. (*) Indicates theoretically calculated *D** which has shown to be a large overestimation for perovskites or indicates that specific detectivity *D** is calculated from theoretical noise and the noise is not measured. Using theoretical values for noise has shown highly overestimation of *D** for Perovskite PDs by at least an order of magnitude or more and is shown not to be consistent. (**) Lifetimes : Only lifetimes calculated on transient signals where the transient response was allowed to reach saturation is shown here. Impulse measurements are not considered. Length normalized temporal response is shown for different devices where for photodiodes the film thickness is taken as the length.

Chapter 4

Printed CsPbBr3 Nanocrystals Inks for Light Harvesting Applications

In the 4th chapter of the Ph.D. thesis, the project on nanocrystals based, wide band gap solar cell devices is described. Here is possible to find the details of the active material's synthesis and how we optimized it looking at the concentration of precursors and polarity of the solvents used; these parameters influence the size and the packing of the nanocrystals that strictly correlated to the performances of the device. As main result, we were able to obtain standard structure nanocrystals-based fully inorganic perovskite solar cells with 1 cm^2 active area deposited by large-area-compatible deposition technique.

Hybrid perovskites are attractive materials thanks to their extraordinary electrical [111,112,113] and tunable optical properties from NIR [114] to UV [115] that have been studied intensively in the fields of photovoltaic [116,117,118] where the power conversion efficiency is approaching the one of crystalline silicon solar cells [119]. After solar cells, also LED [120,121,122], photodetector [123,124,125], lasing [126,127,128] and field effect transistors [129,130] perovskite-based have been intensively investigated. Even if significant progress has been made in perovskite-based optoelectronic devices over the past years, still the open questions around this

material like lack of stability and up-scaling are limiting the real entrance of this technology in the industrialization. Other important parameters to obtain a good performing perovskite thin film solar cells fabrication are the film morphology[131] and the type and concentration of defects.

Recently, was shown that by using fully inorganic perovskite materials, the thermal stability is increased [132,133] and by using nanocrystals [134,135], the parameters that are driving the film morphology are reduced and the optical properties are enhanced.

Another possible application for nanocrystal inks perovskite-based might be the possibility of use them in tandem solar cell applications, where having materials with a tunable band gap is fundamental. By using inks is allowed to have different materials, able to absorb different wavelengths, obtaining devices with higher power conversion efficiency.

From the ink point of view, has been recently shown the possibility to up-scale the synthesis by synthetizing large quantity of nanocrystals dispersed in different kind of solvents and were realized solar cell devices with a layer by layer spin coating technique. What was not showed yet is the possibility to up-scale the active area of the devices. Here we focus the attention on having a wider active area in the devices and solving the related problems during an up-scaling process.

4.1 CESIUM LEAD TRI-BROMIDE NANOCRYSTALS SYNTHESIS

The room temperature nanocrystals synthesis is deeply explained in [136]. Briefly, to obtain cesium lead tri-bromide ($CsPbBr_3$) nanocrystals ink, 2 M of cesium carbonate (Cs_2CO_3) is dissolved in propionic acid (PrAc) and 5 µL are injected in 3 mL of a poor solvent Hexane (Hex) and Propan-2-ol (IPA), mixed in a ratio 2:1. 100 µL of 0.5 M lead (II) bromide ($PbBr_2$), solubilized in a mixture of IPA, PrAc and Butylamine (ratio 1:1:1) is added after the first injection under vigorous stirring at room temperature.

The solution turns immediately green and the nanocrystals are formed within 10 seconds. After the formation of the nanocrystals, they are centrifuged at 1000 rpm

for 2 minutes by using a centrifuge, to remove the unreacted products and washed twice with Toluene. During the synthesis of different batches, was observed that apparently same conditions have led to different nanocrystals produced.

4.2 $CsPbBr_3$ NANOCRYSTALS CHARACTERIZATION

The absorption and steady state photoluminescence are showed in Figure 4.2.1a. Both are measured from thin films deposed on glass by spin coating at 1000 r.p.m. In the graph is possible to individuate as product of the reaction only the presence of three dimensional (3D) nanocrystals of $CsPbBr_3$ with the band edge at 515±5 nm and a photoluminescence at 521±5 nm. There is not the presence of any sub-products of the reaction but apparently similar synthesis conditions have led also to the absorption and photoluminescence presented in the Figure 4.2.1b in which is possible to distinguish some sub-products from the different shapes in the absorbance spectra.

In particular, it is possible to individuate the three dimensional nanocrystals, the multiphase perovskite and an excitonic peak in the blue region due to the presence of two dimensional nanoplatelets at 515±5 nm, 464±5 nm and 436±5 nm, respectively. To each absorption is related a peak in photoluminescence spectra.

By X-Ray Diffraction analysis, showed in Figure 4.2.1c, green color line, is possible to distinguish the usual peaks for 3D $CsPbBr_3$ nanocrystals at two theta equal to 15.2°, 21.6° and 38.3°, that correspond to (100), (110) and (211) planes, respectively. The red color line in the same graph permits to recognize a mixture of multiphase, two and three dimensional perovskite nanocrystals thanks to the presence of all the previous peaks and the presence of extra peaks at low angles (two theta lower than 15°) distinctive for low dimensional and two dimensional nanoplatelets.

Nevertheless, the presence of three dimensional only and the mixture of two and three dimensional perovskite nanocrystals is further confirmed by High Resolution – Scanning Electron Microscopy (HR–SEM) in Figure 4.2.1d and Figure 4.2.1e, where is possible to clearly distinguish nanoplatelets from three dimensional nanocrystals thanks to the different shape.

Our speculation on the formation of different products is that the amount of Cs^+ in the reaction might be not sufficient. Since the solution is viscose, a different quantity in the reaction might be injected from batch to batch of synthesis. Smaller amount of Cs^+ drives the reaction to the formation of two dimensional perovskite with Butylammonium as cation A in the crystal structure.

Our hypothesis come from the fact that is now well established that aliphatic ammonium (RNH_3^+) ions can compete with the Cs^+ in the reaction for the formation of perovskite materials. [137]

Anyway, the hypothesis has to be confirmed yet and further experiments have to be carried out to confirm unambiguously our idea.

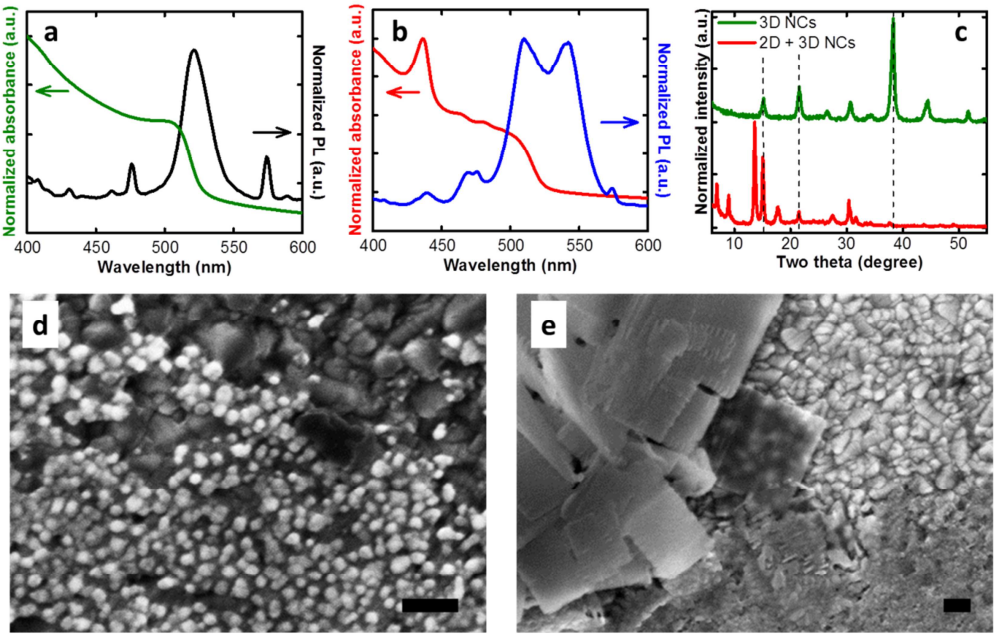

Figure 4.2.1: Absorbance and photoluminescence of two different synthetized batches of $CsPbBr_3$ nanocrystals deposed on a glass substrate. (a) 3D only nanocrystals, (b) mixture of multiphase, 2D and 3D nanocrystals. (c) XRD spectra of 3D only nanocrystals (green line) and the mixture of sub-products (red line). HR–SEM images showing the (d) absence and (e) presence of 2D nanoplatelets components. Scale bar 200 nm.

After a first characterization of the nanocrystals, also the relative photoluminescence versus the fluence is analyzed because high rates of radiative recombination of carriers are essential for efficient device operation. The radiative recombination competes with the trapping of the carriers at crystal defects. The

trap-limited recombination is usually investigated by monitoring the photoluminescence quantum yield. [138] This means that high PLQY values, are correlated with low defect concentration.

All the nanocrystals were deposited through spin coating and were deposited three layers one on top of the other. During the PLQY measurement, done by Jetsabel Maria Figueroa Tapia, the samples are kept in vacuum atmosphere. This measurement permits to understand if the exposure to light induces photo-instability of the material. It is generally accepted that at low excitation densities, the carrier recombination is dominated by monomolecular process through trapping while by increasing the excitation density, when the trap states are filled, bimolecular band to band recombination became the dominant process. Another important information is given by the hysteretic behavior of the curve when the samples are measured from low to high fluences and back to low, always on the same spot. If the defects are well passivated, the points are overlapped, while if the ions are free to move around the material, the aperture of the curve increases. This aperture suggests that under photo-excitation there is an increase in the density of traps.

The PLQY values obtained for different synthetized batches are correlated to the absorbance spectra showed in the inset of Figure 4.2.2.

In the graph, is clearly distinguishable the different behavior for the various kind of samples. The 3D nanocrystals (green color light) do not present hysteretic behavior by increasing and decreasing the fluence. This means that the surface of the nanocrystals is well-passivated by the amino-ligands used and the photo-excitation do not causes a variation in the density of the traps in the nanocrystals.

If during the synthesis, after the two injections, the solution is left stirring for one minute instead of 10 seconds (black color line), the size of the 3D nanocrystals increases. The consequence for bigger size synthetized nanocrystals is that it's possible to distinguish an excitonic peak in the absorbance spectra, around the band edge. These kind of samples present an huge hysteretic behavior in PLQY measurements and it is probably due to the fact that the amino-ligands do not well-passivate the surfaces of the nanocrystals and a certain degree of photo-instability is detected.

If the reaction brings to the formation of mixture of multiphase, 2D and 3D nanocrystals (red color line), clearly distinguishable from the absorption spectra, the hysteretic behavior is still present but less pronounced than the previous case.

What is clear after the PLQY measurements is that the reaction brings not only different shapes of nanocrystals but also we need to monitor the value of the size and how well the surfaces are passivated by the amino-ligands. All these parameters are correlated to the performances of the solar cell devices.

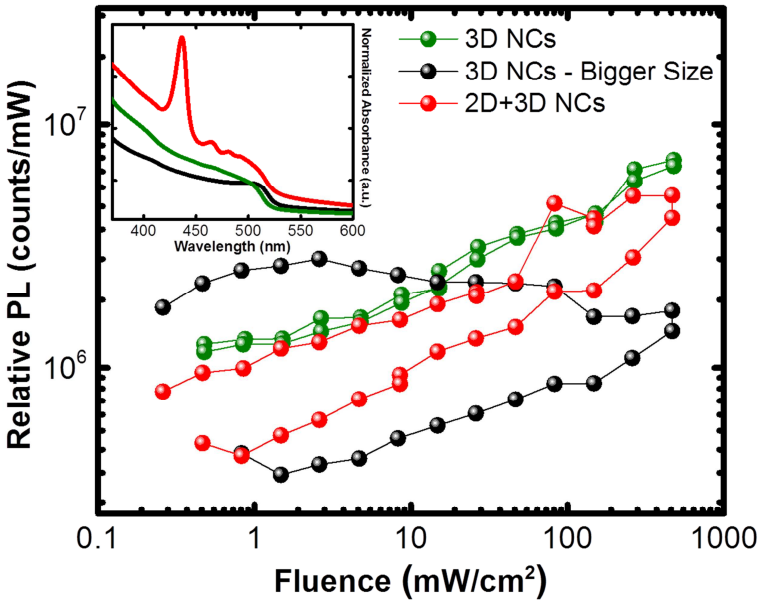

Figure 4.2.2: Relative photoluminescence versus fluence for nanocrystals synthetized in different batches and deposed on glass substrates by spin-coating. Absorbance spectra in the top-left inset.

4.3 INKS OPTIMIZATION

The first step to control the optimization of the perovskite active layer upon inks deposition is the optimization of the nanocrystals packing. This comes with the control of the size and shape of the crystals and the solvent used to disperse them before the printing process. The part of inks optimisation has been done in collaboration with Dr. Marina Gandini.

4.3.1 CONCENTRATION DEPENDANCE

One way to control the size and the shape of the nanocrystals is by modifying the concentration of the precursors in the starting solution. [139] Here we did a systematic concentration variation of $PbBr_2$ dissolved in the mixture of IPA, PrAc and Butylamine. Starting from 0.50 M, we decreased the concentration until 0.20 M. In Figure 4.3.1a is showed the (100) diffraction peak obtained by X-Ray diffraction analysis after the deposition of the material on bare glass. Analyzing the data is possible to see that by reducing the $PbBr_2$ concentration, the broadening of the peak decreases. By using the Scherrer Equation:

$$\tau = \frac{K\,\lambda}{\beta \cos\vartheta}\ .$$

that correlates the broadening of the peak at full width half maximum (β) to the main domain size of the crystals (τ).

τ is proportional to a constant called shape factor (K) close to unity and x-ray wavelength used (λ) and there is an inverse correlation with the Bragg angle (ϑ).

By using this formula, is possible to calculate the crystal main domain size. In Table 4.1 we report the mean domine size as a function of the $PbBr_2$ precursor concentration, after analyzing the main XRD peak at 15.2°.

If the concentration of precursor is decreased, the mean domain grows. In Figure 4.3.1b, the onset of the absorption spectrum, in agreement, shows a more defined excitonic transition when the crystal size increases. [140]

The J-V characteristic for a solar cell device under a solar simulator at 1 sun is shown in Figure 4.3.1c.

The active layer of the devices is obtained from a thin film made with different nanocrystal sizes but the active area for each pixel is constant with a value of 0.0935 cm^2.

As the size increases, the current density grows as well, till an optimum crystal size of 28.26 nm that corresponds to a concentration of $PbBr_2$ equal to 0.36 M.

If the nanocrystals size become bigger than 50 nm the thin film becomes insulating and no charges can be extracted from the device anymore. This behavior is probably due to a bad packing of nanocrystals during the film deposition.

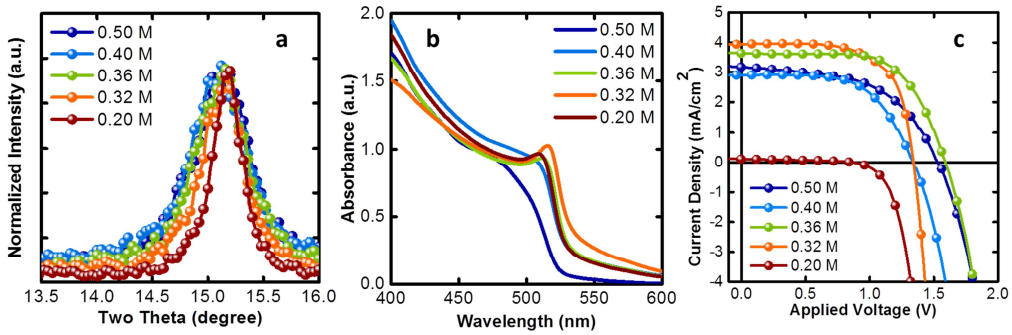

Figure 4.3.1: $PbBr_2$ concentration dependence analysis (a) XRD normalized peak for (100) plane used to calculate the mean domine size with Scherrer equation, (b) absorbance spectra and (c) J-V characteristics of thin film solar cells under 1 sun.

$PbBr_2$ concentration (M)	Mean Domain Size (nm)	Jsc (mA/cm^2)	Voc (V)	FF (%)	PCE (%)
0.50	18.32	3.17	1.53	53.2	2.59
0.40	23.66	2.90	1.34	60.1	2.37
0.36	28.26	3.63	1.60	64.3	3.73
0.32	38.55	3.94	1.34	66.2	3.56
0.20	60.40	0.13	0.88	39.6	0.04

Table 4.1. Correlation between $PbBr_2$ concentration, mean domain size and solar cells performances (Jsc – short circuit current, Voc – open circuit voltage, FF – fill factor and PCE – power conversion efficiency).

4.3.2 SOLVENT DEPENDANCE

After being fixed the optimum $PbBr_2$ concentration in the starting solution at 0.36 M, the nature of the solvents is now investigated. In particular the polarity of the dispersant solvent or rather the solvent in which the nanocrystals are dispersed at the final step, before the deposition.

The polarity is an important parameter to check to deeply control how well (or bad) the nanocrystals are packed once deposed on the substrate. The polarity of the dispersant controls also the degree of the aggregation of the particles in the inks. It can be monitored by the time needed from the particles to sediment at the bottom of the vial. The possibility to avoid the pre-aggregation of the particles in the inks represents a big advantage during the deposition of the nanocrystals because it allows a controllable thickness and homogenous films. For these reasons, a systematic study on dispersing solvents is done and is resumed in Table 4.2.

The effect of the polarity on the nanocrystals' pre-aggregation is reflected to differences in XRD spectra, absorption onset and also solar cells performances with the results that are shown in Figure 4.3.2.

Toluene-dispersed nanocrystals are the most stable in solution over time and they present the smallest size (~ 18.32±0.39 nm) extracted by Sheerer Equation.

If the polarity of the dispersant solvent is increased, i.e. the chlorobenzene-dispersed nanocrystals, they tend to sediment slightly faster and the resulting size is ~ 19.32±0.43 nm.

Finally, if the polarity is further increased (i.e. propan-2-ol) the size reaches much higher values ~ 41.04±1.94 nm. The (100) plane reflections obtained by XRD analysis for the nanocrystals coming from different dispersants are shown in Figure 4.3.2a.

The absorption onset is pretty much stable; the only difference is for propan-2-ol-dispersed nanocrystals (light-blue color line) where is visible an excitonic peak, confirming that the size of the nanocrystals is bigger than the nanocrystals dispersed in the other two solvents, Figure 4.3.2b.

Regarding the J-V characteristic under 1 sun for thin film solar cells, the behavior is much different for solvents with higher polarity than Toluene: both Jsc and Voc are reduced and the overall PCE % is lower than Toluene-dispersed nanocrystals

Figure 4.3.2c. All the active areas of these devices is 0.0935 cm^2 and the nanocrystals were deposed by spin-coating.

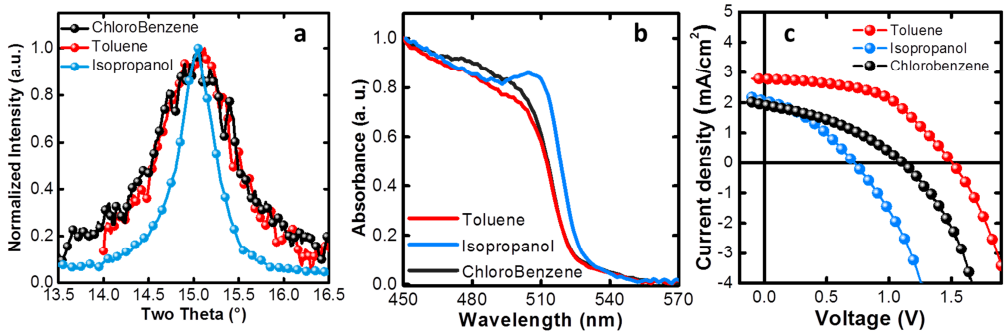

Figure 4.3.2: Nanocrystals dispersed in different solvents. (a) XRD normalized (100) peak at 15.2° used to calculate the average of domine size with Scherrer equation, (b) absorption onset and (c) J-V characteristics of solar cells under 1 sun.

Dispersant solvent	Jsc (mA/cm^2)	Voc (V)	FF (%)	PCE (%)
Toluene	2.78	1.51	51.1	2.15
Chlorobenzene	1.92	1.12	42.5	0.92
Propan-2-ol	2.06	0.72	35.5	0.53

Table 4.2: Correlation between different dispersant solvents and performances of the solar cell devices.

4.4 DEVICES REALIZATION AND CHARACTERIZATION

After the fine tuning of the synthesis and a deep characterization of the material produced, standard structure solar cells are made. The deposition technique used is the bar coating. The bar coating technique consists in a grooved metal bar that roll on top of the substrate, spreading the ink. It is usually used for polymeric materials but it is also a well performing technique with inks made by nanocrystals that are dispersed in solvents. The thickness of the deposed film, can be tuned by modifying different parameters, such as viscosity of the ink, concentration of nanocrystals in the solvent, speed of the bar, roughness of the substrate and pitch of the grooves on the metal bar. [141]

The bar coating, in contrast with the spin coating technique, is a roll-to-roll compatible technique, permitting the scale-up the devices. The use of this technique permitted us to increase the active area and we were able to achieve $1cm^2$ active area in solar cell devices.

Since the solvent is one of the key point during the printing processes, both the boiling point and the polarity must be considered and a trade-off between nanocrystals size and boiling point of the dispersant solvents must be reached.

To have performing devices, after analyzing Toluene, Chlorobenzene and Propan-2-ol as dispersant for nanocrystals, mixtures of two solvents are studied. The optimum for our inks is found with a mixture of two solvents: IPA and Toluene with a ratio 2:1.
The IPA, an alcohol, permits to have a lower boiling point and to fasten the drying process between two consecutive bar coated layers with respect to Toluene only but having a polarity higher than bare Toluene encourages the growth of mean domain size. Toluene, instead, is able to avoid the pre-aggregation of nanocrystals, permitting a longer time for sedimentation and increases the boiling point, driving the drying process of the ink on the samples more uniformly. The difference in drying process, is explained by SEM images in Figure 4.4.1.

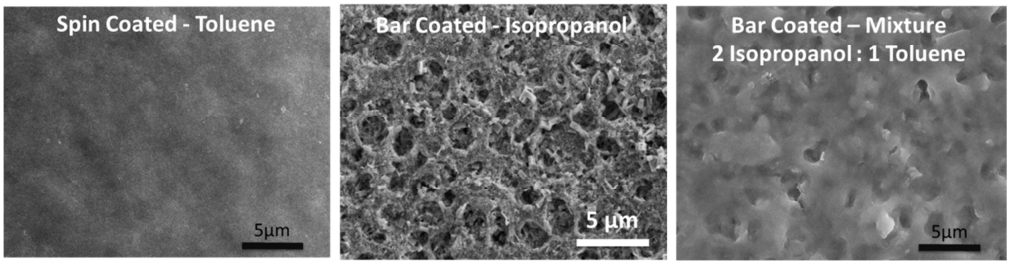

Figure 4.4.1. Scanning Electron Microscopy top view images of nanocrystals deposited from different solvents and with different deposition techniques. Toluene-dispersed, spin coated nanocrystals ink (left side image), IPA-dispersed, bar coated nanocrystals ink (center image) and nanocrystals ink deposed by bar coating from a mixture of Isopropanol and Toluene with a 2:1 ratio (right side image).

In Figure 4.4.2a, are showed the XRD main peak for the nanocrystals deposed on glass by spin coating. By calculating the main domain size of crystals with Scherrer Equation, analyzing the (100) peak, a value of 33.99±1.34 nm is found. The main domain size values for different dispersant solvents are resumed in Table 4.3.
Thanks to this mixture of two solvents, the inks become easily printable on top of different kind of substrates (i.e. glass, ITO, FTO, PET,…).
After an optimization of the deposition speed and metal groove, was possible to obtain good morphology and good smoothness of the active layer in the solar cell devices by bar coating technique Figure 4.4.2b.

Solvent	Relative polarity	Mean Domain Size (nm)
Toluene	0.099	18.32 ± 0.39
Chlorobenzene	0.188	23.66 ± 0.43
Isopropanol	0.546	28.26 ± 1.34
2 Isopropanol : 1 Toluene	0.393	33.99 ± 1.94

Table 4.3. Correlation between relative polarity for different solvents and mean domain size, calculated with Scherrer Equation.

The solar cell device is fabricated in standard structure. It consists in a sequence of FTO/compact TiO_2/Active Layer/Spiro OMeTAD/Au showed in the cross section in Figure 4.4.2c. The lower part collects the electrons and the upper part collects the holes photo-generated in the active layer of the device.
The FTO-coated glass substrates are etched with zinc powder and hydrochloric acid (2 M) to obtain the required electrode pattern. The substrates are cleaned in a ultra-sonication bath, in sequence with detergent (Hellmanex, 2% v/v in water), distilled water, IPA, Acetone and IPA for 10 minutes each step.
The substrates are then dried with N_2 gun and treated with oxygen plasma for 10 minutes to remove the organic traces that might stay on top of the substrate.
As electron transporting layer (ETL), a compact TiO_2 is used. A precursor solution is prepared by mixing 6 µL of 2 M hydrochloric acid in 1 mL of IPA to a titanium iso-propoxide solution in IPA. The solution is spin-casted at 2000 r.p.m. for 60 s

and subsequently sintered at 500°C for 45 min. Once the substrates are back at room temperature, the active layer is deposed.

- For spin coated solar cells, the synthetized $CsPbBr_3$ nanocrystals dispersed in Toluene can be deposited in ambient atmosphere, at 2000 rpm, 2000 r.p.m./s for 45 s with no further annealing. Different layers are deposed in sequence, increasing the thickness of the active layer. A check is done after each deposited layer with an absorption spectra by a UV/Visible spectrophotometer and the thickness is measured by profilometer. The optimized number of layers is eight.
- To bar coat the inks, 100 µL of solution are deposed on the ETL and an automized bar spreads the ink with a speed set at 30 mm/s with a grooved bar of 10 µm. Even for bar coating technique, multi-layers deposition is needed. For this technique, the optimized number of layers in the device is five.

After the deposition of the active layer, the samples are transferred into a N_2-filled glove box for the deposition of the hole transporting layer (HTL). The Spiro-OMeTAD molecule is spin coated at 1500 r.p.m., 1500 r.p.m./s for 40 s.

The solution is prepared by dissolving 75 mg of Spiro-OMeTAD, 32 µL 4-tert-butylpyridine, 18.8 µL of a stock solution of 520 mg/mL Li-TFSI salts in acetonitrile in 1 mL of anhydrous chlorobenzene.

The hole transporting layer has to be oxidized in dry air to increase the conductivity of the small molecules and, after 12 hours of exposure to dry air, a 75 nm thick gold film is thermally evaporated through a shadow mask.

The active area of the devices is 0.0935 cm^2 or 1 cm^2, depending on the experiment.

4.4.1 OUTDOOR PERFORMANCES

These solar cell devices are tested under a solar simulator at 1 sun intensity, both in forward-bias to short circuit (FB-SC) and short circuit to forward bias (SC-FB), also called reverse scan. The data reported refers to a scan rate equal to 0.01 V/s, without any pre-bias of the sample and 10 s of light soaking. In all the J-V characteristics shown, no hysteretic behavior is found.

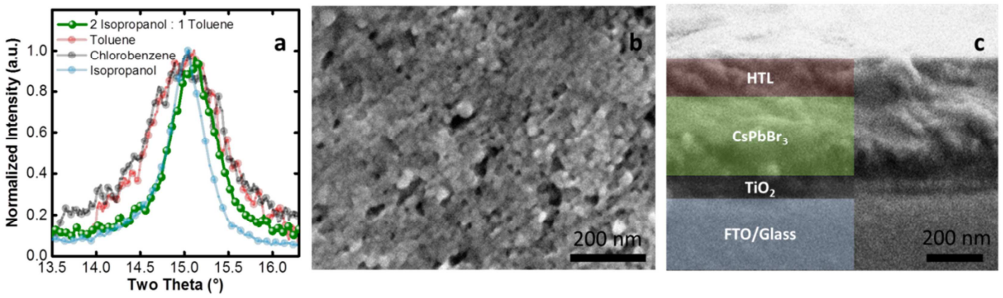

Figure 4.4.2: Nanocrystals dispersed in the mixture of Isopropanol and Toluene with 2:1 ratio. (a) comparison between different XRD normalized (100) peaks. The nanocrystals are deposited on glass by spin coating starting from different solvents, (b) top view morphology by HR-SEM of the bar coated active layer starting from the mixture of two solvents (Propan-2-ol and Toluene) and (c) cross section image of the full device by HR-SEM with highlighted the different layers (Glass/FTO/c-TiO_2/$CsPbBr_3$/Spiro-OMeTAD).

The J-V characteristics are shown in Figure 4.4.3a. The highest performances are reached by printing five layers. Between two consecutive layers a waiting time of 2 minutes is needed to permit the drying process of the solvent printed. The optimal speed bar is found to be 30 mm/s with a groove path of 10 µm.

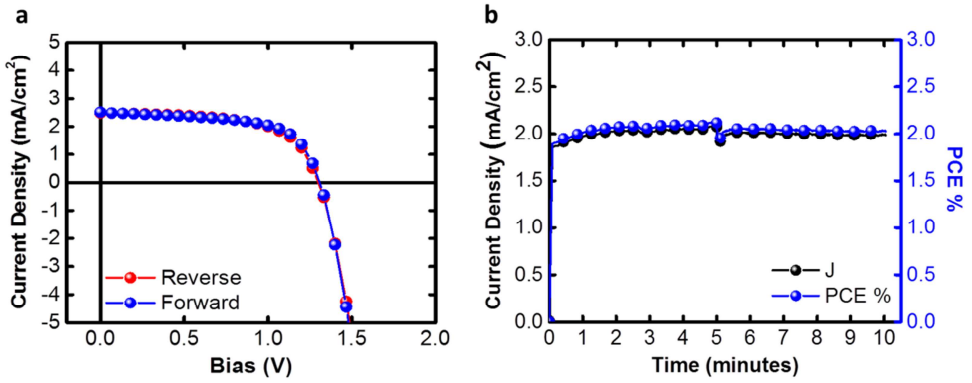

Figure 4.4.3. a) J vs. V curve forward (blue line) and reverse (red line) at slow (0.01 V/s) scan under 1 sun. No hysteretical behavior was found. b) Current density (J) vs. time (t), black line and Power Conversion Efficiency (PCE %) vs. time (t) (blue line) biasing the device (at maximum power point value equal to 1 V).

The solar cells were tested under 1 sun with a scan rate of 0.01 V/s. No hysteretic behavior was found; in fact, the forward and reverse scan are exactly overlapped. The obtained performances, resumed in Table 4.4, are the following:

- J_{sc} = 2.48 mA/cm^2
- V_{oc} = 1.31 V
- $FF_{\%}$ = 63%
- $PCE_{\%}$ = 2.11%

Importantly, we monitored the device performances by tracking the maximum power point (M.P.P. ~ 1 V) in air, with 65% humidity, without any kind of encapsulation obtaining a stable device over 10 minutes as a confirmation to the fact that the fully inorganic perovskite is a stable material under thermic stress and high moisture level. The behavior is shown in Figure 4.4.3b.

4.4.2 INDOOR PERFORMANCES

In the last few years, an exponential interest for indoor light harvesting applications is conquering the PV market. It can be used to power on different kind of devices like Internet of Thing (IoT) and low-consuming devices in our houses. [142]
The idea in behind is that is possible to exploit the indoor illumination and the light coming from outside (i.e. the sunlight passing through the windows).

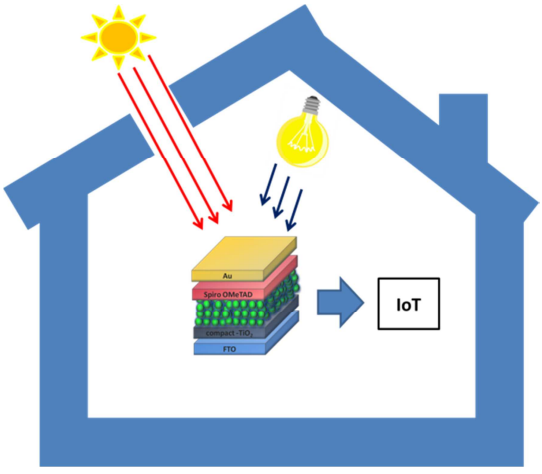

Figure 4.4.4. Sketch for indoor and outdoor light harvesting. Both the sources of light can generate enough efficiency to power on the low-consuming devices and the Internet of Things.

With this application in mind, the same devices are tested under white LED board with an intensity of 1000 Lux with the same scan rate to compare the solar cell performances. The intensity used is 1% of 1 sun and it is a value that is easily reachable by combining indoor and outdoor illumination.

The devices gave higher performances at low incident light intensities. The obtained values for the champion device are:

- J_{sc} = 47.12 μA/cm^2
- V_{oc} = 0.93 V
- $FF_{\%}$ = 52%
- $PCE_{\%}$ = 3.50%

From Figure 4.4.5 is possible to see that all the tested devices, responded with similar behavior and similar J vs V characteristic obtaining a yield of 100%.

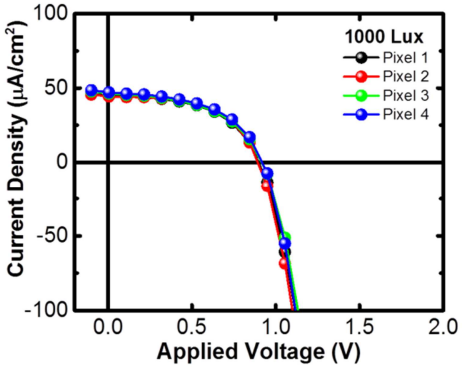

Figure 4.4.5: Current density (J) vs. applied voltage (V) curves. In the graph is showed the forward curve at slow (0.01 V/s) scan under 1000 Lux coming from a white LED board for all the devices that are tested.

In Table 4.4 are compared the performances of the best device under the solar simulator at 1 sun and under the white LED board set at 1000 Lux.

Illumination used	Jsc (mA/cm^2)	Voc (V)	FF (%)	PCE (%)
1 sun	2.48	1.31	63.1	2.11
1000 Lux	47.12 x 10^{-3}	0.93	52.5	3.50

Table 4.4. Performances of the best solar cell device under different illumination intensities.

Chapter 5

Highly Luminescent Nanocrystals Inks for Light Emitting Diodes

In the 5th chapter of the Ph.D. thesis, the project on highly luminescent MAPbBr$_3$ nanocrystals is described. Here is possible to find the details of the active material's synthesis, the characterization of the material and the amazing optical properties such as the extremely high Photoluminescence Quantum Yield (PLQY), both in solution and thin film, the extremely long carrier life time of the photo-generated carriers and the high stability of the material exposed to environmental conditions.

In this chapter, the focus is on synthesis of perovskite nanoparticles (NPs) also called nanocrystals (NCs). The nanoparticles permit to achieve color tunability and high PLQYs and even small changes in the synthesis protocol (such as temperature, stirring time, concentration of precursors…) can influence the size and the energy gap of the nanocrystals produced. By changing the energy gap and the size of the nanoparticles the photo-physical properties extremely change.[143,144]

The application of nanocrystals is mainly for innovative displays. In this field scientists are continuously looking for color tunable and narrow band emissive

materials. These characteristic permit to enhance the color performance of lighting and display systems.

Nowadays the quantum dots is playing an important role in this technological field but also perovskite nanocrystals have attracted attention thanks to the easily band gap tunability by halide exchange reaction and the narrow PL emission (FWHM ~ 20 nm). The presence of sub-band defect states is detrimental and was showed that high PLQY values and bright electroluminescence (EL) can be achieved only if the material is excited at high excitation fluencies (for PL) and high current density (for EL). A high fluence and/or a high current density cause a fast degradation of the material. This has been an obstacle for perovskite-based devices in this field.[145,146]

To overcome these problems, has been shown that the PL in hybrid organic-inorganic lead compounds can be enhanced by controlling the size and by a proper passivation of the defects on the surface of the nanocrystals. [147,148]

Considering the effect of the size, thermodynamically, the number of the intrinsic defects should decrease by decreasing the volume of the crystal considered and it might be further decreased because of the auto-excluding effect.[149] Even if the number of defects in bulk decreases, due to large surface to volume ratio, the number of surface defects are dominant in nanomaterials. Considering the increased exciton binding energy in small crystals, the PL emission is more likely due to exciton-recombination rather than the recombination from free charges [150] and if the defects on the surface are well-passivated, it will be possible to obtain highly luminescent nanocrystals with impressive PLQY at low excitation density. The high PLQY at low fluencies and an high EL at low current densities is desirable for Light Emitting Diode (LED) applications.

During the past years different path were followed for the synthesis of perovskite-based nanocrystals, such as the non-template synthesis of colloidal methylammonium lead bromide ($MAPbBr_3$) nanoparticles, with a size of around 6 nm showing a photoluminescence quantum yield (PLQY) of up to 83%,[151] or the ligand-assisted re-precipitation strategy (LARP) for the synthesis of hybrid organic-inorganic lead based perovskites with a particle size of around 3.3 nm and photoluminescence quantum yield (PLQY) between 50% and 93%.[152,153,154]

The goal of improving in luminescence stability and enhancing the PL efficiency of nanocrystals can be achieved by following another path. The idea is to grow a shell of a wider band gap semiconductor on top of the narrower band gap one.[155,156]
This structure of the nanoparticles, known as core–shell semiconducting nanocrystals, permits to engineer the optical properties of the semiconductor. The presence of the shell, improves the quantum yield by confining the charge carriers and it also passivates defects of the surface and non-radiative recombination sites that are present on the surfaces of the perovskite nanocrystals.

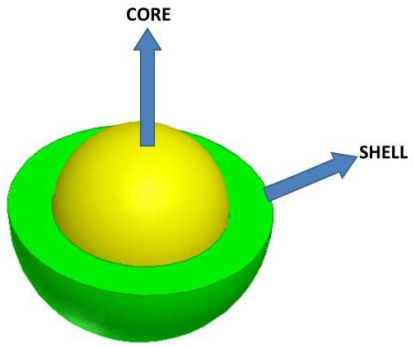

Figure 5.1: Cartoon for core-shell nanocrystal. The passivation on the surface inhibits the non-radiative recombination pushing up the PLQY.

Here a deep characterization of optical properties is done on core-shell perovskite nanocrystals synthetized by a modified-LARP technique. After the synthesis, the material is characterized both in solution and thin film. To obtain the thin film, the nanocrystals are deposited by spray coating.
This material presents incredibly high PLQY and a stability in environment condition that is not common in hybrid organic-inorganic perovskite materials.

5.1 $MAPbBr_3$ NANOCRYSTALS SYNTHESIS AND DEPOSITION TECHNIQUE

In a typical synthesis of methylammonium lead tri-bromide ($MAPbBr_3$) nanocrystals, 0.16 mmol of methylammonium bromide (MABr) and 0.20 mmol of lead (II) bromide $PbBr_2$ are dissolved in 5 mL of n,n-dimethylformamide (DMF).

[157] with a certain amount of n-octylamine, an alkyl chain with eight carbon atoms, ending with an amine group acting as ligand.

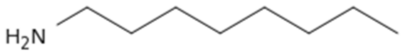

Figure 5.1.1: n-Octylamine chemical formula.

The reference solution has 0.4% v/v of ligands with respect to the starting solution. This value comes after an optimization of the amount of the alkyl chain needed to passivate the surface of the nanocrystals.

After leaving the solution stirring for one hour to complete the dissolution of the reagents in the solvent, 100 µL are injected into 10 mL of anhydrous chlorobenzene (CB) kept under vigorous stirring. Since CB is an anti-solvent, a solvent in which the perovskite is not soluble, the $MAPbBr_3$ nanocrystals are immediately formed and the solution turns immediately yellowish. The nanocrystals are then purified by a centrifugation step at 7000 r.p.m. for 10 minutes.

The biggest-size nanocrystals precipitate and are discarded. The obtained bright green colloidal solution is further investigated; this dispersion contains the smallest-size $MAPbBr_3$ nanocrystals in anhydrous CB that were not discarded after centrifugation.

What is formed upon the injection, is schematically represented in Figure 5.1. A shell of alkyl chain (green color in the sketch) completely covers a core of $MAPbBr_3$ (yellow color in the sketch). The coverage of the shell on the core permits the passivation of the defects on the surface of the nanocrystals and the passivation permits an increasing in the PLQY values.

Once the synthesis is done, the nanocrystals were deposed by spray coating; this is a technique used to depose thin film on different kind of substrates by using a spray coater machine or air-pressurized spray gun. The gun can have different types of nozzles, shapes and sizes. This technique permits to obtain a uniform and smooth film, after a first optimization of different parameters (i.e. the concentration of the ink, the amount of ink, the distance and the temperature of the sample…).

The technique used in our laboratory is called manual mode; the air-gun is moved manually on the substrate, with a distance of about 10-20 cm between nozzles and surface where the material is deposed.

5.2 $MAPbBr_3$ NANOCRYSTALS CHARACTERIZATION

The first analysis done is a study on the optimized ratio of the ligand in the initial solution. Starting from 0.2 % v/v increasing to 1.2 % v/v, the formation of nanocrystals has been investigated. The variation of ligand permits to see its effect on the nanocrystals' formation.

The absorbance and photoluminescence of the obtained dispersions are showed in Figure 5.2.1a and Figure 5.2.1b, respectively.

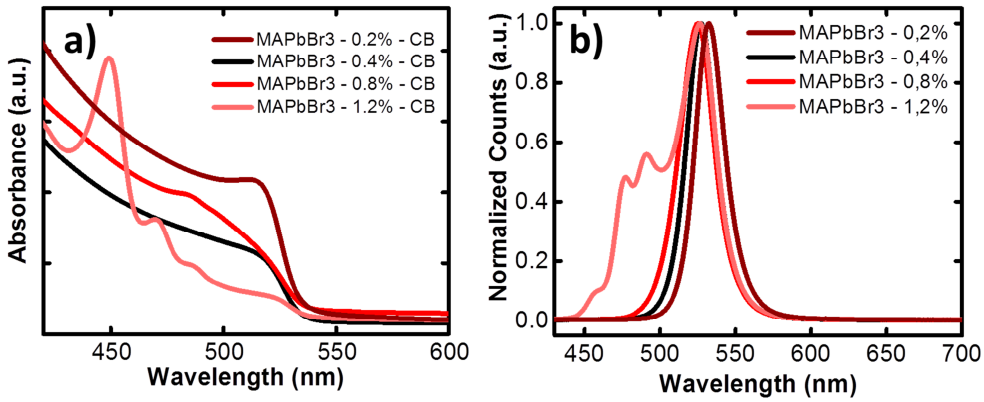

Figure 5.2.1: optical characterization for dispersion containing nanocrystals with different amount of n-octylamine (a) absorbance spectra and (b) steady state photoluminescence.

The different amount of ligand, bring to the formation of different profiles in the absorbance band edge. This permits to assume that different concentrations of ligand bring to different sizes of nanocrystals produced and for this reason a shift of the band edge. This assumption is further confirmed by the blue shift of the nanocrystals $MAPbBr_3$ photoluminescence peak by increasing the amount of ligands in the synthesis.

When the amount of ligand is increased up to 1.2 % v/v, an excitonic peak in the absorbance appears at low (~ 450 nm) wavelength. The presence of this peak

confirms that two dimensional perovskite nanocrystals are formed during the synthesis process. [158]
For the further analysis nanocrystals with 0.4% v/v n-octylamine in the solution have been considered because they have the highest PLQY value.

The synthetized nanocrystals were deposed by spray coating technique. The most simplified process uses a manual air-gun. The deposition is done under the fumehood, to avoid inhaling harmful solvents such as chlorobenzene, where the nanocrystals are dispersed in. The substrate is on top of an hot plate and it is heated up to 70 °C to permit the evaporation of the little drops of solvents coming out from the spray nozzle in few seconds after the deposition.
The temperature is kept at 70 °C even for high boiling point solvents (i.e. chlorobenzene) and not higher temperature to not induce the aggregation of the nanocrystals on the substrate but only the evaporation of the solvent.

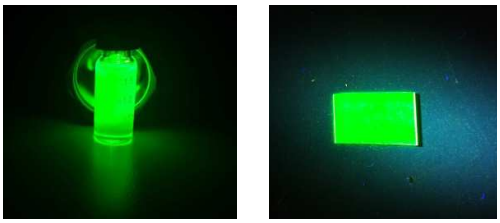

Figure 5.2.2: picture of the dispersion of $MAPbBr_3$ in chlorobenzene (on the left side) and $MAPbBr_3$ nanocrystals deposed on a glass slide by spray coating (on the right side). Both the samples are illuminated with a UV torch light.

Since the concentration of the nanoparticles in the dispersion is not high, the deposition by spray coater has been done for several minutes and, to have a uniform deposition of the material, the substrate has been rotated with a slow but uniform speed. After the deposition of the active material, the absorbance and the normalized steady state photoluminescence is investigated. Moreover, the sample is left over 10 days in ambient atmosphere and the absorbance and photoluminescence are showed in Figure 5.2.3. No differences are present in PL-normalized shape and only a small reduction can be observed in absorbance. This data confirm the robustness and the stability of the material covered by a protective shell even in ambient conditions.

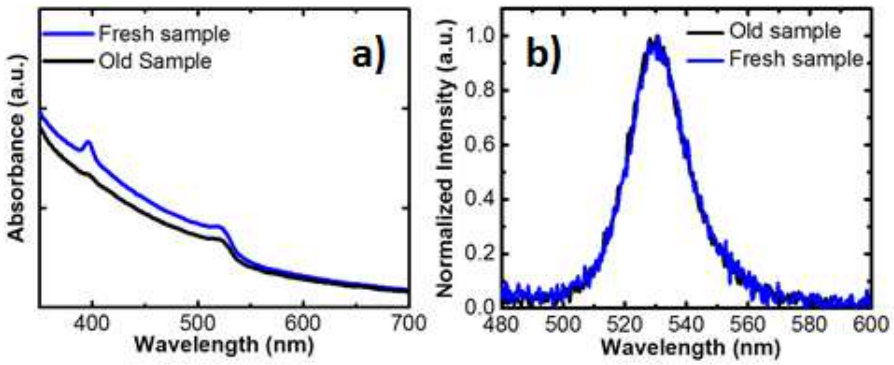

Figure 5.2.3: optical characterization for thin film samples (a) absorbance spectra and (b) steady state photoluminescence for "fresh" (as deposited – blue line) and "old" (after 10 days from the deposition – black line). The sample is left for 10 days in ambient atmosphere.

Once the deposition is done and the solvent is evaporated, the presence of the excitonic peak in the absorption spectra, shows even at lower ligand concentration the presence of two dimensional materials.

This presence is further confirmed by X-Ray Diffraction analysis showed in Figure 5.2.4a. The peak at low angles (Two Theta ~ 9°), shows the presence of low dimensional perovskite material, while the peak at Two Theta ~ 12.6° shows the presence of unreacted $PbBr_2$. The presence of lead (II) bromide is predictable because of the starting stoichiometry of the reaction, where a small amount of excess of $PbBr_2$ is used with respect to methylammonium bromide (0.2 mmol of $PbBr_2$ versus 0.16 mmol of MABr). The peak at Two Theta ~ 15° reveals the (001) diffraction plane for three dimensional $MAPbBr_3$ perovskite material

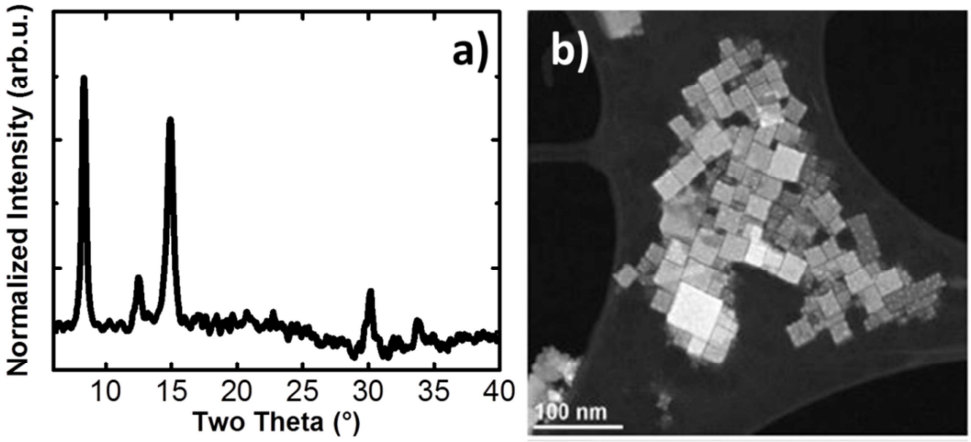

Figure 5.2.4: characterization of $MAPbBr_3$ nanocrystals with 0.4% v/v n-octylamine (a) X-Ray Diffraction spectra showing the presence of low dimensional perovskite (Two theta ~ 9°), excess of lead (II) bromide (~ 12.6°) and diffraction planes for $MAPbBr_3$.(~ 15°, ~ 30°). (b) Transmission Electron Microscope (TEM) image of drop casted nanocrystals on ultrathin carbon/holey-carbon film coated Cupper grid.

The TEM image shown in Figure 5.2.4b, permits to individuate cuboidal crystals with an average size of 27 nm on diagonal of the projection viewed. Under e-beam irradiation, the nanocrystals exhibit lead-segregation and by the images from elemental mapping, is possible to individuate a carbon shell around the nanocrystals, showed in Figure 5.2.5.

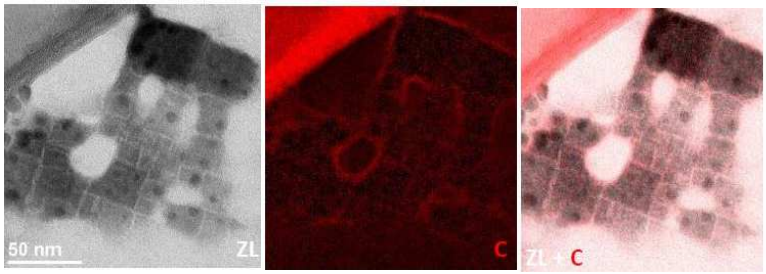

Figure 5.2.5: TEM images of drop casted $MAPbBr_3$ nanocrystals. (a) Elastically filtered bright-field (zero loss), (b) Elastically filtered bright-field TEM (map of carbon) and (c) Elastically filtered bright-field TEM (map of carbon and zero loss).

After the first analysis on the morphology of the material, a deep study on optical properties is done. It has been monitored the PLQY at different decades of excitation power, directly correlated to fluence (Figure 5.2.6). The fluence is defined as the ratio between the power of the laser divided by area of the spot of the laser.

The power dependent relative photoluminescence excitation analysis is analyzed by an unfocused CW diode laser at 405 nm (Oxxius). The spectra is collected in reflection geometry through an integrating sphere and focused into a fiber coupled to a spectrometer (Ocean Optics MAYA Pro 2000). The measurements are taken starting from low to high power. The resulting spectra was integrated in the range of 400 nm to 700 nm. All measurements were taken at room temperature, in air. The values are calculated by using the following formula:

$$PLQY\ \% = \frac{emitted\ photons}{absorbed\ photons} * 100\ .$$

The sphere used to determine the PLQY has an inner surface covered by a material that reflects all the radiation inside the sphere. These reflected and diffused photons are collected into a fiber coupled to a spectrometer. The CCD is connected to a PC and, with a specific software, is possible to analyze the signal coming from the sample and is possible to calculate the photoluminescence quantum yield.

To determine the PLQY% value, three measurements are needed:

- The empty sphere, with the laser reflected inside.
- The sample inside the sphere, with the laser that does not hit the sample.
- The sample inside the sphere, with the laser that hit the sample.

After these measurements is possible to calculate the photoluminescence quantum yield with a simple analysis. This analysis take into account the integrated area of the photoluminescence peaks measured by the PL experiment.[159]

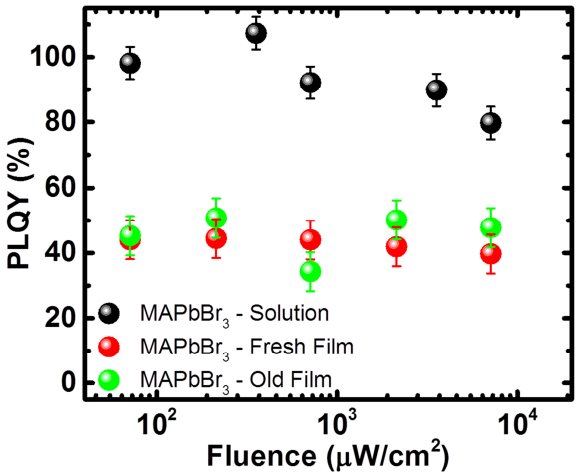

Figure 5.2.6: Photoluminescence quantum yield (PLQY %) versus fluence of light. For $MAPbBr_3$ dispersed in chlorobenzene (black dots), $MAPbBr_3$ nanocrystals measured as soon as deposited on glass by spray coater (red dots), $MAPbBr_3$ nanocrystals deposed on glass and measured after being exposed to the atmosphere for 10 days (green dots).

The analysis through PLQY shows a flat trend by increasing the incident power with an average of 92% for $MAPbBr_3$ nanocrystals in solution, while the nanocrystals deposited by spray coating on glass have a PLQY% ~ 45% on average both for fresh sample, measured as soon as the material is deposed and for the same sample, left in atmosphere for 10 days.

Another spectroscopic proof that sustains the presence of a shell that covers the "bulky" nanocrystal-material is showed in Figure 5.2.7 where the spray coated thin film composed by nanocrystals on bare glass it's excited with a 400 nm pulsed laser at 1MHz with a fluence ~1 nJ/cm^2 that corresponds to an excitation density of ~ 10^{13}.

In the figures is possible to recognize a fast component in the PL decay on the blue side of the spectrum and this is possibly related to the transfer from 2D shell to 3D nanocrystals. Further analysis are anyway needed to validate our theory.

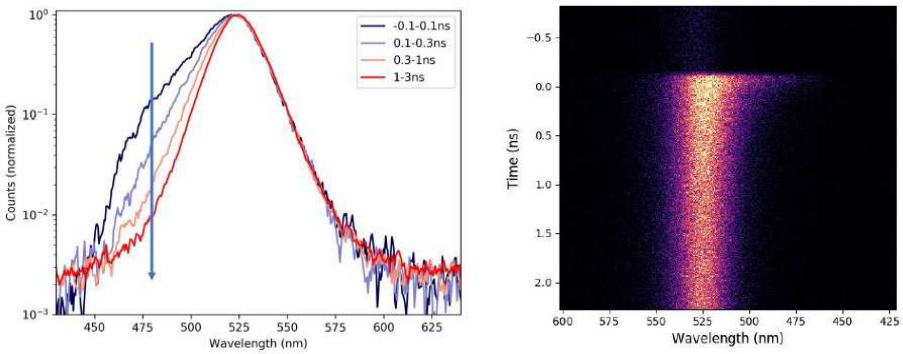

Figure 5.2.7: Time Resolved with Streak camera in slow sweep mode. A fast component on the blue side of the spectra is detected.

Another important parameter to fully characterized a material from the optical point of view is the carrier lifetime after the photo-generation. The lifetime can be monitored by the *time resolved photoluminescence* (trPL) measurement.

The result of this measurement is showed in Figure 5.2.8. The excitation used has a wavelength of 540 nm and the carrier lifetime is up to 1200 ns. This value is extremely high in a thin film and it is comparable to $MAPbBr_3$ single crystals proving that the quality of our nanocrystals is high and a full passivation is done on top of the surfaces.

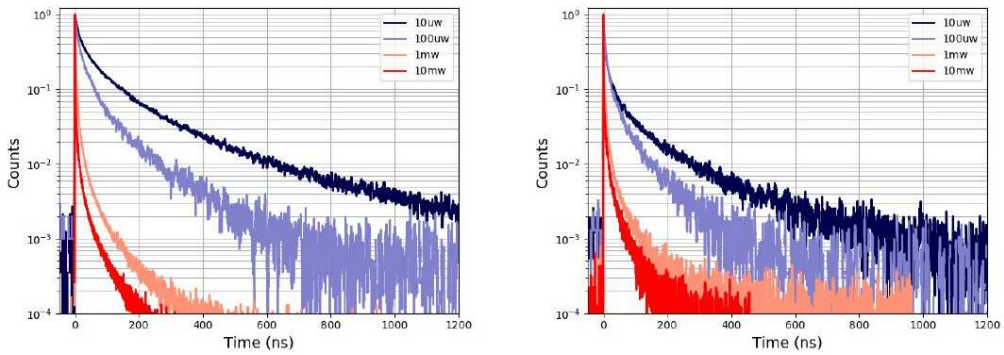

Figure 5.2.7: Time Resolved Photoluminescence for nanocrystals deposed on glass by air-gun.

Chapter 6

Conclusions

During the Ph.D. period I've been working with perovskite materials. This promising class of semiconductor that might revolutionize the opto-electronic devices still has some open questions such as the presence of lead, the toxicity of the solvents that are usually used and it lacks in terms of stability in environmental conditions and in terms of photo-stability upon exposure to light.

One approach that can answer to these open questions around perovskite materials, might be the realization and the optimization of inks. The inks are formed from perovskite crystals with a size in the order of nano- to micro- depending on the synthesis procedure and the application directly dispersed in solvents. Having perovskite crystals already formed in the ink, permits to not care about the crystallization in situ of the material that is strongly correlated to the environmental condition during synthesis and deposition process. This may reduce the possibility to handle materials with different opto-electronic properties that are correlated with the morphology of the material itself.

Thanks to the fact that different band-gaps can be obtained with hybrid organic-inorganic materials simply by changing the halide composition, different synthesis strategies were followed, obtaining different inks each of them specific for the own desired application.

During the Ph.D. period were developed three different kind of inks, containing perovskite with nano- or micro- crystals size. The synthesis, the size and the band gap of the material is thought to be specific and used in an particular application considering the morphology and the optical and electronic properties of the material. All the deposition processes are done by using different printing techniques and the solvents used during the printing has been, where was possible, a not harmful and low boiling point solvent to reduce the risk in handling the materials.

The first ink discussed in the Ph.D. thesis, the $MAPbI_3$ ink, we were able to obtain sub-micrometer hybrid organic-inorganic perovskite particles first synthetized in water and propan-2-ol and then dispersed in non-hazardous alcohol solvents. The usage of such non-hazardous solvents to synthetize and print perovskite-based devices is innovative and never exploited before. The material obtained is an high quality material, reproducible and up-scalable in large quantity. The stability of the material both in ambient condition and in working condition (protracted light soaking and repeated bias sweeps) confirms the novelty and the importance of such inks. Moreover, we showed the possibility to print these inks by bar-coating, a large area and roll-to-roll compatible technique, obtaining a simple planar geometry perovskite-based light detector. These devices show excellent photo-conducting response when the active phase is functionalized with a small molecule called PCBM. The fullerene derivative on one hand passivates hole traps, enhancing hole transport through the semiconductor material and reduces the photo-response time to 14 µs, corresponding to a maximum operation frequency of 35 kHz; on the other hand, PCBM acts as an acceptor phase for electrons, thus increasing the photoconductive gain. As a final result, the device achieves a record high gain-bandwidth product for printed perovskite light detectors, 1.5×10^7 Hz. Importantly, the defects passivation also strongly suppresses *1/f* noise, so that shot noise dominates already above 4 kHz. Thanks to the good dynamic response, the device can be operated in such frequency region, reaching the very high specific detectivity of 7.23×10^{13} cm $Hz^{0.5}$/W which is the highest measured D^* for any printed photodetector till date and with values that are slightly higher than commercially available silicon photodiodes. These characteristics open up

attractive possibilities to use printable perovskite for large area light detection applications and imaging applications.

The second ink discussed in the Ph.D. thesis, is the fully inorganic $CsPbBr_3$ ink. This ink, firstly developed in Istituto Italiano di Tecnologia in Genova, was optimized in our laboratory and we show the possibility to increase till 1 cm^2 the active area of the solar cell device with a wide band gap.
The synthesis conditions are varied to have full control on the products. The obtained nanocrystals can be fully three dimensional perovskite nanocrystals or a mix between two dimensional nanoplatelets and three dimensional perovskite nanocrystals. The obtained material has been characterized and the semiconducting, three dimensional nanocrystals are printed by an automatized bar coater to fabricate solar cells devices built in a standard structure configuration. Working devices with high open circuit voltage are tested in air without any kind of encapsulation. They showed stability both in environmental condition and during operation at the maximum power point.
The possibility to control the size of the nanocrystals by changing the concentration of precursors and the dispersant solvent polarity and boiling point permitted to maximize the packing and the smoothness of the active layer in the solar cell device. These devices are tested both under solar simulator and under white LED board to simulate an application for indoor light harvesting.
The obtained inks permit to realize tandem solar cells with tunable band gap absorbing materials such as tandem perovskite/perovskite configuration or tandem perovskite/silicon configuration.

The third and last ink is an highly luminescent dispersion of $MAPbBr_3$ nanocrystals. After an optimization of the nanocrystals ligand concentration and an optimization of the deposition through spray coater technique, the material is characterized from the optical properties point of view. The goal of improving in luminescence stability and enhancing the PL efficiency of nanocrystals is achieved by growing a shell of a wider band gap semiconductor on top of the narrower band gap one. This structure is known as core–shell semiconducting nanocrystals. The presence of the shell, improves the photoluminescence quantum yield (~ 90 % in solution and ~ 50 % in thin film) by confining the charge carriers and it also passivates defects and non-radiative recombination sites that are present on the

surfaces of the perovskite nanocrystals. TEM images confirm the presence of an organic shell around the nanocrystals, while time resolved photoluminescence (trPL) shows an extremely long carrier lifetime due to the fact that all the non-radiative path are passivated by amino groups. Finally the trPL map shows a fast decay in the blue region and a slower decay around 525 nm. This suggests a transfer from two dimensional shell to three dimensional nanocrystals. Moreover, this core/shell nanocrystals result to be stable also when exposed to environmental conditions. Such high PLQY, long carrier lifetime decay and stability are fundamental characteristics for active emitting materials in LED.

Thanks to the amazing properties and devices performances, the three inks developed in our laboratory, might revolutionize the opto-electronic applications, opening the doors of the market to perovskite-based devices.

References

[1] Grätzel M., The light and shade of Perovskite solar cells, Nature Materials, volume 13, pages 838–842 (2014).

[2] Pacchioni G., Lezioni di Chimica dello Stato Solido, I.S.U. (1999).

[3] Krishnamoorthy T., Ding H., Yan C., Leong W.L., Baikie T., Zhang Z., Sherburne M., Li S., Asta M., Mathews N., Mhaisalkarac S.G., Lead-free germanium iodide perovskite materials for photovoltaic applications, Journal of Materials Chemistry A, Issue 47 (2015).

[4] Cortecchia D., Dewi H.A., Yin J., Bruno A., Chen S., Baikie T., Boix P.P., Grätzel M., Mhaisalkar S., Soci C., Mathews N., Lead-Free MA2CuClxBr4–x Hybrid Perovskites, Inorg. Chem., 55 (3), pp 1044–1052 (2016).

[5] Locardi F., Cirignano M., Baranov D., Dang Z., Prato M., Drago F., Ferretti M., Pinchetti V., Fanciulli M., Brovelli S., De Trizio L., Manna L., Colloidal Synthesis of Double Perovskite Cs2AgInCl6 and Mn-Doped Cs2AgInCl6 Nanocrystals, J. Am. Chem. Soc., 140, 12989−12995 (2018).

[6] Park B.W., Philippe B., Zhang X., Rensmo H., Boschloo G., Johansson E.M.J., Bismuth Based Hybrid Perovskites A3Bi2I9 (A: Methylammonium or Cesium) for Solar Cell Application, Advanced Materials, Volume27, Issue43, Pages 6806-6813, (2015).

[7] Borriello I., Cantele G., Ninno D., Ab initio investigation of hybrid organic-inorganic perovskites based on tin halides, Physical Review B, vol. 77, no. 23, p. 235214 (2008).

[8] Pellet N., Gao P., Gregori G., Yang T.Y., Nazeeruddin M.K., Maier J., Grätzel M., Mixed-Organic-Cation Perovskite Photovoltaics for Enhanced Solar-Light Harvesting, Angewandte Chemie, Volume 53, Issue12, Pages 3151-3157 (2014).

[9] Tan W., Bowring A.R., Meng A.C., McGehee M.D., McIntyre P.C., Thermal Stability of Mixed Cation Metal Halide Perovskites in Air, ACS Appl. Mater. Interfaces, 10 (6), pp 5485–5491 (2018).

[10] Saliba M., Matsui T., Seo J.Y., Domanski K., Correa-Baena J.P., Nazeeruddin M., Zakeeruddin S.M., Tress W., Abate A., Hagfeldtd A., Grätzel M., Cesium-containing triple cation perovskite solar cells: improved stability, reproducibility and high efficiency, Energy & Environmental Science, Issue 6 (2016).

[11] Saliba M., Matsui T., Domanski K., Seo J.Y., Ummadisingu A., Zakeeruddin S.M., Correa-Baena J.P., Tress W.R., Abate A., Hagfeldt A., Grätzel M., Incorporation of rubidium cations into perovskite solar cells improves photovoltaic performance, Science, Vol. 354, Issue 6309, pp. 206-209 (2016).

[12] Ogomi Y., Morita A., Tsukamoto S., Saitho T., Fujikawa N., Shen Q., Toyoda T., Yoshino K., Pandey S.S., Ma T., CH3NH3SnxPb(1–x)I3 perovskite solar cells covering up to 1060 nm, The Journal of Physical Chemistry Letters, vol. 5, no. 6, pp. 1004–1011 (2014).

[13] Noh J.H., Im S.H., Heo J. H., Mandal T. N., Seok S.I., Chemical management for colorful, efficient, and stable inorganic–organic hybrid nanostructured solar cells, Nano letters, vol. 13, no. 4, pp. 1764–1769 (2013).

[14] Umari P., Mosconi E., De Angelis F., Relativistic gw calculations on $CH_3NH_3PbI_3$ and $CH_3NH_3SnI_3$ perovskites for solar cell applications, Scientific Reports, vol. 4 (2014).

[15] Miyata A., Mitioglu A., Plochocka P., Portugall O., Tse-Wei Wang J., Stranks S.D., Snaith H.J., Nicholas R.J., Direct measurement of the exciton binding energy and effective masses for charge carriers in organic–inorganic tri-halide perovskites, Nature Physics, volume 11, pages 582–587 (2015).

[16] Tanaka K., Takahashi T., Ban T., Kondo T., Uchida K., Miura N., Comparative study on the excitons in lead-halide-based perovskite-type crystals $CH_3NH_3PbBr_3$ and $CH_3NH_3PbI_3$, Solid state communications, vol. 127, no. 9, pp. 619–623, (2003).

[17] D'Innocenzo V., Grancini G., Alcocer M.J.P., Kandada A.R.S., Stranks S.D., Lee M.M., Lanzani G., Snaith H.J., Petrozza P., Excitons versus free charges in organo-lead tri-halide perovskites, Nature Communications volume 5, Article number: 3586 (2014).

[18] Stranks S.D., Eperon G.E., Grancini G., Menelaou C., Alcocer M.J.P., Leijtens T., Herz L.M., Petrozza A., Snaith H.J., Electron-Hole Diffusion Lengths Exceeding 1 Micrometer in an Organometal Trihalide Perovskite Absorber, Science, Vol 342 (2013).

[19] De Bastiani M., V. D'Innocenzo, Stranks S.D., Snaith H.J., Petrozza A., Role of the crystallization substrate on the photoluminescence properties of organo-lead mixed halides perovskites APL Materials 2, 081509 (2014).

[20] Ball J.M., Petrozza A., Defects in perovskite-halides and their effects in solar cells, Nature Energy, Volume 1, 16149 (2016).

[21] Snaith H.J., Perovskites: The Emergence of a New Era for Low-Cost, High-Efficiency Solar Cells, J. Phys. Chem. Lett., 4 (21), pp 3623–3630 (2013).

[22] Im J.-H., Kim H.-S., Park N.-G., Morphology-photovoltaic property correlation in perovskite solar cells: One-step versus two-step deposition of $CH_3NH_3PbI_3$, Apl Materials, vol. 2, no. 8, p. 081510 (2014).

[23] Burschka J., Pellet N., Moon S.-J., Humphry-Baker R., Gao P., Nazeeruddin M. K., Graetzel M., Sequential deposition as a route to high performance perovskite-sensitized solar cells, Nature, vol. 499, no. 7458, pp. 316–319 (2013).

[24] Ávila J., Momblona C., Boix P.P., Sessolo M., Bolink H.J., Vapor-Deposited Perovskites: The Route to High-Performance Solar Cell Production?, Joule, Volume 1, Issue 3, Pages 431-442 (2017).

[25] Jeon N.J., Noh J.H., Kim Y.C., Yang W.S., Ryu S., Seok S.I., Solvent engineering for high-performance inorganic–organic hybrid perovskite solar cells, Nature Materials, 13, 897–903 (2014).

[26] Sadhanala A., Deschler F., Thomas T.H., Dutton S.E., Goedel K.C., Hanusch F.C., Lai M.L., Steiner U., Bein T., Docampo P., Cahen D., Friend R.H., Preparation of Single-Phase Films of CH3NH3Pb(I1–xBrx)3 with Sharp Optical Band Edges, J. Phys. Chem. Lett., 5 (15), pp 2501–2505 (2014).

[27] Barker A.J., Sadhanala A., Deschler F., Gandini M., Senanayak S.P., Pearce P.M., Mosconi E., Pearson A.J., Wu Y., Kandada A.R.S., Leijtens T., De Angelis T., Dutton S.E., Petrozza A., Friend R.H., Defect-Assisted Photoinduced Halide Segregation in Mixed-Halide Perovskite Thin Films, ACS Energy Lett., 2, 1416−1424 (2017).

[28] Zhang H., Nazeeruddin M.K., Choy W.C.H., Perovskite Photovoltaics: The Significant Role of Ligands in Film Formation, Passivation, and Stability, Adv.Mater., 1805702 (2018).

[29] Noel N.K., Abate A., Stranks S.D., Parrott E.S., Burlakov V.M., Goriely A., Snaith H.J., Enhanced photoluminescence and solar cell performance via Lewis base passivation of organic-inorganic lead halide perovskites, .ACS Nano., 8(10):9815-21 (2014).

[30] Wang F., Geng W., Zhou Y., Fang H.H., Tong C.J., Loi M.A., Liu L.M., Zhao N., Phenylalkylamine Passivation of Organolead Halide Perovskites Enabling High-Efficiency and Air-Stable Photovoltaic Cells., Adv Mater., 28(45):9986-9992 (2016).

[31] National Renewable Energy Laboratory. (2018). NREL solar cell efficiency chart. https://www.nrel.gov/pv/assets/images/ efficiency-chart.png.

[32] Yang M., Kim D.H., Klein T.R., Li Z., Reese M.O., Tremolet de Villers B.J., Berry J.J., Van Hest M.F.A.M., Zhu K., Highly efficient perovskite solar modules by scalable fabrication and interconnection optimization. ACS Energy Lett. 3, 322–328 (2018).

[33] Chen P.Y.Y, Qi J., Klug M.T., Dang X., Hammond P.T., Belcher A.M., Environmentally responsible fabrication of efficient perovskite solar cells from recycled car batteries, Energy & Environmental Science, 7, 3659 (2014).

[34] Gardner K.L., Tait J.G., Merckx T., Qiu W., Paetzold U.W., Kootstra L., Jaysankar M., Gehlhaar R., Cheyns D., Heremans P., Nonhazardous solvent systems for processing perovskite photovoltaics, Adv. Energy Mater., 6, 1600386 (2016).

[35] Noel N.K., Habisreutinger S.N., Wenger B., Klug M.T., Hörantner M.T., Johnston M.B., Nicholas R.J., Moore D.T., Snaith H.J., A low viscosity, low boiling point, clean solvent system for the rapid crystallisation of highly specular perovskite films, Energy & Environmental Science, Issue 1 (2017).

[36] Grancini G., Roldán-Carmona C., Zimmermann I., Mosconi E., Lee X., Martineau D., Narbey S., Oswald S., De Angelis F., Graetzel M., Nazeeruddin M.K., One-Year stable perovskite solar cells by 2D/3D interface engineering, Nature Communications, volume 8, Article number: 15684 (2017).

[37] Luque, A. and Hegedus, S., Handbook of Photovoltaic Science and Engineering, Wiley-Blackwell, 2010.

[38] Tress, W., Organic Solar Cells Theory, Experiment and Device Simulation, Springer, Vol. 208 (2014).

[39] Nabet B., Photodetectors: Materials, Devices and Applications, Woodhead Publishing (2015).

[40] Hewig G. *et al*., *Proc. 16th IEEE Photovoltaic Specialist Conf.*, 713–718 (1982).

[41] Bragagnolo J. *et al*., *IEEE Trans. Electron Devices* **27**, 645–650 (1980).

[42] Alferov Z.I., Andreev V.M., Garbuzov D.Z., Zhilyaev Y.V., Morozov E.P., Portnoi E.L., Trofim V.G., Investigation of the influence of the AlAs–GaAs heterostructure parameters on the laser threshold current and the realization of continuous emission at room temperature, A.F. Ioffe Physicotechnical Institute, USSR Academy of Sciences (1970).

[43] Hall R., Birkmire R., Phillips J., Meakin J., *Appl. Phys. Lett.* 38, 925, 926 (1981).

[44] Mickelson R., Chen W., *Proc. 16th IEEE Photovoltaic Specialist Conf.*, 781–785 (1982).

[45] Tyan Y., Perez-Albuerne E., *Proc. 16th IEEE Photovoltaic Specialist Conf.*, 794–799 (1982).

[46] Kalyanasundaram K., Grätzel M., Metal Complexes as Photosensitizers in Photoelectrochemical Cells, in Kalyanasundaram K, Grätzel M, Eds, *Photosensitization and Photocatalysis Using Inorganic and Organometallic Compounds*, 247–271, Kluwer Academic Publishers, Dordrecht, Netherlands (1993).

[47] Smestad G., Bignozzi C., Argazzi R., *Sol. Energy Mater. Sol. Cells* 32, 259–273 (1994).

[48] Smestad G., *Sol. Energy Mater. Sol. Cells* 32, 259–288 (1994).

[49] Hagfeldt A., Grätzel M, *Chem. Rev.* 95, 49–68 (1995).

[50] Kay A., Grätzel M., *Sol. Energy Mater. Sol. Cells* 44, 99–117 (1996).

[51] Meng L., Zhang Y., Wan X., Li C., Zhang X., Wang Y., Ke X., Zuo Xiao, Liming Ding, Ruoxi Xia, Hin-Lap Yip, Yong Cao, Yongsheng Chen, Organic and solution-processed tandem solar cells with 17.3% efficiency, Science, eaat2612 (2018).

[52] Zhang S., Qin Y., Zhu J., Hou J., Over 14% Efficiency in Polymer Solar Cells Enabled by a Chlorinated Polymer Donor, Adv.Mater., 30, 1800868 (2018).

[53] Luque A., Marti A., Increasing the Efficiency of Ideal Solar Cells by Photon Induced Transitions at Intermediate Levels, *Phys. Rev. Lett.* 78, 5014 (1997).

[54] Johnston, Pattantyus-Abraham, Clifford, Myrskog, MacNeil, Levina, E.H. Sargent, Schottky-quantum dot photovoltaics for efficient infrared power conversion, Appl. Phys. Lett., 92, 151115 (2008).

[55] Sanehira E.M., Marshall A.S., Christians J.A., Harvey S.P., Ciesielski P.N., Wheeler L.M., Schulz P., Lin L.Y., Beard M.C., Luther J.M., Enhanced mobility CsPbI3 quantum dot arrays for record-efficiency, high-voltage photovoltaic cells, Science Advances, Vol. 3, 10, eaao4204 (2017).

[56] Kim H.S., Lee C.R., Im J.K., Lee K.B., Moehl T., Marchioro A., Moon S.J., Humphry-Baker R., Yum J.H., Moser J.E., Grätzel M., Park N.G., Lead Iodide Perovskite Sensitized All-Solid-State Submicron Thin Film Mesoscopic Solar Cell with Efficiency Exceeding 9 %, Scientific Reports, 2, 591 (2012).

[57] Lee M.M., Teuscher J., Miyasaka T., Murakami T.N., Snaith H.J., Efficient Hybrid Solar Cells Based on Meso-Superstructured Organometal Halide Perovskites, Science, 1228604 (2012).

[58] Zhao D., Wang C., Song Z., Yu Y., Chen C., Zhao Z., Zhu K., Yan Y., Four-Terminal All-Perovskite Tandem Solar Cells Achieving Power Conversion efficiencies Exceeding 23%, ACS Energy Lett., 3 (2), pp 305–306 (2018).

[59] National Renewable Energy Laboratory, http://www.nrel.gov.

[60] Ferrari G., Sampietro M., Correlation spectrum analyzer for direct measurement of device current noise, Rev. Sci. Instrum., vol. 73, no. 7, p. 2717, (2002).

[61] Saidaminov M. I., Planar-integrated single-crystalline perovskite photodetectors. Nature Communications 6, 8724 (2015).

[62] Fang Y., Huang J., Resolving Weak Light of Sub-picowatt per Square Centimeter by Hybrid Perovskite Photodetectors Enabled by Noise Reduction, Advanced Materials 27, 2804-2810 (2015).

[63] Sutherland B. R., Sensitive, Fast, and Stable Perovskite Photodetectors Exploiting Interface Engineering, ACS Photonics 2, 1117-1123 (2015).

[64] Wang H., Kim D. H., Perovskite-based photodetectors: materials and devices, Chemical Society Reviews 46, 5204-5236 (2017).

[65] Chen P.-Y., Environmentally responsible fabrication of efficient perovskite solar cells from recycled car batteries, Energy & Environmental Science 7, 3659-3665 (2014).

[66] Binek A., Recycling Perovskite Solar Cells To Avoid Lead Waste, ACS Applied Materials & Interfaces 8, 12881-12886 (2016).

[67] Gardner Kira L., Nonhazardous Solvent Systems for Processing Perovskite Photovoltaics, Advanced Energy Materials 6, 1600386 (2016).

[68] Hu Q., Large-area perovskite nanowire arrays fabricated by large-scale roll-to-roll micro-gravure printing and doctor blading, Nanoscale 8, 5350-5357 (2016).

[69] Liu Y., Inkjet-Printed Photodetector Arrays Based on Hybrid Perovskite CH3NH3PbI3 Microwires, ACS Applied Materials & Interfaces 9, 11662-11668 (2017).

[70] Tong S., Large-area and high-performance CH3NH3PbI3 perovskite photodetectors fabricated via doctor blading in ambient condition, Organic Electronics 49, 347-354 (2017).

[71] Li S., et al. Fast-response and high-responsivity FAxMA(1−x)PbI3 photodetectors fabricated via doctor-blading deposition in ambient condition, Organic Electronics 52, 190-194 (2018).

[72] Clusters in solution: Growth and optical properties of layered semiconductors with hexagonal and honeycombed structures. The Journal of Chemical Physics 85, 5337-5340 (1986).

[73] Ha, S. T. et al. Synthesis of Organic–Inorganic Lead Halide Perovskite Nanoplatelets: Towards High-Performance Perovskite Solar Cells and Optoelectronic Devices, Advanced Optical Materials 2, 838-844 (2014).

[74] Khim D., et al. Simple Bar-Coating Process for Large-Area, High-Performance Organic Field-Effect Transistors and Ambipolar Complementary Integrated Circuits, Advanced Materials 25, 4302-4308 (2013).

[75] Bucella S.G., Macroscopic and high-throughput printing of aligned nanostructured polymer semiconductors for MHz large-area electronics, Nature Communications 6, 8394 (2015).

[76] Manshor N.A., Wali Q., Kan Wong K., Muzakir S.K., Fakharuddin A., Schmidt-Mendeb L., Jose R., Humidity versus photo-stability of metal halide perovskite films in a polymer matrix, Phys. Chem. Chem. Phys., 18, 21629-2163 (2016).

[77] Konstantatos, G. and Sargent, E. H. Nanostructured materials for photon detection. Nature Nanotechnology 5, 391 (2010).

[78] Liu J.-M., Photonic Devices. (Cambridge University Press, 2005).

[79] Jie J.S., et al. Photoconductive Characteristics of Single-Crystal CdS Nanoribbons, Nano Letters 6, 1887-1892 (2006).

[80] Irkhin P., Najafov H., Podzorov V., Steady-state photoconductivity and multi-particle interactions in high-mobility organic semiconductors, Scientific Reports 5, 15323 (2015).

[81] Stöckmann F., On the Dependence of Photocurrents on the Excitation Strength. physica status solidi (b) 34, 741-749 (1969).

[82] Leijtens T., et al. Carrier trapping and recombination: the role of defect physics in enhancing the open circuit voltage of metal halide perovskite solar cells, Energy & Environmental Science 9, 3472-3481 (2016).

[83] Meggiolaro D., et al. Iodine chemistry determines the defect tolerance of lead-halide perovskites. Energy & Environmental Science 11, 702-713 (2018).

[84] Zheng X., et al. Defect passivation in hybrid perovskite solar cells using quaternary ammonium halide anions and cations. Nature Energy 2, 17102 (2017).

[85] De Bastiani M., et al. Ion Migration and the Role of Preconditioning Cycles in the Stabilization of the J–V Characteristics of Inverted Hybrid Perovskite Solar Cells. Advanced Energy Materials 6, 1501453 (2015).

[86] Hooge F. N., Kleinpenning, T. G. M., Vandamme, L. K. J. Experimental studies on 1/f noise. Reports on Progress in Physics 44, 479 (1981).

[87] Ziel A.V.D., et al. Unified presentation of 1/f noise in electron devices: fundamental 1/f noise sources. Proceedings of the IEEE 76, 233-258 (1988).

[88] Liu G., Rumyantsev, S., Shur, M. S., Balandin, A. A. Origin of 1/f noise in graphene multilayers: Surface vs. volume. Applied Physics Letters 102, 093111 (2013).

[89] Ciofi C., et al. A New Circuit Topology for the Realization of Very Low-Noise Wide-Bandwidth Transimpedance Amplifier. IEEE Transactions on Instrumentation and Measurement 56, 1626-1631 (2007).

[90] Song J., et al. Monolayer and Few-Layer All-Inorganic Perovskites as a New Family of Two-Dimensional Semiconductors for Printable Optoelectronic Devices. Adv. Mater. 28, 4861-4869 (2016).

[91] Hu X., et al. High-Performance Flexible Broadband Photodetector Based on Organolead Halide Perovskite. Adv. Funct. Mater. 24, 7373-7380 (2014).

[92] Lian Z., et al. High-Performance Planar-Type Photodetector on (100) Facet of MAPbI3 Single Crystal. Sci Rep 5, 16563 (2015).

[93] Ka I., et al. High-performance nanotube-enhanced perovskite photodetectors. Sci Rep 7, 45543 (2017).

[94] Gao L., et al. Passivated Single-Crystalline CH3NH3PbI3 Nanowire Photodetector with High Detectivity and Polarization Sensitivity. Nano Lett. 16, 7446-7454 (2016).

[95] Saidaminov M. I., et al. Planar-integrated single-crystalline perovskite photodetectors. Nat. Commun. 6, 8724 (2015).

[96] Adinolfi V., et al. Fast and Sensitive Solution-Processed Visible-Blind Perovskite UV Photodetectors. Adv. Mater. 28, 7264-7268 (2016).

[97] Yang Z., et al. High-Performance Single-Crystalline Perovskite Thin-Film Photodetector. Adv. Mater. 30, 1704333 (2018).

[98] Lee Y., et al. High-performance perovskite-graphene hybrid photodetector. Adv. Mater. 27, 41-46 (2015).

[99] Wang Y., et al. Solution-Processed MoS2 /Organolead Trihalide Perovskite Photodetectors. Adv. Mater. 29, (2017).

[100] Wang Y., et al. Hybrid Graphene-Perovskite Phototransistors with Ultrahigh Responsivity and Gain. Advanced Optical Materials 3, 1389-1396 (2015).

[101] Sutherland B.R., et al. Sensitive, Fast, and Stable Perovskite Photodetectors Exploiting Interface Engineering. ACS Photonics 2, 1117-1123 (2015).

[102] Dou L., et al. Solution-processed hybrid perovskite photodetectors with high detectivity. Nat. Commun. 5, 5404 (2014).

[103] Lin Q., et al. Low Noise, IR-Blind Organohalide Perovskite Photodiodes for Visible Light Detection and Imaging. Adv. Mater. 27, 2060-2064 (2015).

[104] Fang Y., Huang, J. Resolving Weak Light of Sub-picowatt per Square Centimeter by Hybrid Perovskite Photodetectors Enabled by Noise Reduction. Adv. Mater. 27, 2804-2810 (2015).

[105] Hu Q., et al. Large-area perovskite nanowire arrays fabricated by large-scale roll-to-roll micro-gravure printing and doctor blading. Nanoscale 8, 5350-5357 (2016).

[106] Liu Y., et al. Inkjet-Printed Photodetector Arrays Based on Hybrid Perovskite CH3NH3PbI3 Microwires. ACS Appl. Mater. Interfaces 9, 11662-11668 (2017).

[107] Deng W., et al. Aligned Single-Crystalline Perovskite Microwire Arrays for High-Performance Flexible Image Sensors with Long-Term Stability. Adv. Mater. 28, 2201-2208 (2016).

[108] Tong S., et al. Large-area and high-performance CH3NH3PbI3 perovskite photodetectors fabricated via doctor blading in ambient condition. Org. Electron. 49, 347-354 (2017).

[109] Konstantatos G., et al. Ultrasensitive solution-cast quantum dot photodetectors. Nature 442, 180 (2006).

[110] Zhang, Q., et al. Solution-Processed Graphene Quantum Dot Deep-UV Photodetectors. ACS Nano 9, 1561-1570 (2015).

[111] Johnston, M.B.; Herz, L.M. Hybrid Perovskites for Photovoltaics: Charge-Carrier Recombination, Diffusion, and Radiative Efficiencies. Acc. Chem. Res., 49, 146-54 (2016).

[112] Giorgi, G.; Fujisawa, J.-I.; Segawa, H.; Yamashita, K. J. Cation Role in Structural and Electronic Properties of 3D Organic–Inorganic Halide Perovskites: A DFT Analysis. Phys. Chem. Lett., 4, 4213 (2013).

[113] Leijtens, T.; Stranks, S. D.; Eperon, G. E.; Lindblad, R.; Johansson, E. M.; McPherson, I. J.; Rensmo, H.; Ball, J. M.; Lee, M.M.; Snaith, H. J. Electronic properties of meso-superstructured and planar organometal halide perovskite films: charge trapping, photodoping,and carrier mobility. ACS Nano, 8, 7147−7155 (2014).

[114] Koh, T.M.; Fu, K.; Fang, Y.; Chen, S.; Sum, T.C.; Mathews, N.; Mhaisalkar, S.G.; Boix, P.P.; Baikie, T. Formamidinium-Containing Metal-Halide: An Alternative Material for Near-IR Absorption Perovskite Solar Cells. J. Phys. Chem. C, 118 (30), 16458–16462 (2014).

[115] Park, N.G.; Perovskite solar cells: an emerging photovoltaic technology. Materials Today, 2, 65-72 (2015).

[116] Liu, M.; Johnston, M. B.; Snaith, H. J. Efficient planar heterojunction perovskite solar cells by vapour deposition. Nature, 501, 395−398 (2013).

[117] Docampo, P.; Ball, J. M.; Darwich, M.; Eperon, G. E.; Snaith, H.J. Efficient organometal trihalide perovskite planar-heterojunction solar cells on flexible polymer substrates. Nat. Commun., 4, 2761 (2013).

[118] Heo, J. H.; Im, S. H.; Noh, J. H.; Mandal, T. N.; Lim, C.; Chang, J. A.; Lee, Y. H.; Kim, H.; Sarkar, A.; Nazeeruddin, M. K.; Gratzel, M.; Seok, I. S. Efficient inorganic−organic hybrid heterojunction solar cells containing perovskite compound and polymeric hole conductors. Nat. Photonics, 7, 486−491 (2013).

[119] NREL chart, http://www.nrel.gov/ncpv/images/efficiency_chart.jpg.

[120] Tan, Z.K.; Moghaddam, R.S.; Lai, M.L., Docampo, P.; Higler, R.; Deschler, F.; Price, M.; Sadhanala, A.; Pazos, L..M.; Credgington, D.; Hanusch, F.; Bein, T.; Snaith, H.J.; Friend, R.H. Bright light-emitting diodes based on organometal halide perovskite. Nat. Nanotechnol., 9, 687–692 (2014).

[121] Li, G.; Tan, Z.-K.; Di, D.; Lai, M.L.; Jiang, L.; Hua-Wei Lim, J.; Friend, R.H.; Greenham, N.C. Efficient Light-Emitting Diodes Based on Nanocrystalline Perovskite in a Dielectric Polymer Matrix. Nano Lett., 15 (4), 2640–2644 (2015).

[122] Kim, Y.-K.; Cho, H.; Heo, J.H.; Kim, T.-S.; Myoung, N.; Lee, C.-L.; Im, S.H.; Lee, T.-W.; Multicolored organic/inorganic hybrid perovskite light-emitting diodes. Adv. Mater., 27, 1248–1254 (2015).

[123] Dou, L., Yang, Y. M.; You, J.; Hong, Z.; Chang, W.H.; Li, G.; Yang Y. Solution-processed hybrid perovskite photodetectors with high detectivity. Nat. Commun., 5, 5404 (2014).

[124] Saidaminov, M. I.; Adinolfi, V.; Comin, R.; Abdelhady, A.L.; Peng, W.; Dursun, I.; Yuan, M.; Hoogland, S.; Sargent E.H.; Bakr, O.M. Planar-integrated single-crystalline perovskite photodetectors. Nat. Commun. 2015, 6, 8724.

[125] Fang, Y.; Huang, J. Resolving Weak Light of Sub-picowatt per Square Centimeter by Hybrid Perovskite Photodetectors Enabled by Noise Reduction. Adv. Mat. 2015, 27, 17, 2804-2810.

[126] Deschler, F.; Price, M.; Pathak, S.; Klintberg, L.E.; Jarausch, D.D.; Higler, R.; Hüttner, S.; Leijtens, T.; Stranks, S.D.; Snaith, H.J.; Atatüre, M.; Phillips, R.T.; Friend, R.H. High Photoluminescence Efficiency and Optically Pumped Lasing in Solution-Processed Mixed Halide Perovskite Semiconductors. J. Phys. Chem. Lett., 2014, 5 (8), 1421–1426

[127] Xing, G.; Mathews, N.; Lim, S.S.; Yantara, N.; Liu, X.; Sabba, D.; Grätzel, M.; Mhaisalkar, S.; Sum, T.C. Low-temperature solution-processed wavelength-tunable perovskites for lasing. Nat. Materials, 13, 476–480 (2014).

[128] Sutherland, B.R.; Hoogland, S.; Adachi, M.M.; Wong, C.T.; Sargent, E.H. Conformal organohalide perovskites enable lasing on spherical resonators. ACS Nano, 8(10), 10947-52 (2014).

[129] X. Y. Chin, D. Cortecchia, J. Yin, A. Bruno, C. Soci. Lead iodide perovskite light-emitting field-effect transistor. Nature Commun., 6, 7383 (2015).

[130] Li, F.; Ma, C.; Wang, H.; Hu, W.; Yu, W.; Sheikh, A.D.; Wu, T. Ambipolar solution-processed hybrid perovskite phototransistors. Nat. Commun., 6, 8238 (2015).

[131] Sharenko, A.; Toney, M.F. Relationships between Lead Halide Perovskite Thin-Film Fabrication, Morphology, and Performance in Solar Cells. J. Am. Chem. Soc., 138 (2), 463–470 (2016).

[132] Eperon, G.E.; Paternò, G.M.; Sutton, R.J.; Zampetti, A.; Haghighirad, A.A.; Cacialli, F.; Snaith, H.J. Inorganic caesium lead iodide perovskite solar cells. J. Mater. Chem. A, 3, 19688-19695 (2015).

[133] Sutton, R.J.; Eperon, G.E.; Miranda, L.; Parrott, E.S.; Kamino, B.A.; Patel, J.B.; Hörantner, M.T.; Johnston, M.B.; Haghighirad, A.A.; Moore, D.T.; Snaith, H.J. Bandgap-Tunable Cesium Lead Halide Perovskites with High Thermal Stability for Efficient Solar Cells. Adv. Energy Mater. 6, 8, 1502458 (2016).

[134] Im, J.-H.; Lee, C.-R.; Lee,J.-W.; Park, S.-W.; Park, N.-G. 6.5% efficient perovskite quantum-dot-sensitized solar cell. Nanoscale, 3, 4088-4093 (2011).

[135] Swarnkar, A.; Marshall, A.R.; Sanehira, E.M.; Chernomordik, B.D.; Moore, D.T.; Christians, J.A.; Chakrabarti, T.; Luther, J.M. Quantum dot–induced phase stabilization of α-CsPbI3 perovskite for high-efficiency photovoltaics. Science, 354, 6308, 92-95 (2016).

[136] Akkerman, Q.A.; Gandini, M.; Di Stasio, F.; Rastogi, P.; Palazon, F.; Bertoni, G.; Ball, G.M.; Prato, M.; Petrozza, A.; Manna, L. Strongly emissive perovskite nanocrystal inks for high-voltage solar cells. Nat. Energy, 2, 16194 (2016).

[137] Almeida G., Goldoni L., Akkerman Q., Dang Z., Khan A.H., Marras S., Moreels I., Manna L., Role of Acid–Base Equilibria in the Size, Shape, and Phase Control of Cesium Lead Bromide Nanocrystals, ACS Nano, 12 (2), pp 1704–1711 (2018).

[138] Hoke E.T., Slotcavage D.J., Dohner E.R., Bowring A.R., Karunadasa H.I., McGehee M.D., Reversible photo-induced trap formation in mixed-halide hybrid perovskites for photovoltaics, Chem. Sci., 6, 613-61 (2015).

[139] D'Innocenzo, V.; Kandada, A.R.S.; De Bastiani, M.; Gandini, M.; Petrozza, A. Tuning the Light Emission Properties by Band Gap Engineering in Hybrid Lead Halide Perovskite. J. Am. Chem. Soc., 136 (51), 17730–17733 (2015).

[140] Grancini, G.; Kandada, A.R.S.; Frost, J.M., Barker, A.J.; De Bastiani, M.; Gandini, M.; Marras, S.; Lanzani, G.; Walsh, A.; Petrozza, A. Role of microstructure in the electron–hole interaction of hybrid lead halide perovskites. Nat. Photonics, 9, 695–701 (2015).

[141] Khim, D.; Han, H.; Baeg, K.-J.; Kim, J; Kwak, S.-W.; Kim, D.-Y.; Noh, Y.-Y. Simple Bar-Coating Process for Large-Area, High-Performance Organic Field-Effect Transistors and Ambipolar Complementary Integrated Circuits. Adv. Mater., 25, 31, 4302-4308 (2013).

[142] Dagara J., Castro-Hermosa S., Lucarelli G., Cacialli F., Brown T.M., Highly efficient perovskite solar cells for light harvesting under indoor illumination via solution processed SnO2/MgO composite electron transport layers, Nano Energy, Volume 49, Pages 290-299 (2018).

[143] Heo, J. H.; Im, S. H.; Noh, J. H.; Mandal, T. N.; Lim, C.; Chang, J. A.; Lee, Y. H.; Kim, H.; Sarkar, A.; Nazeeruddin, M. K.; Gratzel, M.; Seok, I. S. Efficient inorganic−organic hybrid heterojunction solar cells containing perovskite compound and polymeric hole conductors. Nat. Photonics, 7, 486−491 (2013).

[144] Liu, M.; Johnston, M. B.; Snaith, H. J. Efficient planar heterojunction perovskite solar cells by vapour deposition. Nature, 501, 395−398 (2013).

[145] Deschler F., Price M., Pathak S., Klintberg L.E., Jarausch D.D., Higler R., Hüttner S., Leijtens T., Stranks S.D., Snaith H.J., Atatüre M., Phillips R.T., Friend R.H., High Photoluminescence Efficiency and Optically Pumped Lasing in Solution-Processed Mixed Halide Perovskite Semiconductors, J Phys Chem Lett., 5(8):1421-6 (2014).

[146] Stranks S.D., Burlakov V.M., Leijtens T., Ball J.M., Goriely A., Snaith A.J., Recombination Kinetics in Organic-Inorganic Perovskites: Excitons, Free Charge, and Subgap States, Phys. Rev. Applied 2, 034007 (2014).

[147] Kojima A., Ikegami M., Teshima K., Miyasaka T., Highly Luminescent Lead Bromide Perovskite Nanoparticles Synthesized with Porous Alumina Media, Vol.41, No.4, 397-399 (2012).

[148] Noel N.K., Abate A., Stranks S.D., Parrott E.S., Burlakov V.M., Goriely A., Snaith H.J., Enhanced photoluminescence and solar cell performance via Lewis base passivation of organic-inorganic lead halide perovskites, ACS Nano, 8(10):9815-21 (2014).

[149] Agiorgousis M.L., Sun Y.Y., Zeng H., Zhang S., Strong Covalency-Induced Recombination Centers in Perovskite Solar Cell Material CH3NH3PbI3, J. Am. Chem. Soc., 136 (41), pp 14570–14575 (2014).

[150] Nirmal, M.; Brus, L., Luminescence Photophysics in Semiconductor Nanocrystals. Acc. Chem. Res., 32, 407–414 (1999).

[151] Docampo P., Ball J.M., Darwich M., Eperon G.E., Snaith, H.J., Efficient organometal trihalide perovskite planar-heterojunction solar cells on flexible polymer substrates. Nat. Commun., 4, 2761 (2013).

[152] Gonzalez-Carrero S., Galian R.E., Perez-Prieto J., Organic-inorganic and all-inorganic lead halide nanoparticles, Opt. Express, 24, A285 (2015).

[153] Gonzalez-Carrero S., Galian R.E., Perez-Prieto J., Maximizing the emissive properties of CH3NH3PbBr3 perovskite nanoparticles, J. Mater. Chem. A, 3, 9187 (2015).

[154] Huang H., Susha A.S., Kershaw S.V., Hung T.F., Rogach A.L., Control of Emission Color of High Quantum Yield CH3NH3PbBr3 Perovskite Quantum Dots by Precipitation Temperature, Adv. Sci., 2, 1500194 (2015).

[155] Shirasaki Y., Supran G.J., Bawendi M.G., Bulovic V., Emergence of colloidal quantum-dot light-emitting technologies, Nat. Photonics, 7, 13 (2013).

[156] Protesescu L., Yakunin S., Bodnarchuk M.I., Krieg F.K., Caputo R., Hendon C.H., Yang R.X., Walsh A., Kovalenko M.V., Nanocrystals of Cesium Lead Halide Perovskites ($CsPbX_3$, X = Cl, Br, and I): Novel Optoelectronic Materials Showing Bright Emission with Wide Color Gamut, Nano Lett., 15, 3692 (2015).

[157] Zhang F., Zhong H., Chen C., Wu X., Hu X., Huang H., Han J., Zou B., Dong Y., Brightly Luminescent and ColorTunable Colloidal CH3NH3PbX3 (X = Br, I, Cl) Quantum Dots: Potential Alternatives for Display Technology, ACS Nano, Vol. 9, No. 4, 4533–4542 (2015).

[158] Chin X.Y., Perumal A., Bruno A., Yantara N., Veldhuis S.A., Martínez-Sarti L., Chandran B., Chirvony V., Shu-Zee Lo A., So J., Soci C., Grätzel M., Bolink H.J., Mathews N., Mhaisalkar S.G., Self-assembled hierarchical nanostructured perovskites enable highly efficient LEDs via an energy cascade, Energy & Environmental Science, Issue 7 (2018).

[159] De Mello J.C., Wittmann H.F., Friend R.H., An improved experimental determination of external photoluminescence quantum efficiency, Advanced Materials, 9, 3 (1997).